Operando infrared characterization of polymer electrolyte membrane water splitting electrolyzers

Kevin Krause

université de BORDEAUX

THÈSE PRÉSENTÉE

POUR OBTENIR LE GRADE DE

DOCTEUR DE L'UNIVERSITÉ DE BORDEAUX

École Doctorale Sciences Physiques et de l'Ingénieur

Spécialité : Mécanique

Par Kevin KRAUSE

Caractérisation infrarouge operando des électrolyseurs à membrane électrolytique polymère pour la séparation de l'eau

---

Sous la direction de : Jean-Luc BATTAGLIA

Co-direction : Stéphane CHEVALIER

Soutenue le 16 février 2024

Membres du jury :

Mme DIDIERJEAN, Sophie	Professeure	Université de Lorraine	**Rapporteure**
M. MILLET, Pierre	Professeur	Université Paris-Saclay	**Rapporteur**
Mme BAZYLAK, Aimy	Professeure	University of Toronto	**Examinateure**
M. BOBET, Jean-Louis	Professeur	ICMCB Bordeaux	**Examinateur**
M. TOURVIELLE, Jean-Noël	Ingénieur de recherche	Syensqo	**Examinateur**
M. BATTAGLIA, Jean-Luc	Professeur	Université de Bordeaux	**Directeur**
M. CHEVALIER Stéphane	Maître de conférences	ENSAM Bordeaux	**Co-directeur**

Acknowledgments

I would first like to thank Stéphane for being everything I could have wished for in a supervisor and more. I am so grateful to have had the privilege of working alongside you, as you were accommodating when I needed it, pushed me when necessary, and finally, your guidance ensured that my research was never without direction. Thank you.

To my thesis director Jean-Luc, thank you for your guidance through my PhD. While my research topic was out of the scope of your work, your constructive feedback and support pushed me to be a better researcher.

Thank you to the jury members of my defense committee: Professor Sophie Didierjean and Professor Pierre Millet, for your constructive feedback as reviewers of my thesis. I would also like to thank Professor Aimy Bazylak, Professor Jean-Louis Bobet, and Dr. Jean-Noël Tourvielle. It was an honor to have you all as jury members of my PhD defense committee and I truly enjoyed the conversations we had.

To Clement, Marine, Malo, Valentin, Thomas, Coline, Hamza, Adele, Steven, Alisa, Florian, Theo, Celia, Jeremie, and Alain, thank you. Everyone helped me transition to life in a country where I don't speak the language. Thanks to you all, I was able to hopefully learn some French! We'll see how well I can remember what I've learned.

To Clement and Marine, you were the greatest friends I could have asked for during my time in France. You both made me feel like I had a second home away from home.

To Marine, Malo, and Alisa, I truly enjoyed running together with you and I look forward to seeing you all at the 2024 French Olympics! Looking forward to the many races we have yet to run.

To everyone I met playing Super Smash Brothers Melee during my time in Bordeaux, it was truly a pleasure to meet everyone. There are too many of you and too many moments to write about, but I will cherish these memories and come back to the EU scene a better player than ever!

Finally, to those closest to me: Mom and Dad, thank you for your unwavering support. Jamie, thank you once again for being there for me every step of the way (5 years!!!). Your support always pushed me to be my best self.

Résumé

Les électrolyseurs à électrolyte polymère (PEM), employés dans le processus d'électrolyse de l'eau, ont une utilisation limitée due au manque de connaissances des phénomènes physiques en jeu, notamment au niveau de la membrane utilisée pour séparer l'eau. La compréhension des mécanismes de transfert de masse et d'ions au sein de cette membrane est essentielle pour améliorer le rendement de ces systèmes. Ainsi, l'objectif de cette thèse est de développer une technique de caractérisation basée sur l'imagerie afin de mieux comprendre les phénomènes de transport dans la membrane d'une PEM. Le déroulement de cette thèse est organisé en deux parties.

Dans la première partie de la thèse, une plateforme d'imagerie basée sur la spectroscopie infrarouge (IR) à transformée de Fourier (FTIR) et sur la thermographie IR est présentée. Le dispositif expérimental a été développé et utilisé pour étudier deux réactions acide-base exothermiques dans un canal microfluidique. Le champ de concentration 2D imagé permet de quantifier simultanément le transport de chaleur et de masse dans le canal microfluidique. Les résultats expérimentaux ont été utilisés pour valider une simulation du phénomène de diffusion-advection-réaction. Ces premiers résultats ont permis de montrer la viabilité du banc expérimental pour la caractérisation du transfert de masse dans une puce microfluidique.

Dans la deuxième partie de la thèse, une PEM microfluidique a été spécifiquement développée afin de mesurer la teneur en eau dans la membrane via une technique de spectroscopie par transmission dans la gamme IR. Dans un premier temps, un dispositif de spectroscopie FTIR synchrotron a été utilisé pour étudier le processus de séchage et d'hydratation de la membrane. L'électrolyseur PEM microfluidique a ensuite été caractérisé sur une plateforme d'imagerie qui combine la spectroscopie IR et les mesures électrochimiques. Les cartographies 2D obtenues grâce à cette technique permettent de quantifier l'hydratation de la membrane sur une surface. La combinaison des images et des mesures électrochimiques a permis d'établir le lien entre les performances, les pertes ohmiques et le transport de masse dans la membrane. Les résultats de cette thèse montrent le potentiel des techniques IR basées sur la transmission pour comprendre les mécanismes de transport dans les PEM microfluidiques en fonctionnement. Ces techniques IR sans contact pourraient être utilisées pour quantifier d'autres phénomènes tels que la traînée électro- ou thermo-osmotique.

Abstract

Understanding and improving mass and ionic transport mechanisms within the membrane used in polymer electrolyte membrane (PEM) water splitting electrolyzers is vital for achieving improved efficiencies that would enable the use of water electrolysis in sustainable energy infrastructures. A better understanding of mass and ion transport within the PEM are essential to achieving the improved performance and efficiencies necessary for wide-scale commercialization of these devices. The work from this thesis aims to improve characterization methods for measuring PEM hydration using an operating microfluidic PEM electrolysis chip coupled with operando infrared (IR) spectroscopy. This development of this thesis is organized through two parts.

In part one and prior to the development of the microfluidic electrolyzer, the experimental setup for IR characterization via Fourier transform infrared spectroscopy (FTIR) and IR thermography was developed. This setup was tested through a microfluidic chip designed for semi-transparency in mid-wave IR light. Two exothermic acid-base reactions were imaged in the chip to simultaneously quantify heat and mass transport in the microfluidic channel. Concentration fields of each chemical species and thermal fields of the chemical reactions were resolved from the acquired IR images. Experimental results were used to validate an advection diffusion simulation of the chemical reaction within a meshed replica of the microfluidic chip, for which there was a strong agreement between the results from each dataset.

In part two, the methods from part one were honed for the fabrication of the first microfluidic PEM water electrolyzer for transmission-based IR characterization. The water content within the PEM of the microfluidic water electrolyzer was characterized through two operando IR spectroscopy setups. The first IR experimental setup utilized a synchrotron FTIR spectroscopy setup, where the water content of the PEM was quantified using IR for the first time, albeit only at a single point. The second microfluidic PEM electrolyzer setup used a broadband IR source combined with other techniques to distinguish contributions from ohmic, kinetic, and mass transport losses while acquiring IR images. Images were acquired during potentiostatic operation for a range of anolyte concentrations. Electrochemical impedance spectroscopy (EIS) and distribution of relaxation times (DRT) analysis unveiled that higher anolyte concentrations were accompanied by reduced ohmic losses but higher kinetic and mass transport losses. The higher mass transport losses were investigated through images averaged over comparable time scales to EIS and DRT results, and

implied that inefficient gas removal occurred at the cathode. These effects were further investigated through the PEM hydration (λ_{H_2O}) via three characteristic regions where the adjacent channels were either wet, dry, or a mix of both. The local channel wetness was observed to strongly affect the PEM's hydration through gradients that manifested between cathode and anode channels.

Results from this thesis show the potential of transmission-based IR techniques for elucidating transport mechanisms in PEMs of operating microfluidic electrolyzers. Implementing layers that are traditionally implemented in fuel cells and electrolyzers for gas-liquid management into the microfluidic PEM electrolyzer could greatly improve results obtained from the presented methods. Consequently, IR techniques could potentially be used to achieve the contactless quantification of phenomena such as electro- or thermo-osmotic drag. The findings in this thesis provide valuable insights for membrane characterization in electrochemical devices with integrated PEMs, and will inform the next generation of electrolyzer design.

Table of Contents

List of Tables

List of Figures

List of Appendices

Abbreviations

Technical Abbreviation:

2D	Two-dimensional
3D	Three-dimensional
AC	Alternating current
AFM	Atomic force microscopy
ATR	Attenuated total reflection
CAFM	Conductive atomic force microscopy
CCM	Catalyst coated membrane
CL	Catalyst layer
CFD	Computational fluid dynamics
CFL	Courant-Friedrichs-Lewy
CT	Computed tomography
DI	De-ionized
DRT	Distribution of relaxation times
DVS	Dynamic vapor sorption
eDRT	Extended distribution of relaxation times
EEC	Equivalent electrical circuit
EIS	Electrochemical impedance spectroscopy
FFT	Fast Fourier transform
FTIR	Fourier transform infrared
GDL	Gas diffusion layer
HER	Hydrogen evolution reaction
HFR	High frequency resistance
IR	Infrared

LFR	Low frequency resistance
MEA	Membrane electrode assembly
MRI	Magnetic resonance imaging
MWIR	Mid-wave infrared
NMR	Nuclear magnetic resonance
OCV	Open circuit voltage
OER	Oxygen evolution reaction
SAXS	Small-angle X-ray scattering
PEM	Polymer electrolyte membrane
PEMFC	Polymer electrolyte membrane fuel cell
PFAS	Per/polyfluoroalkyl substance
PGSE	Pulsed field gradient spin-echo
PID	Proportional-integral-derivative
PTL	Porous transport layer
RH	Relative humidity
WAXS	Wide-angle X-ray scattering

Chemical Abbreviations:

e^-	Electron
H^+	Hydrogen proton
HCl	Hydrochloric acid
H_2	Hydrogen
H_2O	Water
H_2SO_4	Sulfuric acid
H_3O^+	Hydrated proton
InSb	Indium Antimonide
IPA	Isopropanol
Ir	Iridium
NaCl	Sodium chloride
NaOH	Sodium hydroxide
Na_2SO_4	Sodium sulfate
O_2	Oxygen
PDMS	Polydimethylsiloxane
PEEKK	Polyetheretherketoneketone
Pt	Platinum
PTFE	Polytetrafluoroethylene
Ru	Ruthenium
Si	Silicon
SO_3^-	Sulfonic acid site
VTES	Vinyltriethoxysilane
ZnSe	Zinc selenide

Nomenclature

a_x	Linear fit coefficient x [-]
A	Absorbance [-]
α	Thermal expansion coefficient [K^{-1}]
Bi	Biot number [-]
C_i	Concentration of chemical species i [mol L^{-1}]
C_0	Total concentration of chemicals per pixel [mol L^{-1}]
C_p	Specific heat [J kg^{-1} K^{-1}]
D	Diffusion coefficient [m^2 s^{-1}]
D	(Appendix) Derivative term of PID
DL	Digital level [-]
E_{cell}	Cell potential [V]
E_{Nernst}	Nernst potential [V]
E_{rev}	Reversible cell potential [V]
E_{th}	Thermo-neutral potential [V]
ϵ	Thermal radiation captured by camera[-]
Γ	Transmittance [-]
γ	Creation [+1] or consumption [-1] coefficient
EW	Equivalent weight [$g_{polymer}$ $mol_{ionic\text{-}group}^{-1}$]
η_{ohm}	Ohmic overpotential [V]
η_{kin}	Kinetic/activation overpotential [V]
η_{mt}	Mass transport overpotential [V]
F	Faraday's constant (96485 C mol^{-1})
ΔG	Gibbs free energy [J mol^{-1}]
h	Enthalpy of reaction [kJ mol^{-1}]

$h(\tau)$	Tikhonov regularization function
h_k	Absolute polarization contribution from RC element k
ΔH	Change in enthalpy [J mol^{-1}]
$\Delta_f H°_{liquid}$	Enthalpy of formation of liquid under standard conditions [kJ mol^{-1}]
i	Current density [A cm^{-2}]
I	Image [-]
I	(Appendix) Integral term of PID
I_0	Reference image [-]
I_{AC}	Modulating component of image signal [-]
I_{DC}	Constant component of image signal [-]
j	Unit imaginary number $= \sqrt{-1}$
k	Permeability [cm^2]
k_f	Reaction kinetics coefficient [m^3 mol^{-1} s^{-1}]
k_m	Mass transport coefficient [cm s^{-1}]
K_d	(Appendix) Gain for the derivative term
K_i	(Appendix) Gain for the integral term
K_p	(Appendix) Gain for the proportional term
κ	Thermal conductivity [W m^{-1} K^{-1}]
l_w	Membrane water content [µm]
λ	Wavelength [m]
λ_{H_2O}	Molar fraction of water molecules per sulfonic-acid group [-]
$\overline{\lambda_{H_2O}}$	Change in membrane hydration [-]
$\Delta\overline{\lambda_{fit}}$	Linear fit of averaged λ [-]
Λ	Regularization parameter

m_{rx}	Molar fraction coefficient [-]
M	Molar mass [kg mol^{-1}]
μ_i	Multispectral absorptivity coefficient of chemical species i [L mol^{-1}]
μ_{visc}	Dynamic viscosity [cP] or [kg m^{-1} s^{-1}] or [Pa s]
n	Charge transfer number [-]
ω	Angular frequency [-]
p	Pressure [Pa]
P_x	Partial pressure of x [a.u.]
P	(Appendix) Proportional term of PID
PV	(Appendix) Process variable
ϕ_w	Molar volume fraction [-]
$\Delta\phi$	Proton flux
q	Flow rate [L min^{-1}]
res_{px}	Pixel resolution [µm^2 px^{-2}]
R	Universal gas constant (8.314 J mol^{-1} K^{-1})
R_{ohm}	Ohmic resistance [Ω cm^{-2}]
ρ	Density [kg m^3]
ΔS	Percent change in water saturation [%]
S_{C_i}	Concentration source term [-]
S_T	Temperature source term [-]
SP	(Appendix) Set point
t	Thickness [m]
T	Temperature [K]
TAC	Total acid capacity [g mol$_{SO3H}^{-1}$]

τ	Time constant [s]
u	Velocity field [m s^{-1}]
v	Velocity [m s^{-1}]
ν	Kinematic viscosity [cSt] or [mm^2 s^{-1}]
Z	Impedance [Ω cm^{-2}]

1 Introduction

Over the past couple decades, poorly regulated anthropogenic activities have led to rapidly increasing global temperatures and have triggered the sixth and ongoing extinction event – The Holocene Extinction.[1] This looming threat of climate change has motivated the shift in energy usage from fossil fuel consumption to renewable energy. While the shift to renewable energy is promising and is scaling up globally, it must also accommodate the increasing global energy consumption which was forecasted by the EIA to increase by 56 % between 2010 and 2040.[2] In addition to the development of renewable energy technologies such as wind and solar, energy storage infrastructure must be developed in tandem to compensate for the intermittent nature of these renewable technologies.[3,4]

A hydrogen economy has been proposed as a potential solution for energy storage when coupled with intermittent renewable energy technologies.[5,6] Electrical energy produced through wind and solar can be converted and stored to chemical energy in the form of hydrogen as an energy carrier. Polymer electrolyte membrane (PEM) water electrolyzers are one of the most promising technologies for fulfilling this necessity, through the electrochemical splitting of water in the absence of carbon emissions. Moreover, PEM electrolysis benefits from: high purity hydrogen production (>99.95 %), fast system responses (on the millisecond scale), high operating current densities, and flexible operating conditions.[7,8] However, the high capital costs and low efficiencies of these devices has slowed their commercialization, and are consequently key research targets for spearheading this technology.[8] Thus, optimizing the efficiency of PEM water electrolysis is imperative for achieving the future hydrogen economy.

1.1 Polymer electrolyte membrane water electrolysis

PEM electrolyzers are typically comprised of the PEM, flow channels, porous transport layers (PTLs), and catalyst layers (CLs). The PEM is a thin (~20 μm to 300 μm thick) persulfonated membrane that separates the anode and cathode compartments of the electrolyzer. In electrolyzers, the PEM is a solid electrolyte between the anode and cathode CLs, acting as an electrical insulator and reactant barrier while remaining permeable to protons.[9,10] The flow channels deliver reactants through the PTL to the catalyst layer, where the electrochemical reaction occurs (*Fig. **1-1***).

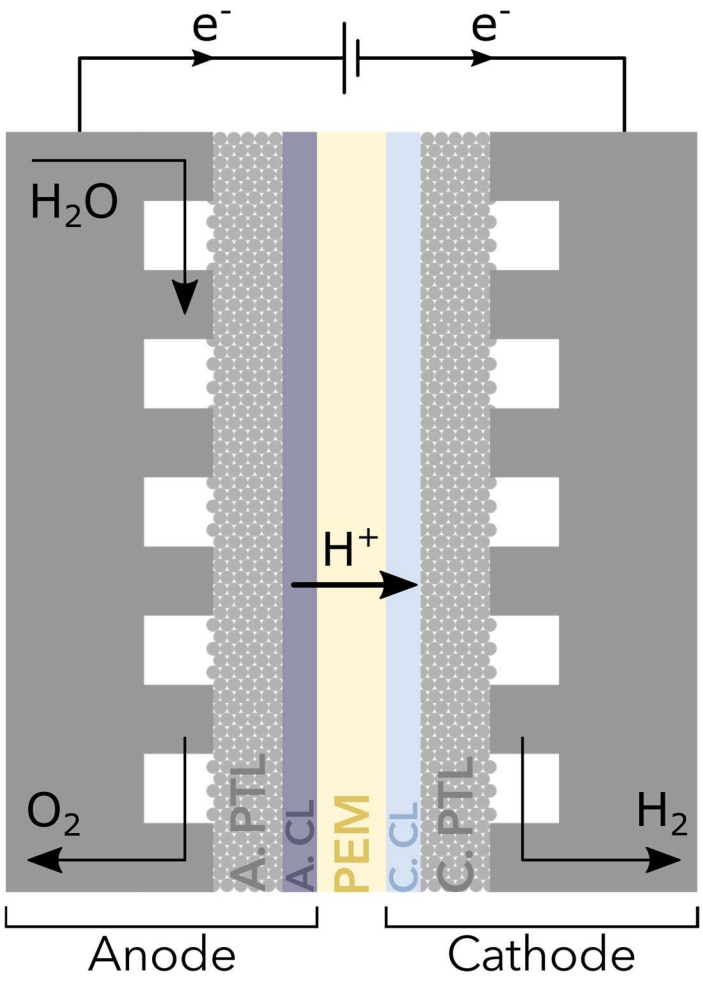

Fig. 1-1: A schematic of a PEM electrolyzer for water splitting. Oxygen evolution occurs at the anode, and hydrogen evolution occurs at the cathode.

At the anode CL, the oxygen evolution reaction (OER) separates water molecules are into oxygen gas and hydrogen protons, as shown below in *Eq. 1-1*. The PEM is preferentially permeable to the byproduct hydrogen protons and blocks oxygen gas from the OER. Hydrogen protons that traverse through the PEM to the cathode compartment are converted to hydrogen gas through the hydrogen evolution reaction (HER) as shown in *Eq. 1-2*. The overall reaction considering both the HER and OER is shown in *Eq. 1-3*.

$$\text{Anode: } \boldsymbol{H_2O \rightarrow 2H^+ + \frac{1}{2}O_2 + 2e^-} \qquad \textit{Eq. 1-1}$$

$$\text{Cathode: } \boldsymbol{2H^+ + 2e^- \rightarrow H_2} \qquad \textit{Eq. 1-2}$$

$$\text{Overall: } \boldsymbol{H_2O \rightarrow H_2 + \frac{1}{2}O_2} \qquad \textit{Eq. 1-3}$$

When the electrolyzer is operated under reversible conditions (i.e. open-circuit conditions), the reversible potential of the electrolyzer E_{rev} [V] can be determined as a function of temperature T and pressure P.

$$\boldsymbol{E_{rev}(T,P) = \frac{\Delta G(T,P)}{nF}} \qquad \textit{Eq. 1-4}$$

where ΔG is the Gibb's free energy of reaction [J mol^{-1}], n is the charge transfer number [-], and F is Faraday's constant [96485 C mol^{-1}]. The thermo-neutral potential E_{th} is the potential drop across an electrochemical cell necessary to drive the reaction while providing heat to maintain a constant temperature, and is determined relative to the change in enthalpy for the system ΔH [J mol^{-1}] instead of ΔG.

$$\boldsymbol{E_{th}(T,P) = \frac{\Delta H(T,P)}{nF}} \qquad \textit{Eq. 1-5}$$

Under standard conditions ($T° = 298$ K and $P° = 1$ atm), the change in enthalpy is $\Delta H° = 285.84$ kJ mol^{-1}, and the Gibb's free energy of electrochemical water splitting is $\Delta G° = 237.22$ kJ mol^{-1}, making the reaction strongly endothermic and therefore non-spontaneous.[11] Consequently, at these conditions the reversible potential is $E_{rev}° = 1.2293$ V and the thermo-neutral voltage is $E_{th}° = 1.4813$ V. The ideal potential of the electrolyzer is sensitive to the temperature and pressure, and electrolysis under non-standard conditions can be described through the Nernst equation:

$$\boldsymbol{E_{Nernst} = E_{rev}(T,P) + \frac{RT}{nF}\ln\left(\frac{P_{H_2}P_{O_2}^{1/2}}{P_{H_2O}}\right)} \qquad \textit{Eq. 1-6}$$

where R is the ideal gas constant [8.314 J mol^{-1} K^{-1}], T is the temperature [K], and P_{H_2}, P_{O_2}, and P_{H_2O} are the partial pressures of hydrogen, oxygen, and water at the reaction sites [-], respectively. P_{H_2O} is only applicable if electrolysis uses water in its vapor form and therefore at temperatures above 100 °C, otherwise $P_{H_2O} = 1$. In practice, the operating potential of a water electrolyzer E_{cell}

is considerably larger than the ideal potential due to overpotentials. There are three sources of overpotentials: (1) ohmic η_{ohm} [V], (2) kinetic η_{kin} [V], and (3) mass transport η_{mt} [V].

$$\boldsymbol{E_{cell} = E_{Nernst} + \eta_{ohm} + \eta_{kin} + \eta_{mt}} \qquad \textit{Eq. 1-7}$$

Each overpotential contribution dominates cell overpotentials at different currents for the electrolyzer, which can be visualized through a polarization curve (*Fig. 1-2*). Specifically, at low currents kinetic overpotentials are dominant and manifest as a logarithmic increase, while at high currents mass transport overpotentials dominate and manifest as an exponential increase leading to cell failure. At currents in between kinetic and mass transport dominated potentials, ohmic overpotentials dominate as a linear contribution which is comprised of the ionic resistance of the PEM, the total electronic resistance of each cell component between electrodes, and the interfacial resistances between each layer of the electrolyzer.[12]

$$\boldsymbol{\eta_{ohm} = iR_{ohm}} \qquad \textit{Eq. 1-8}$$

where i is the current density of the electrolyzer [A cm^{-2}] and R_{ohm} is the total ohmic resistance of the electrolyzer [Ω cm^2] from the previously mentioned sources of electronic resistance. Kinetic overpotential (also known as activation overpotentials) is the necessary activation potential for splitting water molecules, which is significantly higher for the OER at the anode due to its slower reaction kinetics in comparison to the HER at the cathode.[13] Mass transport overpotentials occur due to the gas-liquid phase boundary between the reactant water and product gas. Inefficient gaseous product removal from the CL prevents reactant water from reaching the electrodes, leading to exponential increases in overpotential with the applied current density.[14,15]

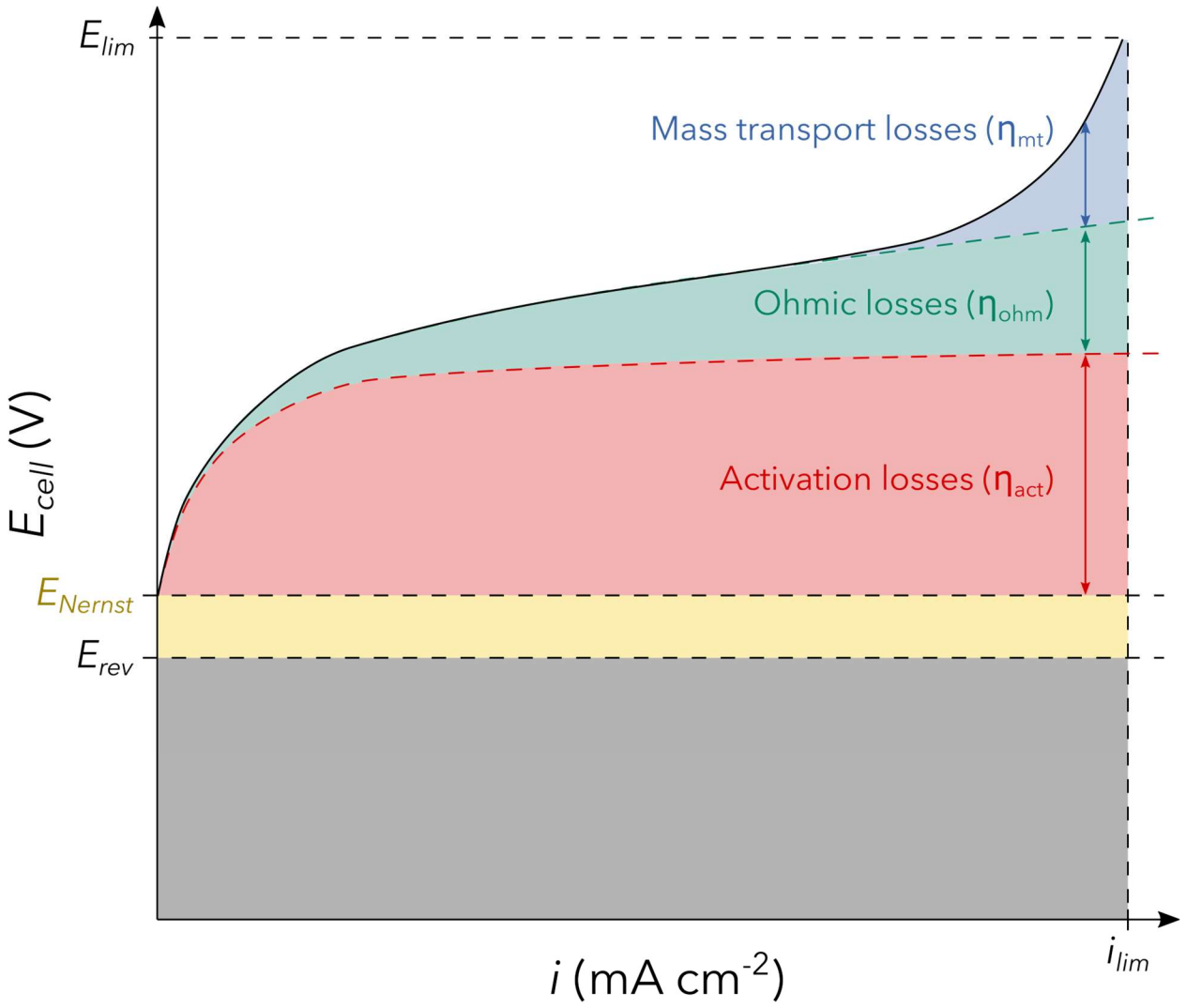

Fig. 1-2: A sample polarization curve with labeled loss contributions. Activation losses are dominant at low current densities, ohmic losses scale linearly with the current density relative to the ohmic resistance of the cell, and mass transport losses are dominant at high current densities that commonly drive cell failure at the limiting current density $\boldsymbol{i_{lim}}$ *and potential* $\boldsymbol{E_{lim}}$.

The commercialization of water electrolysis is dependent on minimizing each source of overpotential, requiring in depth knowledge of not only the materials employed, but also the complex physics that occur within water electrolyzers. PEMs in particular are the key component of these devices that have seen continuous use since their development before the 1950s;[16,17] however, mass transport within the PEM (particularly the inter-relation between proton and water transport) remains poorly understood. Understanding mass transport phenomena within the PEM is vital for optimizing water electrolysis, and therefore fulfillment of the hydrogen economy.

1.2 Objectives

Studies investigating mass transport associated with PEM water splitting have primarily focused on the two-phase transport of gas and liquid within the PTLs.[18–20] Although these works have highlighted the importance of water management on cell performance, transport phenomena within another core component of electrolyzers, the PEM, have often been overlooked to investigate PTLs instead. For example, Arbabi et al. evaluates the feasibility of integrating microfluidics as platforms for characterizing porous gas diffusion layers in electrolyzers.[21] However, while PTLs play an instrumental role in promoting PEM hydration, the mechanisms that drive proton transport through a PEM also have potential for investigation through microfluidic chips.[22] Particularly, there is much to be gained through the combination of PEMs in microfluidics with techniques that have yet to be implemented in the field, such as operando infrared (IR) spectroscopy.

The objectives of this thesis are to characterize the hydration in the PEM of a working water electrolyzer. This will be realized by fabricating microfluidic PEM electrolyzer and then characterizing transport through the PEM via transmission IR techniques. These objectives have been fulfilled through the following goals:

- Develop a semi-transparent microfluidic chip in the IR spectral range, and then quantify heat and mass transport within the chip for an acid-base reaction
- Fabricate a microfluidic PEM electrolyzer that is semi-transparent in the IR spectral range, then characterize its membrane hydration via operando IR spectroscopic imaging under different failure conditions
- Determine contributions from ohmic, kinetic, and mass transport losses through novel (IR spectroscopic imaging) and commonly used (electrochemical impedance spectroscopy and distribution of relaxation times) characterization techniques in the field, and then evaluate correlations between loss mechanisms and IR imaging data

The key contribution of this thesis enables the characterization of PEMs through a technique that has yet to be utilized in the field, enabling the elucidation of mass transport mechanisms through the PEM that remain poorly understood.

1.3 Contributions

A list of first authored contributions directly based on the work presented in this thesis is presented below.

- Krause, K., Palka, C., Garcia, M., Erriguible, A., Glockner, S., Pradère, C., Chevalier, S., (2022) "Heat and mass transfer visualization of an exothermic acid-base microfluidic reactor using infrared thermo-spectroscopy" (In preparation) (Chapter 3)

- Krause, K., Garcia, M., Michau, D., Clisson, G., Billinghurst, B., Battaglia, JL., Chevalier, S., (2023) "Probing membrane hydration in microfluidic polymer electrolyte membrane electrolyzers via operando synchrotron Fourier transform infrared spectroscopy" Lab on a Chip, 23, 18, 4002-4009 (Chapter 5)

- Krause, K., Crête Lawrence, A., Michau, D., Battaglia, JL., Chevalier, S. (2023) "Investigating inter-electrode water diffusion in a microfluidic polymer electrolyte membrane electrolyzer via operando infrared spectroscopic imaging" (In preparation) (Chapter 6)

Each of these studies would not have been achieved without the collaboration from the co-authors. The following list summarizes the contributions from each co-author in the aforementioned studies:

Ms. Garcia (PhD candidate) is a co-author for the publication and manuscript in preparation based on Chapter 3 and Chapter 5. She participated in the development of the experiments, the experimental data collection, and the discussion of the results.

Mr. Palka (PhD candidate) performed the modelling work presented in Section 3.3 under the supervision of Dr. Erriguible (Associate Professor from the Institut Polytechnique de Bordeaux), and Dr. Glockner (Research Engineer with HDR from the Institut Polytechnique de Bordeaux), and they are all co-authors for the manuscript in preparation based on Chapter 3.

Dr. Michau (collaborator from the Institut de Chimie de la Matière Condenséé de Bordeaux) is a co-author for the publication and manuscript in preparation based on Chapter 5 and Chapter 6. He participated in the fabrication of the microfluidic chips by performing the electrode depositions.

Mr. Clisson (collaborator from Solvay) is a co-author for the publication based on Chapter 5. He participated in the fabrication of the microfluidic chips.

Dr. Billinghurst (collaborator from the Canadian Light Source) is a co-author for the publication based on Chapter 5. He participated in the experimental data collection and the discussion of results.

Ms. Crête Lawrence (former student intern from the University of Toronto) is a co-author for the publication based on Chapter 6. She participated in the development of the experiment, the experimental data collection, and the discussion of the results.

In addition to the works presented above, I have also made contributions to the following work by a peer from the same lab.

- Chassain, C., Kusiak, A., Krause, K., Garcia, M., Battaglia, JL. (2023) “Bayesian estimation of thermal properties using periodically pulsed photothermal radiometry: A focus on interfacial thermal resistances between layers” physica status solidi (RRL)–Rapid Research Letters, 17, 2, 2200328

1.4 Organization of the thesis

This thesis is organized in eight chapters which are recommended to be read in order. Chapter 1 serves as an introductory chapter to describe the fundamentals of water electrolysis. The objectives and contributions of this thesis are also presented. The remainder of this thesis is separated into two main parts.

Part one of this thesis contains Chapter 2 and Chapter 3. This part is focused on the characterization of simplified microfluidics via IR techniques and establishes the context necessary for part two of this thesis. In Chapter 2, a brief background for microfluidics and their potential when coupled with infrared techniques utilized in the subsequent chapter are presented. The working principles and post-processing routines associated with each IR technique are also elaborated. Chapter 3 puts the background presented in the previous chapter into practice, through the fabrication of a microfluidic chip for the investigation of heat and mass transfer via infrared techniques. Additionally, experimental and numerical results are presented and cross-validated.

Part two of this thesis contains Chapter 4, Chapter 5, and Chapter 6. This part is dedicated to providing the necessary context for PEM water electrolysis, and then bridging the research gap through the combination of PEM water electrolysis and transmission-based IR characterization. In Chapter 4, a deeper background for polymer electrolyte membrane water electrolyzers is described with a focus on transport phenomena within the PEM of water electrolyzers. Chapter 5 features the fabrication and characterization of water hydration in an operating microfluidic PEM water electrolyzer with transmission IR techniques. Chapter 6 refines the work presented in the previous chapter by improving upon and implementing additional characterization techniques for elucidating mass transport in the PEM of an operating electrolyzer.

Chapter 7 summarizes the research contributions from the work presented in this thesis. Chapter 8 concludes this thesis with recommendations for future work.

Part I. Microfluidic characterization with infrared spectroscopic imaging

2 Background for microfluidics and infrared characterization

In this chapter, laminar microfluidics are introduced as a platform for the characterization of heat and mass transfer through IR imaging techniques. The potential for characterization of semi-transparent microfluidics via infrared (IR) based techniques is introduced, and then relevant IR techniques are detailed. Specifically, the working principles and relevant processing techniques for both Fourier transform infrared (FTIR) spectroscopy and IR thermography are discussed. These techniques will be used in the study presented in the following chapter to characterize heat and mass transport in a microfluidic chemical reactor.

2.1 Microfluidics

The development of laminar microfluidics has revolutionized the modern laboratory toolkit, enabling rapid fabrication and testing of experimental conditions under well controlled conditions.[23,24] Microfluidics are particularly attractive due to the low unit cost for mass reproduction, ease of parallel processing, reduced volume of necessary sample reagents, reduced volume of waste, flexibility of fabrication techniques, and much more.[25] Moreover, when controlled through precise instruments, physical and chemical processes within microfluidic chips can be evaluated at the micro-scale. As a result, the popularity of microfluidics in research has grown exponentially, with these devices being widely adopted in research towards a variety of applications, such as the analysis of biological cells, food safety, nanoparticle preparation, and more.[26–28] The development of models for the assessment of these devices can complement microfluidics used for all of these applications. However, the refinement of these models is dependent on improving characterization methods for understanding the relevant physical and chemical processes in these devices.

A significant advantage in microfluidic devices lies in their ease of parameter control, such as fluidic regimes and heat. When the effects of parameter control are combined with ex situ characterization techniques, such as gas chromatography, liquid chromatography, mass spectroscopy, etc., the effects of various experimental parameters on the physical and chemical processes within microfluidics can be more easily interpreted. Additionally, recent advances in technology surrounding laboratory instrumentation (e.g. detectors and sources) and data

processing have advanced the quality of obtained information closer to theoretical limits.[29] As stated in the work by Perro et al., one issue of significance is the characterization of microfluidics through the use of modern tools, with the most promising being spectroscopic imaging.[30] Specifically, as the wavelengths for some microspectroscopy techniques and microfluidics share micro-scale characteristic lengths, coupling these together could provide new perspectives to relevant fields. For example, the experimental characterization of key physical phenomena within microfluidic chips, such as heat and mass transfer via IR techniques, is particular interest for developing and validating computational models.[31] In the following section, a brief overview of their characterization and the relevant techniques for Part I of this thesis is discussed.

2.2 Infrared characterization and material selection

IR techniques utilize wavelengths on the micro-scale, typically between 780 nm and 50 µm (wavenumbers between 12800 cm^{-1} and 200 cm^{-1}, respectively). IR light in this range corresponds to the vibrational energies of many molecule groups or dipole moments of the molecule change, which can be visualized through the absorption of IR photons.[30] Considering an IR spectrum from analysis, the bands observed on the spectrum can be characterized by their vibrational wavenumber or wavelength – relative to the specific molecule group or transition energy, or by their intensity – relative to the magnitude of change in bond dipole moments.[32]

Fabricating a microfluidic chip for characterization through IR techniques is accompanied by a complex set of limitations that must be considered, such as a material's transparency in the IR spectral range. Materials that are transparent in the near-IR range may not be transparent in the mid- or far-IR range. For example, sapphire is transparent in the visible range up to wavelengths in the mid-IR spectrum, while silicon attenuates visible light and is only transparent for a portion of the near-IR and all of the mid-IR spectral range, as shown in *Fig. 2-1*.[30] In addition to the materials that the microfluidic chip is comprised of, the investigated samples within the microfluidic chip (e.g. chemical reagents) must be semi-transparent. Specifically, as a completely transparent sample or a sample that completely attenuates the beam would not provide information that could be interpreted. Given the low penetrative power of light in the IR spectrum when using transmission based techniques, penetrative lengths for samples containing water is often restricted to scales less than 100 µm. However, the low characteristic lengths can be mitigated by coupling

transmission IR techniques with microfluidics designed to have channel thicknesses within this limitation.

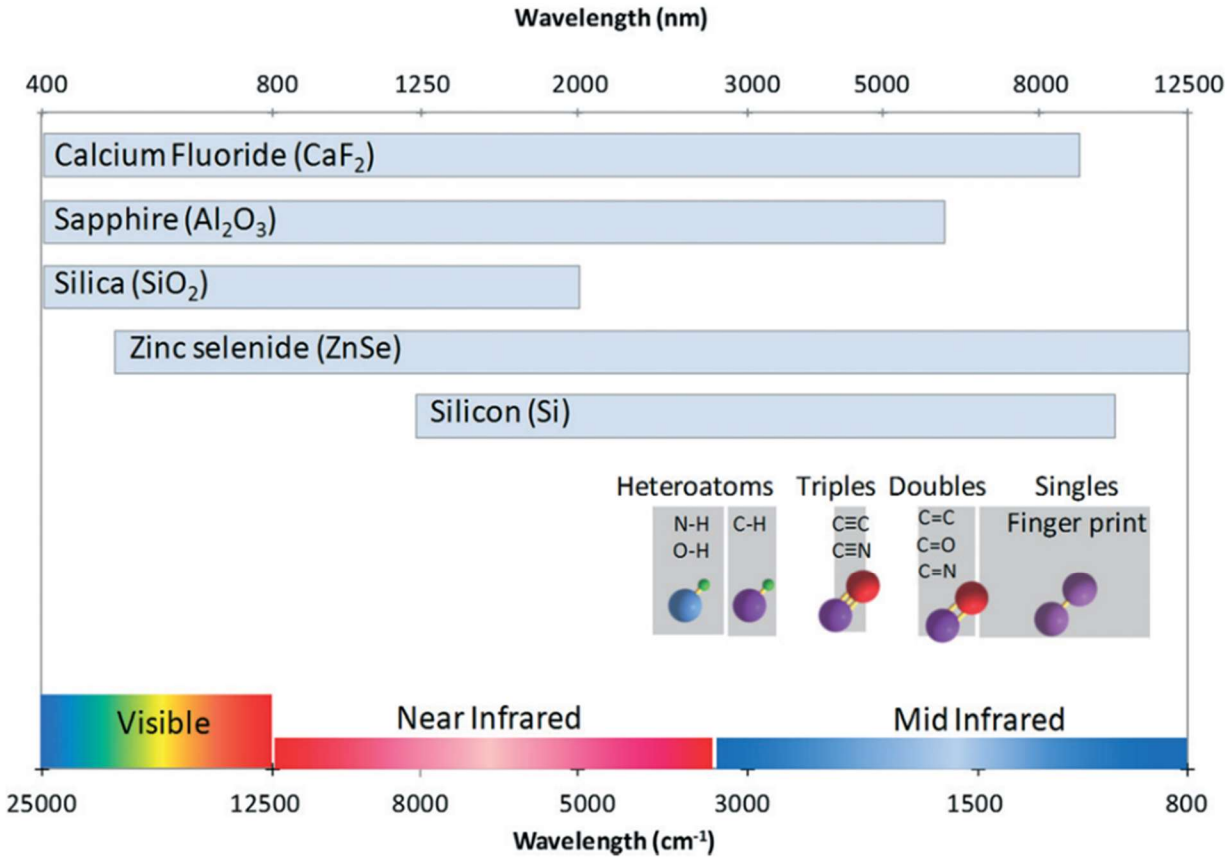

Fig. 2-1: Reproduced figure from Perro et al. featuring a guide for FTIR analysis in microfluidic reactors. The chart represents the transparent domain of materials and the major region of some conventional spectra of bond stretching.[30]

In addition to the transparency of the materials and samples, other properties that must be considered when fabricating a microfluidic chip include the chemical compatibility of the materials for investigating chemical interactions that use corrosive solutions, or the rate of thermal diffusion for studies that investigate heat transfer. While silicon is an outstanding material in terms of IR transparency, it diffuses heat extremely quickly. Therefore, heat transfer investigations using silicon materials must utilize instruments that are capable of correspondingly high temporal resolutions.[33,34] Similarly, zinc selenide (ZnSe) is known to have a remarkably wide transmission

wavelength range in IR, but reacts with acids to form the toxic hydrogen selenide gas. In addition to the experimental characteristics, fabrication techniques, such as the bonding between materials via plasma treatment, must be considered, as a material like sapphire is inert for common plasma treatment techniques.[35] Upon proper material selection for microfluidic chip fabrication, IR techniques can then be used to characterize physical and chemical phenomena within microfluidic chips.

Following material selection and the subsequent fabrication of the microfluidic chip, IR spectroscopy can be used to investigate physical or chemical processes that occur within the chip. The most common IR spectroscopy technique that utilizes IR light to produce IR spectra will be detailed in the following section as a method to investigate mass transfer. Subsequently, the associated processing routine for images acquired with this spectroscopic technique will be discussed. Heat transfer can also be characterized with IR-based techniques through the use of thermography, for which the working principles and relevant processing techniques will be introduced following IR spectroscopy.

2.2.1 Fourier transform infrared spectroscopy

2.2.1.1 Working principles of Fourier transform infrared spectroscopy

Fourier transform infrared spectroscopy can be used acquire IR spectra for the investigation of mass transfer in microfluidic reactors. The majority of IR testing is now through FTIR spectrometry, as the technique provides improved signal-to-noise ratios, accuracies, spatial resolutions, and temporal resolutions in comparison to classic IR techniques.[36] FTIR spectroscopy is performed through the use of a Michelson interferometer, which is shown in *Fig. 2-2*. Inside the FTIR spectrometer, a polychromatic IR source produces an IR beam that is collimated. The collimated beam traverses through a beam splitter, which splits the beam into two. One of the split beams is directed towards a stationary mirror while the other split beam is directed to a moving mirror. The reflected beams interfere with each other and recombine at the beam splitter. The interference characteristics of the recombined beam are dependent on the light source, mirror orientation, and mirror positioning. Subsequently, a portion of the recombined beam is then directed out of the spectrometer through the shutter. The IR beam can then be converted into an

IR spectrum spanning the full wavelength range of the polychromatic source through a Fourier transform.

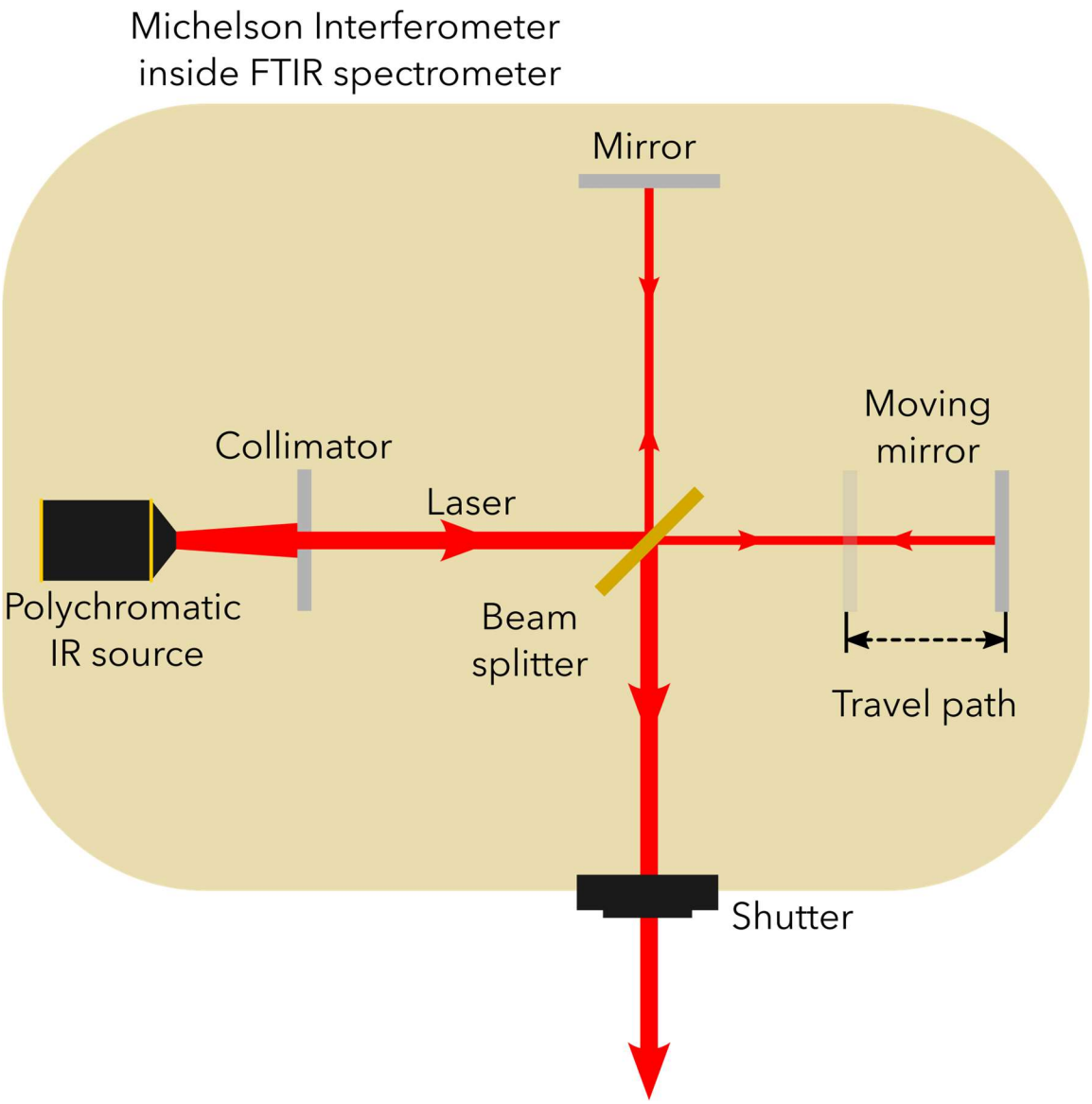

Fig. 2-2: Schematic of a Michelson interferometer used to perform FTIR spectroscopy. A polychromatic IR source produces an IR beam, which passes through a collimator. The collimated beam is split into two, where one beam is reflected by a stationary mirror and the other is reflected by a moving mirror. The two beams traverse back through the beam splitter where a portion of the beam will recombine, causing interference in the beam waves, and exit the shutter.

2.2.1.2 Image processing

The multispectral signal produced by a FTIR spectrometer is an interferogram, which needs to be processed to obtain an IR spectrum. With an appropriate camera or imaging setup, a FTIR spectrometer is capable of producing images, which are two-dimensional (2D) fields. Each pixel that an image produced by a FTIR spectroscopy is comprised of can be interpreted as an interferogram, as shown in *Fig. **2-3**a* and *Fig. **2-3**b*. Acquired images from FTIR spectroscopic imaging can be summarized through the following equation,

$$\boldsymbol{I_{tot} = I_{DC} + I_{AC}(x, y, \delta)} \qquad \textit{Eq. 2-1}$$

where I_{tot} is the complete image, I_{DC} is the continuous component from the spectrometer light source, and I_{AC} is the modulated component from the Michelson interferometer. A sample corresponding interferogram from a FTIR spectrometer is shown in *Fig. 2-3a*, which can be processed through a fast Fourier transform (FFT) based on the Mertz method to produce an IR spectrum (*Fig. 2-3b*).[37] However, the resulting signal can suffer from fringe interference from the light interaction through the sample. Another Fourier transform can be applied to the spectrum to visualize the fringe interference, which can be selectively removed through applying a low pass filter on the window shown by the dotted line in *Fig. 2-3c*. The IR spectrum is then reconstructed with the low pass filter applied to produce the cleaned IR spectrum shown in *Fig. 2-3d*. In an image, this process is applied to obtain and clean the IR spectrum for each of its pixels.

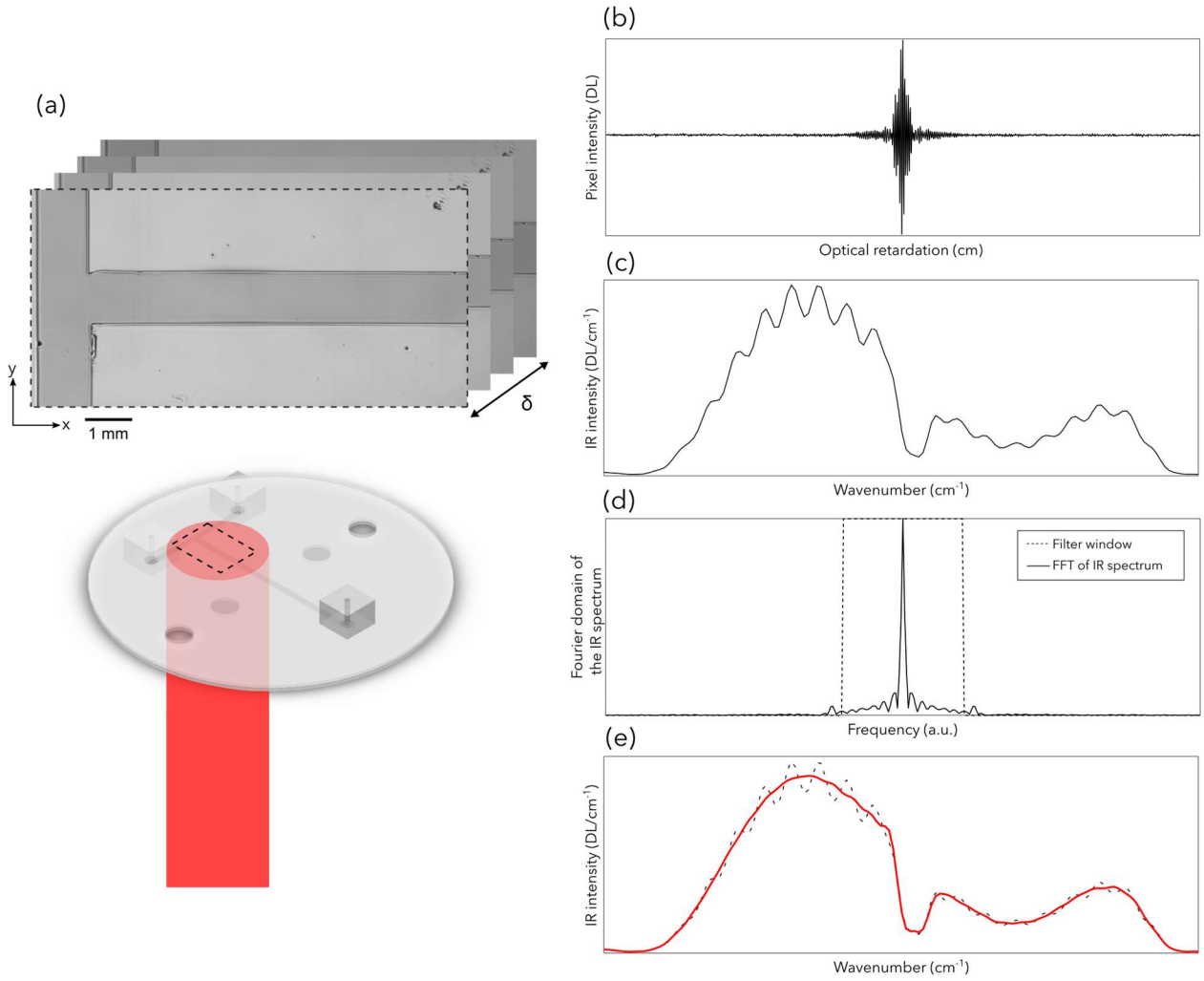

Fig. 2-3: The image processing routine for (a) a sample image captured by a FTIR spectrometer of a microfluidic T-channel cell. The spectrometer produces an (b) interferogram, which is converted into (c) an IR spectrum through a FFT based on the Mertz method.[37] *The IR spectrum suffers from fringe interference artifacts, for which a second FFT is applied to visualize (d) the frequency range that the artifacts occur for. This range is filtered for the wavenumbers in the filter window shown in (d) as indicated with the dotted line. After applying the filter, the (e) cleaned IR spectrum is produced.*

2.2.2 Infrared thermography

2.2.2.1 Working principles

Infrared thermography is used to capture images of a source that radiates electromagnetic waves, from which the temperature of the source can be determined. Other common techniques or tools for measuring temperature are often invasive techniques – requiring contact with the sample – which affects the temperature of that sample. Thermography circumvents these issues as it is a contactless and non-invasive technique, consequently enabling the temperature characterization of samples at a distance without affecting them. In another facet, when compared to other radiative imaging techniques (e.g. X-ray- and neutron-based), the radiation emitted from thermography is safe for the user and can therefore be utilized for extended periods of time without health hazards. These advantages make thermography an effective tool for a wide range of applications.[38–41] However, infrared thermography is not a perfect technique, as it is highly dependent on the following working conditions of the setting that must be accounted for: temperature, airflow, and humidity. Additionally, achieving high spatial and temporal resolutions with thermography is accompanied by expensive price tags.

2.2.2.2 Thermal image processing

Images captured through thermography are assigned colors pertaining to the intensity of emitted radiation from the sources in the image. Consequently, the unit of pixels within thermal images are unitless [-] and expressed as the digital level (DL). The thermal radiation emitted from a sample (ϵ_{sample}) can be isolated as the difference in DL between the DC component from the camera's sensor (ϵ_{DC}) and the proper emission in the captured image (ϵ_{image}).

$$\boldsymbol{\epsilon_{DL,sample}(x,y) = \epsilon_{DL,image}(x,y) - \epsilon_{DL,DC}(x,y)} \qquad \textit{Eq. 2-2}$$

Then a thermal calibration can be performed to quantify the relation between temperature and DL.[42] The DC component from the camera's sensor (ϵ_{DC} [-]) can be determined by acquiring a background image that blocks external signals from the sensor. This can be achieved by blocking the sensor with a material that completely attenuates IR light (for example a material covered with a suitable black paint).

When an IR camera is coupled with a FTIR spectrometer, the captured images contain information from both techniques and can be summarized through the following equation that combines *Eq. 2-1* and *Eq. 2-2*.

$$\boldsymbol{I_{tot} = \epsilon_{DL,image}(x,y) + I_{DC} + I_{AC}(x,y,\delta)} \qquad \textit{Eq. 2-3}$$

The thermal component (ϵ_{image}) can be isolated by blocking the IR beam from the FTIR spectrometer by a material that completely attenuates IR light. Once the DC component from the camera's sensor (ϵ_{DC}) is measured, and *Eq. 2-2* can be used to determine the thermal field of the sample (ϵ_{sample}).

Thus, with the combination of an IR camera and a FTIR spectrometer, the mass and heat transport within a sample can be determined through measuring its IR spectra and thermal fields. To summarize, the IR spectrum can be determined from I_{tot} by first removing the thermal component, and then by using the image processing method described in *Section 2.2.1.2* (also shown in *Fig. 2-3*). The thermal component of the sample (ϵ_{sample}) can be determined through the difference of the proper emission in the captured image (ϵ_{image}) and the DC component of the camera's sensor (ϵ_{DC}).

2.3 Chapter summary

In this chapter, a brief overview of microfluidics was discussed. Next, the potential for characterization of mass and heat transfer within these devices through IR spectroscopic and thermography techniques was presented. When fabricating a microfluidic chip for IR characterization, considerations for several parameters such as optical transparency, chemical compatibility, and ease of fabrication were discussed. Then, the working principles and image processing routines for these techniques were each detailed, with the relevant image processing equations. The following chapter will be dedicated to the application of these techniques through a semi-transparent to IR light microfluidic reactor. Specifically, mass transfer between two acid-base reactions in this microfluidic chip will be investigated through FTIR spectroscopy, and then the exothermic heat generated from these reactions will be experimentally quantified through IR thermography.

3 Heat and mass transfer visualization of an exothermic acid-base microfluidic reactor using infrared thermo-spectroscopy

3.1 Introduction

In this chapter, a microfluidic reactor was developed for visualization via operando infrared (IR) thermo-spectroscopy. The microfluidic reactor is semi-transparent in the mid-wave IR (MWIR) spectrum with a thin channel height that allows for the characterization of chemical species diluted with water, which strongly attenuates IR light. The experimental IR thermo-spectroscopy setup was achieved by coupling a Fourier transform infrared (FTIR) spectrometer with a MWIR camera. This experimental setup was used to characterize heat and mass transport of an exothermic acid-base reaction within the microfluidic reactor. The obtained experimental results were cross-validated to an advection-diffusion model, which was developed in collaboration with the SIMFI group at I2M using the in-house Notus computational fluid dynamics (CFD) software.[43] The fabrication techniques and experimental setup used here acted as an important intermediate step towards achieving transmission-based IR characterization in microfluidic polymer electrolyte membrane water electrolyzers via IR techniques.

3.2 Methods

3.2.1 Transparent microfluidic reactor

The materials and design of the microfluidic reactor were selected and optimized for optical transparency in the MWIR spectrum, and to reduce the effective path length of the incident IR beam. The reactor features two sapphire wafers with a polydimethylsiloxane (PDMS) gasket inserted between them (*Fig. 3-1*). Each sapphire wafer (Siegert Wafers) has a diameter of 50.8 mm (2”) and a thickness of 250 μm. The sapphire wafers and the PDMS gasket each have two 4 mm diameter holes removed, which were spaced 36 mm apart for alignment. The top sapphire wafer has additional 2 mm diameter holes removed for the inlets and outlet. The PDMS gasket (PF-X0, Gel-Pak) is a commercially available 40 μm thick film. The PDMS gasket was cut to the same diameter of the wafers and a T-shaped channel was removed via a plotter cutter (Graphtec). The mixing channel of the removed T-shaped pattern featured dimensions of 1.125 mm in width,

40 µm in height, and 30 mm in length. PDMS blocks with holes punched through them were prepared to serve as tubing inlet and outlet connectors.

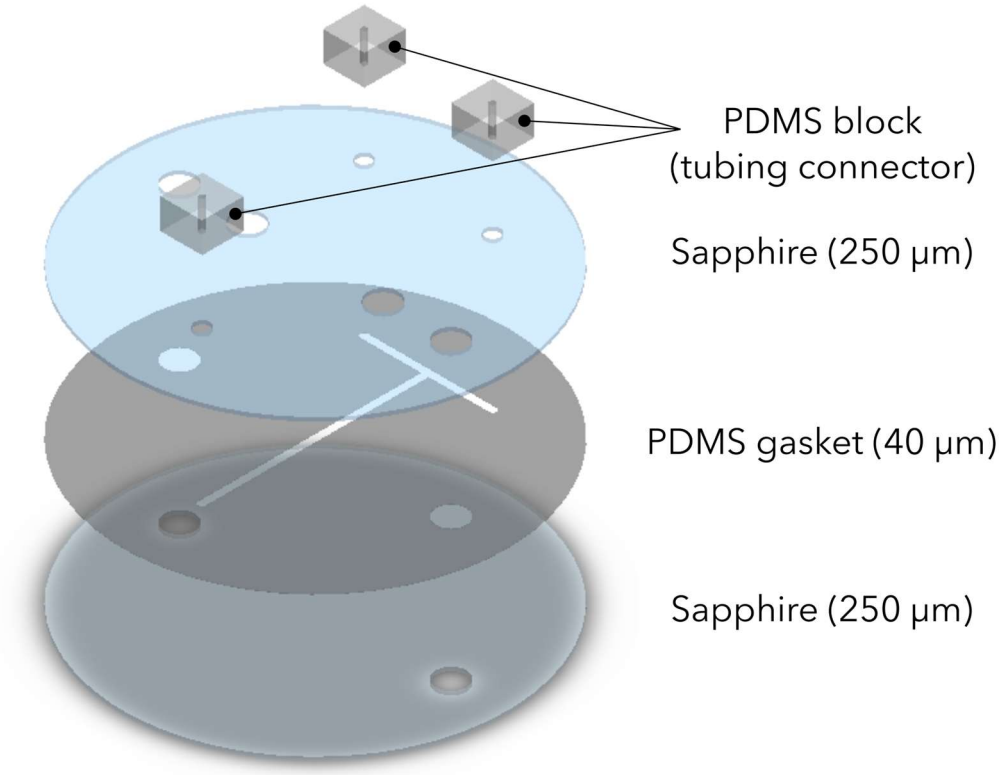

Fig. 3-1: Schematic of each component that the microfluidic reactor is comprised of.

The microfluidic chip was assembled by first positioning the alignment holes of the PDMS gasket to those of the bottom sapphire wafer in an isopropanol (IPA) bath. The IPA bath was used in the alignment step to reduce the friction between layers and because IPA could be easily removed later through evaporation. Once aligned, these components were inserted into a vacuum chamber, which was used for 30 min to adhere these layers together by evaporating any remaining IPA and removing any gas between the layers. Upon removal from the vacuum chamber, the half-built chip was inserted into an oven set to 65 °C for 1 h. Next, the top sapphire wafer was adhered to the assembly through the same process. Finally, the PDMS blocks were aligned to the holes and pressed onto the top sapphire wafer. Epoxy was used to irreversibly bond the PDMS blocks to the

sapphire wafer, then the microfluidic chip was left in the same oven set to 65 °C overnight for completion.

3.2.2 Experimental conditions

The microfluidic chip was used to investigate two exothermic acid-base mixing reactions for this study. The first reaction (*Eq. 3-1*) was between hydrochloric acid (HCl) and sodium hydroxide (NaOH) to form sodium chloride (NaCl), and the second reaction (*Eq. 3-2*) was between sulfuric acid (H_2SO_4) and NaOH to form sodium sulfate (Na_2SO_4).

$$\mathbf{HCl + NaOH \rightleftharpoons NaCl + H_2O} \qquad \textit{Eq. 3-1}$$

$$\mathbf{H_2SO_4 + 2NaOH \rightleftharpoons Na_2SO_4 + 2H_2O} \qquad \textit{Eq. 3-2}$$

Prior to the imaging experiment, pre-mixed salt solutions of of 1.0 mol L^{-1} NaCl and 0.5 mol L^{-1} Na_2SO_4 were prepared and saved for an imaging calibration step later. These solutions were prepared by mixing 2.0 mol L^{-1} HCl solution (Titripur, Sigma Aldrich) with 2.0 mol L^{-1} NaOH (Titripur, Sigma Aldrich) to produce 1.0 mol L^{-1} NaCl, and by mixing 1.0 mol L^{-1} H_2SO_4 with 2.0 mol L^{-1} NaOH to produce 0.5 mol L^{-1} Na_2SO_4. The concentrations of the salt products are half of those shown by their respective molar coefficients in *Eq. 3-1* and *Eq. 3-2*. For example, if the same volume of acid and base reactants are combined (e.g. 100 mL of each), the total number of moles of the produced salt solution would remain as shown in the above equations. While the number of moles remains the same as above, the total volume of the salt solution would be doubled (e.g. 200 mL), and therefore its concentration halved.

In the literature, the change between mass diffusivity and thermal diffusivity of each chemical species presented in this study varies by two orders of magnitude.[44,45] Consequently, the mixing channel flow rate was varied over two orders of magnitude for each chemical reaction (*Tab. 3-1*) such that the rates of mass and thermal diffusion could be compared between these flow rates. The flow rates prescribed in *Tab.* ***3-1*** were for the mixing channel, and to achieve these flow rates, reactants were delivered to the microfluidic chip at half of the flow rates shown.

Tab. 3-1: Experimental flow rates and channel velocities of reactants in the mixing channel for each chemical reaction.

Flow rate in mixing channel $\boldsymbol{q}$ ($\mu L\ min^{-1}$)	Velocity in main channel $\boldsymbol{v}$ ($mm\ s^{-1}$)
3.0	1.1
30.0	11.1
300.0	111.1

3.2.3 Imaging setup

Two configurations of the experimental setup were used to image heat and mass transport in the microfluidic reactor during operation. The first configuration used the IR beam produced by the FTIR spectrometer (*Fig. 3-2a*) and the second configuration was in absence of the beam to capture the proper emission of the sample (*Fig. 3-2b*). The FTIR spectrometer (ThermoFisher Scientific Nicolet iS50) produced a collimated beam for investigating the multispectral absorbance of each species in the microfluidic reactor across wavelengths from 2.5 µm to 25 µm (or wavenumbers of 4000 cm^{-1} to 400 cm^{-1}, respectively). A mirror was used to redirect the beam to the microfluidic chip. The beam was attenuated by the microfluidic chip, and was then captured by a MWIR camera (FLIR SC7000 InSb mid-IR). The images captured by the IR camera were comprised of two components: (1) the signal from the captured IR beam and (2) the proper emission of the sample. The signal from the captured IR beam was used to produce an image containing interferograms at each pixel. The interferograms were processed through a Fourier transform to obtain the multi-spectral IR images. This experimental setup coupled with the microfluidic chip enabled the visualization of the spectral range between 3 µm and 5 µm wavelengths (or 3333 cm^{-1} and 2000 cm^{-1} wavenumbers, respectively) and was used to capture images of the chemical reactions presented *Eq. 3-1* and *Eq. 3-2* during steady-state. The proper emission of the sample was captured by the IR camera to quantify the heat generated at the interface of the exothermic reactions. During experiments and image acquisition, the temperature of the chip was monitored through a custom

designed copper thermistor (Captec, model shown in *Appendix A*). The thermistor was designed to have the same diameter as the microfluidic reactor and was directly inserted underneath the microfluidic chip on the stage.

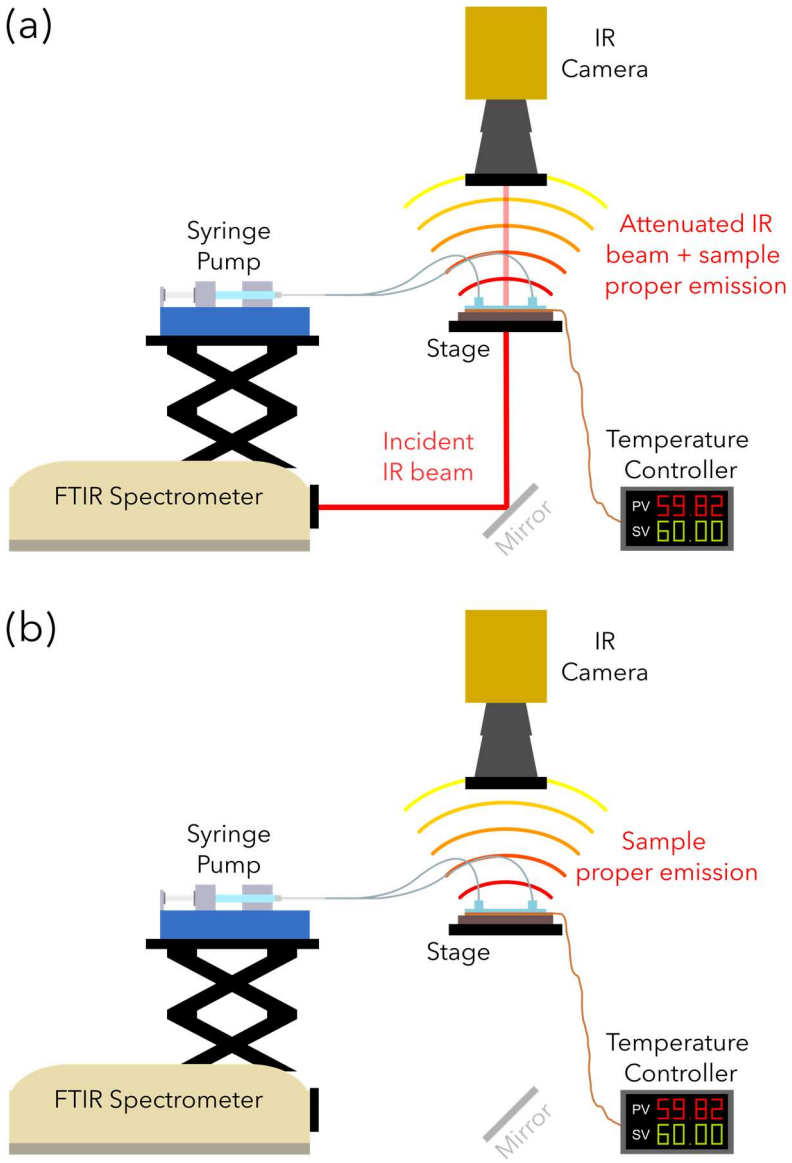

Fig. 3-2: The (a) IR spectroscopy and (b) IR thermography experimental setups for the visualization of heat and mass transfer produced by the exothermic chemical reactions in the microfluidic reactor. The IR thermography setup captures the proper emission of the microfluidic reactor in absence of the IR beam.

3.2.4 Image processing for concentration fields

For the first imaging configuration with the IR beam on, four sets of three images were captured per experimental condition shown in *Tab. 3-1*. First, HCl was supplied to the mixing channel through both inlets at the lowest experimental flow rate. After flowing for 5 min, three images of 1300 frames were acquired with an integration time of 750 µs and a framerate of 150 Hz. This process was repeated to acquire images at each experimental flow rate and for each chemical species (HCl, H_2SO_4, NaOH, NaCl, and Na_2SO_4) at the respective concentration prescribed in *Section 3.2.2*. Next, the same process was repeated to acquire images of each reaction (*Eq. 3-1* and *Eq. 3-2*) and at each experimental flow rate. These images were used to determine the multispectral absorbance field through the Beer-Lambert Law, shown below.

$$\boldsymbol{A(x,y,\lambda) = -\log\big(\Gamma(x,y,\lambda)\big) = -\log\left(\frac{I(x,y,\lambda)}{I_0(x,y,\lambda)}\right)} \qquad \textit{Eq. 3-3}$$

where A is the multispectral absorbance field, Γ is the multispectral transmittance field, I is the sample image, and I_0 is the reference image. The multispectral absorptivity coefficients were then determined for HCl, H_2SO_4, NaOH, NaCl, and Na_2SO_4 over a cropped wavelength range (3.79 µm to 4.16 µm), where each chemical species has a unique absorbance signature:

$$\boldsymbol{A(x,y,\lambda) = \sum_i \mu_i(x,y,\lambda) C_i(x,y)} \qquad \textit{Eq. 3-4}$$

where μ_i [L mol^{-1}] is the multispectral absorptivity coefficient for chemical species i and C_i [mol L^{-1}] is the concentration field for the respective chemical species. Images with the channel filled completely with each chemical species were acquired for calibrating their respective multispectral absorptivity coefficients.

The multispectral absorptivity coefficient (μ) was then determined for each chemical species through *Eq. 3-4* by using the previously acquired calibration images of each chemical solution. The multispectral absorptivity coefficients of each chemical species could then be used in combination with acquired images of the multispectral absorbance fields (A) to derive concentration fields (C) of each chemical species. Next, the law of mass conservation (as shown in *Eq. 3-5* and *Eq. 3-6* for *Eq. 3-1* and *Eq. 3-2*, respectively) was considered for any pixel area of the mixing channel for the respective chemical reaction.

$$\boldsymbol{C_0 = C_{HCl} + C_{NaOH} + 2C_{NaCl} = 2\ mol\ L^{-1}} \qquad \textit{Eq. 3-5}$$

$$\boldsymbol{C_0 = 2C_{H_2SO_4} + C_{NaOH} + 4C_{Na_2SO_4} = 2\ mol\ L^{-1}} \qquad \textit{Eq. 3-6}$$

where C_0 [mol L^{-1}] is the total concentration of chemicals for any pixel area in the channels. *Eq. 3-4* and *Eq. 3-5*/*Eq. 3-6* were then combined by substituting the acid concentration term (C_{HCl} and $C_{H_2SO_4}$) and rewritten into matrix form to consider the multispectral aspect of the images as shown in *Eq. 3-7*/*Eq. 3-8*, respectively, which could then be simplified to *Eq. 3-9*.

$$\begin{pmatrix} \boldsymbol{A^{\lambda_1} - \mu_{HCl}^{\lambda_1} C_0} \\ \boldsymbol{\vdots} \\ \boldsymbol{A^{\lambda_N} - \mu_{HCl}^{\lambda_N} C_0} \end{pmatrix} = \begin{bmatrix} \boldsymbol{\mu_{NaOH}^{\lambda_1} - \mu_{HCl}^{\lambda_1}} & \boldsymbol{\mu_{NaCl}^{\lambda_1} - 2\mu_{HCl}^{\lambda_1}} \\ \boldsymbol{\vdots} & \boldsymbol{\vdots} \\ \boldsymbol{\mu_{NaOH}^{\lambda_N} - \mu_{HCl}^{\lambda_N}} & \boldsymbol{\mu_{NaCl}^{\lambda_N} - 2\mu_{HCl}^{\lambda_N}} \end{bmatrix} \cdot \begin{pmatrix} \boldsymbol{C_{NaOH}} \\ \boldsymbol{C_{NaCl}} \end{pmatrix} \qquad \textit{Eq. 3-7}$$

$$\begin{pmatrix} \boldsymbol{2A^{\lambda_1} - \mu_{H_2SO_4}^{\lambda_1} C_0} \\ \boldsymbol{\vdots} \\ \boldsymbol{2A^{\lambda_N} - \mu_{H_2SO_4}^{\lambda_N} C_0} \end{pmatrix} = \begin{bmatrix} \boldsymbol{2\mu_{NaOH}^{\lambda_1} - \mu_{H_2SO_4}^{\lambda_1}} & \boldsymbol{\mu_{Na_2SO_4}^{\lambda_1} - 2\mu_{H_2SO_4}^{\lambda_1}} \\ \boldsymbol{\vdots} & \boldsymbol{\vdots} \\ \boldsymbol{2\mu_{NaOH}^{\lambda_N} - \mu_{H_2SO_4}^{\lambda_N}} & \boldsymbol{\mu_{Na_2SO_4}^{\lambda_N} - 2\mu_{H_2SO_4}^{\lambda_N}} \end{bmatrix} \cdot \begin{pmatrix} \boldsymbol{C_{NaOH}} \\ \boldsymbol{2C_{Na_2SO_4}} \end{pmatrix} \qquad \textit{Eq. 3-8}$$

$$\boldsymbol{A = \mu C} \qquad \textit{Eq. 3-9}$$

Finally, *Eq. 3-9* could be rearranged such that the concentrations of the base reactant and the salt product could be determined from the images at any pixel through the least squares inverse method.

$$\boldsymbol{C = [\mu^T \mu]^{-1} \mu^T A} \qquad \textit{Eq. 3-10}$$

With the concentration fields of the base and salt species known, the concentration field of the acid species can then be determined back through *Eq. 3-4*. Thus, the concentration field for each chemical species was acquired through processing the multispectral absorbance images.

3.2.5 Differences in concentration field processing for each reaction

The image processing routine in the previous section differs depending on the chemical reaction of interest. Here, the general case for the acidic solutions denoted as a (for HCl and H_2SO_4), the basic solution denoted as b (for NaOH), and product salt solutions denoted as c (for NaCl and Na_2SO_4) will be considered to simplify the explanation for each chemical reaction. Each image with the channel filled with one solution (I_a, I_b, and I_c) was processed through the modified version of *Eq. 3-3* as shown below, each with reference to I_a as the background image (denoted as $I_{a(bkg)}$ below) to obtain the multispectral absorbance field of each chemical species with reference to the to the acid species.

$$\boldsymbol{A_{a/a}(x,y,\lambda) = -\log\left(\frac{I_a(x,y,\lambda)}{I_{a(bkg)}(x,y,\lambda)}\right)} \qquad \textit{Eq. 3-11}$$

$$\boldsymbol{A_{b/a}(x,y,\lambda) = -\log\left(\frac{I_b(x,y,\lambda)}{I_{a(bkg)}(x,y,\lambda)}\right)} \qquad \textit{Eq. 3-12}$$

$$\boldsymbol{A_{c/a}(x,y,\lambda) = -\log\left(\frac{I_c(x,y,\lambda)}{I_{a(bkg)}(x,y,\lambda)}\right)} \qquad \textit{Eq. 3-13}$$

Absorbance fields were determined with reference to the acid reactant because the acid is used as the substituted component in *Eq. 3-7* and *Eq. 3-8*. These relative absorbance fields $A(x,y,\lambda)$ were averaged in the x and y directions to acquire μ for each solution as a function of wavelength ($A(\lambda)$). The multispectral attenuation coefficient μ was determined with reference to the acidic species as well for the wavelength range of 3.79 μm to 4.16 μm shown in *Fig. 3-3*. This wavelength range was tested and found to distinguish the acid, base, and salt species the best for all investigated wavelengths of both chemical reactions. However, while this was the best wavelength range for distinguishing chemical species in the acquired wavelength ranges (3 μm to 5 μm for the used combination of experimental setup and microfluidic chip), the profiles are not necessarily ideal for distinguishing acid and base species. Specifically, comparing the profile of the base species NaOH to the acid species HCl (*Fig. 3-3a*) and H_2SO_4 (*Fig. 3-3b*), the profile relative to HCl is less uniform (or linear) than the one relative to H_2SO_4, thus making it harder to distinguish NaOH from HCl than H_2SO_4 for the inverse method.

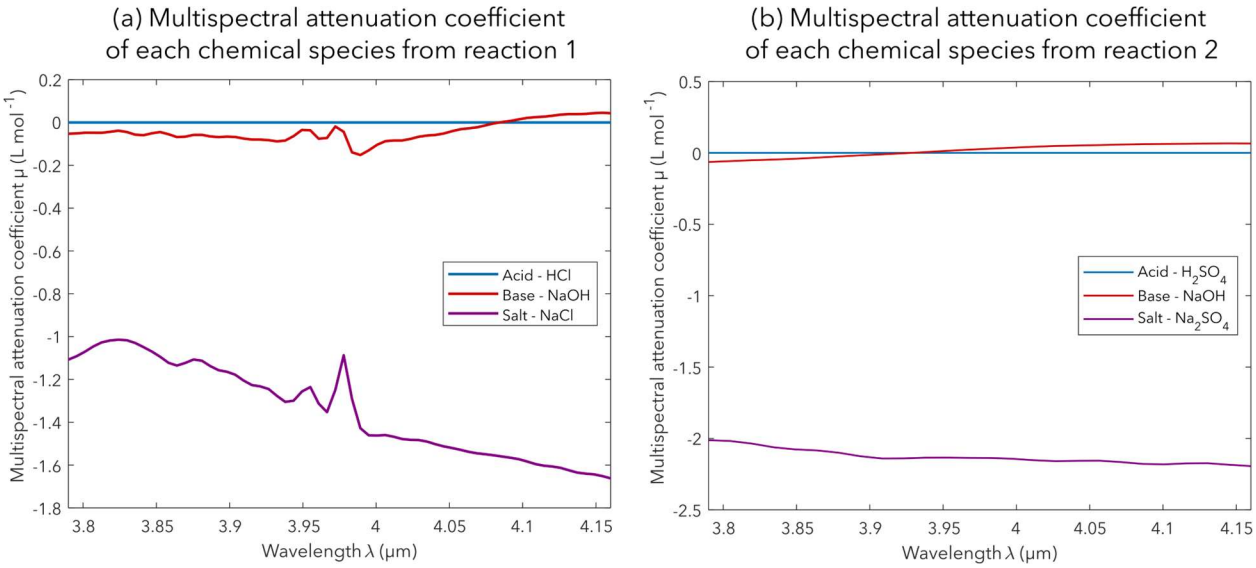

Fig. 3-3: The multispectral attenuation coefficient μ obtained for all chemical species relative to the acid reactant in (a) reaction 1 as described in Eq. 3-1 and (b) reaction 2 as described in Eq. 3-2 between the wavelengths of 3.79 μm to 4.16 μm. Since absorbance fields use acid images as the background/reference images, μ for the acid species is always 0 and the μ for base and salt species are in reference to the acid species.

The molar fraction coefficient of each chemical is significant to consider, as it directly affects C_0, which is used to determine the absorbance A. As a result, the molar fraction coefficients for each chemical species are denoted as m_{rx}, for which the coefficient for each species is shown below.

Tab. 3-2: The molar fraction coefficients ($\mathbf{m_{rx}}$) for use in Eq. 3-14 to Eq. 3-16. These values are the molar coefficients shown in Eq. 3-5 and Eq. 3-6 for the respective chemical reaction.

Chemical species	m_{rx}	
	Reaction 1 (*Eq. 3-1*)	Reaction 2 (*Eq. 3-2*)
Acid (a, *Eq. 3-14*)	1	2
Base (b, *Eq. 3-15*)	1	1
Product salt (c, *Eq. 3-16*)	2	4

Subsequently, these images were processed through the rearranged form of *Eq. 3-9* for the general case of each acid species, the basic species, and each product salt species with reference to the respective acid species.

$$\boldsymbol{\mu_{a/a}(\lambda) = \frac{\overline{A}_{a/a}(\lambda)}{C_0/m_{rx}} = \frac{A_{a/a}(x,y,\lambda)}{C_0/m_{rx}}} \qquad \textit{Eq. 3-14}$$

$$\boldsymbol{\mu_{b/a}(\lambda) = \frac{\overline{A}_{b/a}(\lambda)}{C_0/m_{rx}} = \frac{A_{b/a}(x,y,\lambda)}{C_0/m_{rx}}} \qquad \textit{Eq. 3-15}$$

$$\boldsymbol{\mu_{c/a}(\lambda) = \frac{\overline{A}_{c/a}(\lambda)}{C_0/m_{rx}} = \frac{A_{c/a}(x,y,\lambda)}{C_0/m_{rx}}} \qquad \textit{Eq. 3-16}$$

Next, the multispectral absorbance field of the reaction ($A_{rx/a}$) from the reaction image I_{rx} with reference to the acid background/reference image ($I_{a(bkg)}$) was processed through the Beer Lambert Law modified from *Eq. 3-3* as shown below.

$$\boldsymbol{A_{rx/a}(x,y,\lambda) = -\log\left(\frac{I_{rx}(x,y,\lambda)}{I_{a(bkg)}(x,y,\lambda)}\right)} \qquad \textit{Eq. 3-17}$$

Then, the resulting absorbance field with reference to the respective acidic species was cropped to the same wavelength range as before and averaged over it (3.79 μm to 4.16 μm). This wavelength range is selected because the absorbance spectra of each chemical species (a, b, and c) can be best distinguished in this wavelength range for the spectral range used in this experiment. Finally, the concentration fields of each chemical species were determined from these absorbance spectra through *Eq. 3-10*. However, the resulting concentration fields may contain concentration values that were slightly offset due to minor differences in the environmental conditions between the image acquisition times. To compensate, C_a and C_b were linearized to the inlet channels, as chemicals in those regions have known prescribed concentrations. Finally, C_c was recomputed from the linearized acid and base concentration fields through rearranging *Eq. 3-5* and *Eq. 3-6*.

$$\boldsymbol{C_{NaCl} = \frac{1}{2}(C_0 - C_{HCl} - C_{NaOH})} \qquad \textit{Eq. 3-18}$$

$$\boldsymbol{C_{Na_2SO_4} = \frac{1}{4}\left(C_0 - 2C_{H_2SO_4} - C_{NaOH}\right)} \qquad \textit{Eq. 3-19}$$

3.2.6 Temperature measurements

In the second configuration with the IR beam off, the proper emission of the acid-base reactor was captured with the same MWIR camera. Before thermal image acquisition for each acid-base reaction, calibration images were acquired to convert the units of images from digital level (DL) [-] to temperature [°C]. Calibration images were acquired with the microfluidic chip on the stage and with the copper thermistor placed directly underneath the reactor to mimic experimental conditions (model shown in *Appendix A*). The thermistor was used for temperature measurement and control of the microfluidic chip through a proportional-integral-derivative (PID) controller (working principles of the PID described in *Appendix A*). For calibration images, the thermistor was first set to a temperature of 26 °C such that the temperature was slightly higher than the ambient temperature. A solution of 2.0 mol L^{-1} HCl was supplied to the reactor at 3 µL min^{-1} and 2000 frames of images were acquired. This was repeated for each mixing channel flow rate shown in *Tab. 3-1*. The temperature was then increased in 1 °C increments and additional images were acquired for each mixing channel flow rate and temperature increment until a temperature of 30 °C was achieved. This processes yielded a total of 15 image sets for temperature calibration using HCl as the electrolyte (*Fig.* ***3-4***). Each image set $T(x, y, frame)$ was cropped to the mixing channel and the DL was averaged in the x direction, y direction, and over all 2000 frames yielding $\bar{T}$. Given the small temperature range for this calibration and for experiments, a fit could be applied to determine the relationship between DL and temperature. The profiles are shown in *Fig.* ***3-4***, and appear to be linear, therefore a linear fit was used. The linear fit between the applied temperature and the averaged DL was applied to calculate linear calibration coefficients a_1 and a_2, for each flow rate.

$$\overline{T_{\iota,°C}} = \frac{\overline{T_{\iota,DL}} - a_2}{a_1} \qquad \textit{Eq. 3-20}$$

With these calibration coefficients known, the conversion of DL to temperature could be performed for all thermal images. This process was repeated for all chemical species present in either reaction at the prescribed concentrations. The thermal calibrations had negligible differences between chemical species, therefore the image sets containing HCl were used for the conversion of DL to temperature.

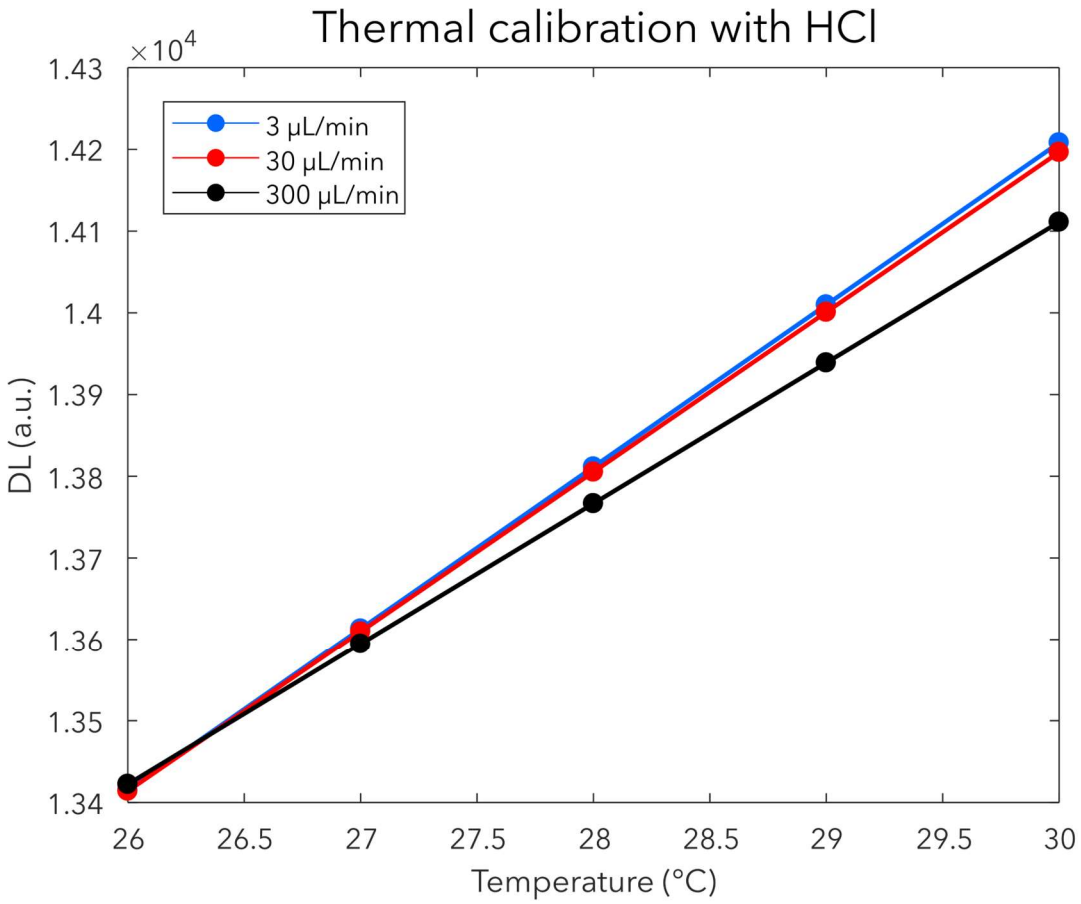

Fig. 3-4: Temperature calibration measurements from 26 °C to 30 °C for HCl at the three experimental flow rates.

After thermal calibration images were acquired and the calibration coefficients were determined, thermal images of the chemical reactions were captured. For each chemical reaction, two sets of 2000 frames each – steady state reaction images ($T_{rx,DL}$) and reference state images ($T_{ref,DL}$) – were captured. $T_{rx,DL}$ images were captured for each chemical reaction and at each flow rate presented in *Tab. 3-1*. $T_{bkg,DL}$ images of room temperature thermal images where the mixing channel was filled with the acid species of the respective chemical reaction were also acquired. DL images were converted to temperature through *Eq. 3-20*, and the final temperature field ($T_{\circ C}$) was determined as the difference between reaction images and the background images:

$$\boldsymbol{T_{\circ C}(x, y, frame) = T_{rx,\circ C}(x, y, frame) - T_{bkg,\circ C}(x, y, frame) + T_{RT}} \qquad \textit{Eq. 3-21}$$

where T_{RT} was the measured temperature from the copper thermistor that was acquired at the same time as image sets $T_{rx,\circ C}$. Since reaction image sets were assumed to be steady state in terms of temperature, they were averaged in the x direction, y direction, and over all 2000 frames as well.

3.3 Reactor model

The experimental results obtained in *Section 3.2* were cross-validated with the advection-diffusion model described in this section. This section will be dedicated to presenting the reactor model developed by Cédric Palka under the supervision of Arnaud Erriguible, and Stéphane Glockner. While the work presented in this section was not performed by the author of this thesis, it is presented briefly here for understanding and cross validation with experimental results. Only the chemical reaction between HCl and NaOH to produce NaCl was modelled (shown in *Eq. 3-1*).

A three-dimensional (3D) simulation was generated to model the heat and mass transfer in the acid-base reactor. Three equations were considered to model the reaction. First, the incompressible Navier-Stokes equation,

$$\begin{cases} \boldsymbol{\rho\left(\frac{\partial u}{\partial t} + u \cdot \nabla u\right) = \nabla \cdot (\mu \nabla u) - \nabla p} \\ \boldsymbol{\nabla \cdot u = 0} \end{cases} \qquad \textit{Eq. 3-22}$$

where ρ represents the density [kg m^{-3}], u represents the velocity field [m s^{-1}], and p represents pressure [Pa]. As the acid and base solutions were diluted with water, the fluidic properties of water were used unless specified otherwise (*Tab. **3-3***).

Tab. 3-3: Properties of the chemical solutions used in the model. Each chemical solution was modelled with a solute expansion coefficient, ϕ, of 0.[46,47]

Solution	Diffusion coefficient, $\boldsymbol{D}$ (m^2 s^{-1})	Molar mass, $\boldsymbol{M}$ (kg mol^{-1})	Concentration $\boldsymbol{C_i}$ (mol L^{-1})
HCl	$3.4 \cdot 10^{-9}$	$3.6 \cdot 10^{-2}$	2.0
NaOH	$2.1 \cdot 10^{-9}$	$4.0 \cdot 10^{-2}$	2.0
NaCl	$2.1 \cdot 10^{-9}$	$5.8 \cdot 10^{-2}$	1.0

The Navier-Stokes equation was computed with inlet flow rates that ranged over the conditions shown in *Tab. 3-1* and yielded a Reynolds number range of 0.077 to 7.72. Second, the energy conservation equation,

$$\boldsymbol{\rho C_p \left(\frac{\partial T}{\partial t} + u \nabla T\right) = \nabla \cdot (\kappa \nabla T) + S_T} \qquad \textit{Eq. 3-23}$$

where C_p represents the specific heat [J kg^{-1} K^{-1}], T represents temperature [K], κ represents the thermal conductivity [W m^{-1} K^{-1}], and S_T is the source term. The energy equation was computed with an initial ambient temperature of $T_0 = 300\ K$ and an enthalpy of reaction of $h_{NaCl} = 56 \cdot 10^3 J\ mol^{-1}$. Third, the advection-diffusion equation, by considering Fick's law for the diffusion part, is described by,

$$\boldsymbol{\frac{\partial C_i}{\partial t} + u \nabla C_i = \nabla \cdot (D_i \nabla C_i) + S_{C_i}} \qquad \textit{Eq. 3-24}$$

where C_i represents the concentration of species i [mol m^{-3}], D_i represents the molecular diffusion coefficient of species i [m^2 s^{-1}], and S_{C_i} is the source term. These three equations were coupled through the flow velocity field and the source terms S_T and S_{C_i}. The source terms can be expressed as:

$$\boldsymbol{S_T = h_{NaCl} k_f C_{HCl} C_{NaOH}} \qquad \textit{Eq. 3-25}$$

$$\boldsymbol{S_{C_i} = \gamma_i k_f C_{HCl} C_{NaOH}} \qquad \textit{Eq. 3-26}$$

where h_{NaCl} is the previously mentioned the enthalpy of reaction for the reaction presented here [kJ mol^{-1}], γ_i represents the creation (+1) and consumption (-1) of chemical species i,and k_f is the reaction kinetics coefficient [m^3 mol^{-1} s^{-1}]. A reaction kinetics coefficient of $k_f = 20\ m^3 mol^{-1} s^{-1}$ was used in this model. Additional parameters for cell components and chemical solutions used in the computational model are shown in *Tab. 3-3* and *Tab. 3-4*.

*Tab. 3-4: The properties of liquid water and solid PDMS and sapphire that were used to generate the model. The molar mass and dynamic viscosity were not utilized in the model for solid materials, which are denoted with *.*

Material	Molar mass, $\boldsymbol{M}$ (kg mol^{-1})	Dynamic viscosity, $\boldsymbol{\mu_{visc}}$ (kg m^{-1} s^{-1})	Density, $\boldsymbol{\rho}$ (kg m^{-3})	Specific heat, $\boldsymbol{C_p}$ (J kg^{-1} K^{-1})	Thermal conductivity, $\boldsymbol{\kappa}$ (W m^{-1} K^{-1})	Thermal expansion coefficient, $\boldsymbol{\alpha}$ (K^{-1})
Water	$18 \cdot 10^{-3}$	$1.0 \cdot 10^{-3}$	1000	4185	0.61	$2.06 \cdot 10^{-4}$
PDMS*			965	1460	0.15	$1 \cdot 10^{-4}$
Sapphire*			3.98	770	45	$6 \cdot 10^{-5}$

The proposed model was discretized and solved on a fixed Cartesian staggered grid through the parallel framework of the Notus CFD code.[43] To ensure the lowest computation times, a mix of implicit and explicit schemes were used depending on the Courant-Friedrichs-Lewy (CFL) conditions associated with each term of the equations. The Navier-Stokes equations were discretized with a second order implicit centered scheme for the non-linear and viscous stress terms. A stationary solution could thus be achieved quickly. For this equation, velocity was penalized to zero in the solid regions of the microfluidic chip (i.e. outside of the channels). Velocity and pressure coupling under the constraint of incompressibility was solved with the Timmermans time splitting method.[48] The advection term of the energy equation was solved with a Lax-Wendroff scheme with a Superbee flux-limiter,[49] as well as the advection term of the concentration equations. The diffusion term of the energy equation was solved with a second order centered implicit scheme whereas the terms for the concentration equations were solved with an explicit scheme because of more favorable CFL conditions. To consider conduction outside of the channels for the microfluidic chip, conductivity was geometrically interpolated at the interface between liquid and solid regions. Finally, the massively parallel Hypre-solver-library was used to compute the solutions of the linear systems of the Navier-Stokes and energy equations.[50]

The 3D simulations were modelled considering the channel dimensions of the microfluidic chip used in the experiments. The channel layer was sandwiched by two sapphire layers of 250 µm thickness to mimic the geometry of the experimental cell. The geometry of the model is presented

in *Fig. 3-5a*, where the reactor features a plate length L of 30 mm, a plate width W of 10 mm, a channel width l_c of 1.125 mm, a total height H of 540 µm, and channel height h of 40 µm. The boundary conditions for the "edges" of the model of any particular region are as shown in *Fig. 3-5b*.

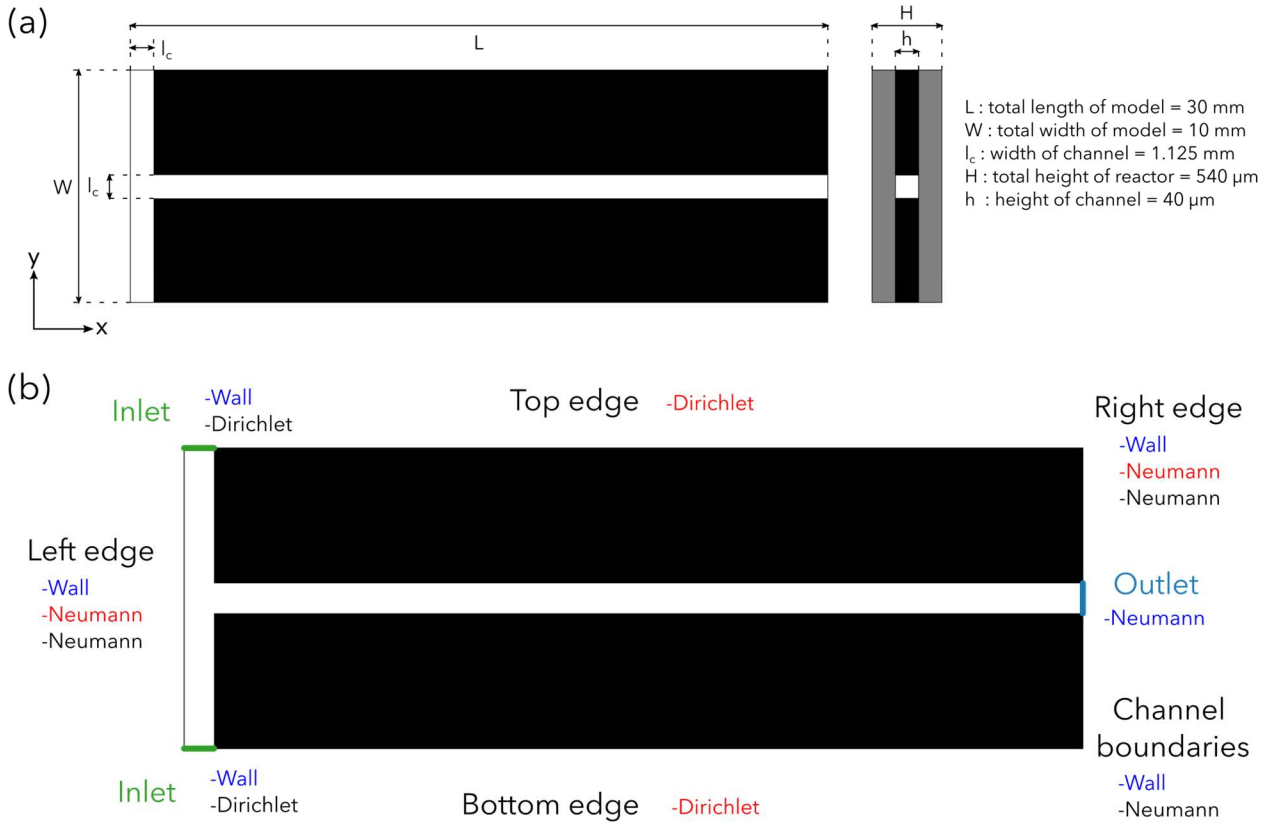

Fig. 3-5: (a) Geometric diagram of the simulated reactor with the channel is shown in white, PDMS insulation is shown in black, and sapphire support wafers are shown in grey. (b) The associated boundary conditions for which the model is computed. Blue boundary conditions are for the Navier-Stokes equation (Eq. 3-22), red boundary conditions are for the energy conservation equation (Eq. 3-23), and black boundary conditions are for the advection-diffusion equation (Eq. 3-24).

3.4 Results and discussion

3.4.1 Concentration fields and comparison with modelled results

The concentration fields and profiles for each chemical reaction and chemical species is shown for the lowest flow rate in *Fig. 3-6*. For the first chemical reaction between HCl and NaOH, the multispectral absorptivity coefficients (*Fig. 3-3a*) were more challenging for the inverse method to distinguish, which resulted in more noise observed for both the concentration fields and profiles shown in *Fig. 3-6a – d*. For the second chemical reaction between H_2SO_4 and NaOH, the multispectral absorptivity coefficients had more distinguishable profiles (*Fig. 3-3b*), which yielded clearer differences between the concentration fields and profiles shown in *Fig. 3-6e – h*. When recalling the multispectral absorptivity coefficients from *Fig. 3-3*, the profile of μ for the basic solution NaOH (used for both reaction) is more linear for the second reaction when compared to the first reaction. This is especially true at wavelengths closer to 4 μm, which impacts the results from the inverse method negatively. These behaviors will be described in more detail in a future section comparing the experimental results to the modelled results, where under-compensations in the HCl concentration measurements are observed with overcompensations in NaOH measurements.

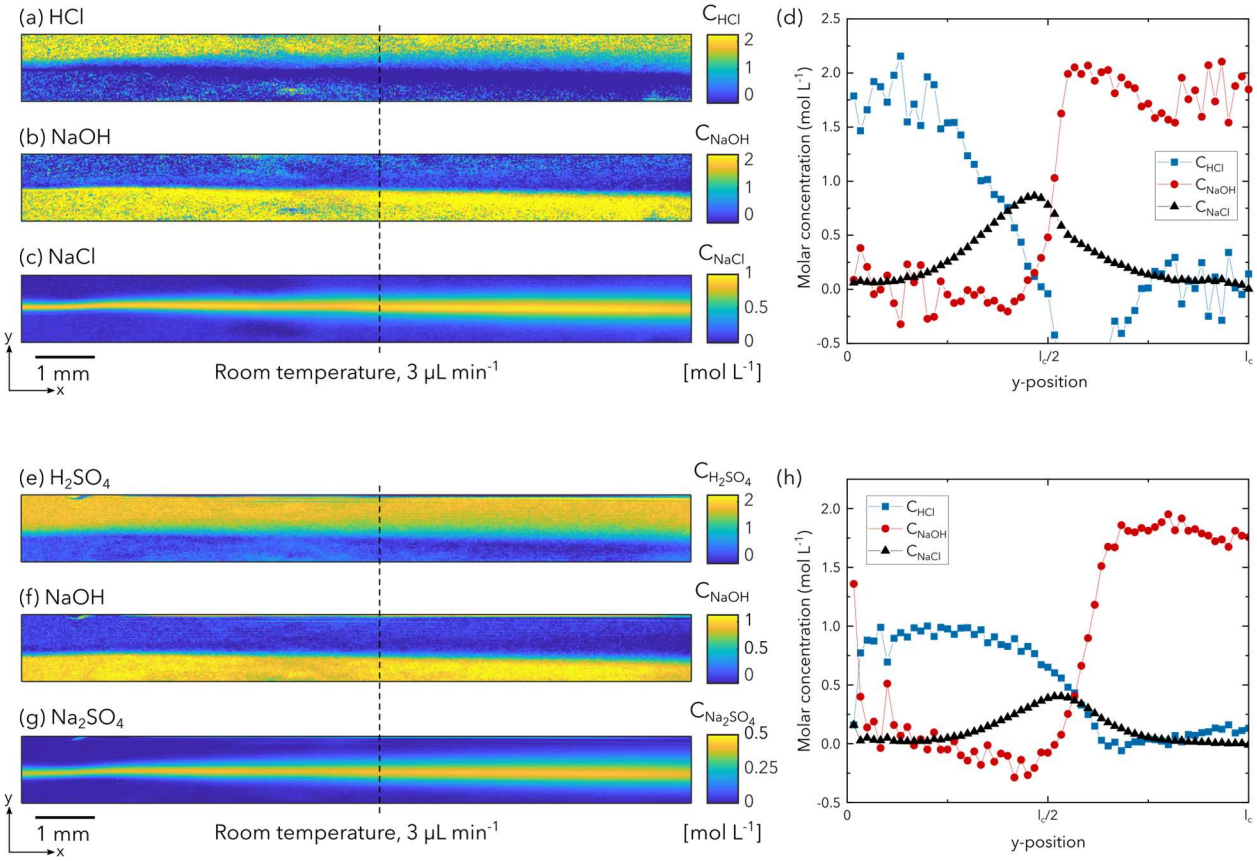

Fig. 3-6: The experimentally measured concentration fields for both the reaction between HCl and NaOH (a-d) and the reaction between H_2SO_4 and NaOH. The concentration fields for the reactions are shown for (a) HCl, (b) NaOH, (c) NaCl for the first reaction, and (e) H_2SO_4, (f) NaOH, and (g) Na_2SO_4 cropped to the entrance of the mixing channel at a flow rate of 3 µL min^{-1}. The corresponding molar concentration profiles of each species averaged over 10 columns centered around the dashed line for (a) to (c) and (e) to (g) for (d) the first chemical reaction and (h) the second chemical reaction, respectively.

The concentration of each chemical species in the simulation model was determined for the first chemical reaction and for each flow rate to draw comparisons with experimental results. Since numerical computations were not performed for the second chemical reaction shown in *Eq. 3-2*, only comparisons of experimental and numerical results for the first chemical reaction between HCl and NaOH to produce NaCl will be discussed. The numerical concentration fields and profiles for the same conditions presented in *Fig. 3-6a – d* are shown in *Fig. 3-7*.

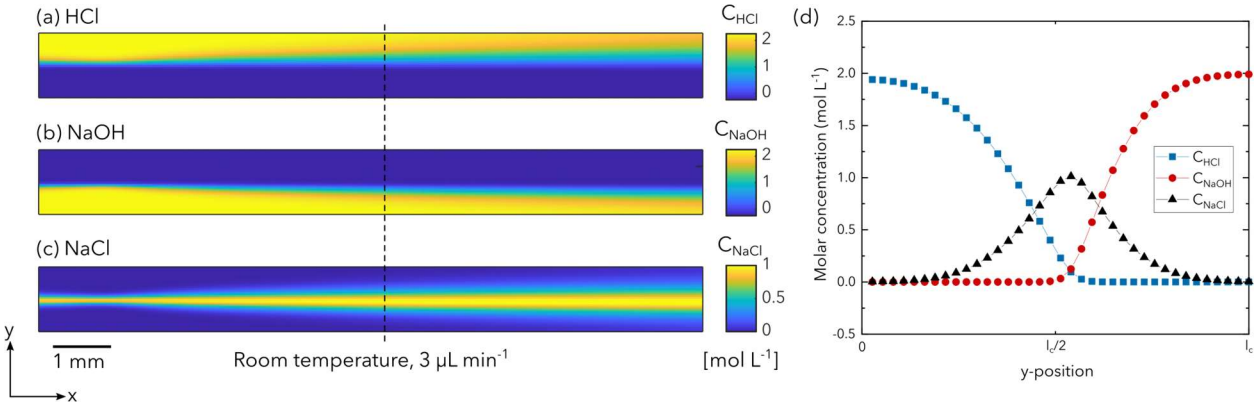

Fig. 3-7: The numerical concentration fields of (a) HCl, (b) NaOH, and (c) NaCl cropped to the entrance of the mixing channel at a flow rate of 3 µL min^{-1} and (d) the corresponding molar concentration profiles of each species averaged over 10 columns centered around the dashed line shown in (a) to (c).

The experimental trends followed the trends shown in the model, but with increased noise for the reactants. Although C_{NaCl} was determined after C_{HCl} and C_{NaOH}, it was the most accurate chemical species when compared to the model, as shown in *Fig. 3-8*. This is because the profile of the absorbance coefficient (μ) for NaCl could be distinguished from those of HCl and NaOH. Additionally, the absorbance profiles of HCl and NaOH were similar to each other in the working wavelength range of the MWIR camera, making the distinction between these two chemical species more challenging with the inverse method. These effects can be more clearly seen when the experimental concentration fields were overlaid onto the simulated concentration fields, as shown in *Fig. 3-8*. The regions where the processing method over-compensates can be observed for the basic solution of NaOH around a y-position of $l_c/2$ in *Fig. 3-8b*, and a similar under-compensation can be observed for the acid solution of HCl at the same position in *Fig. 3-8a*. These over- and under-compensations did not affect the concentration distribution of the product salt solution of NaCl shown in *Fig. 3-8c*. The comparison between these the two reactions through the processing method shows the importance of selecting chemical species with clearly distinguishable absorbance coefficients in the spectral range of interest.

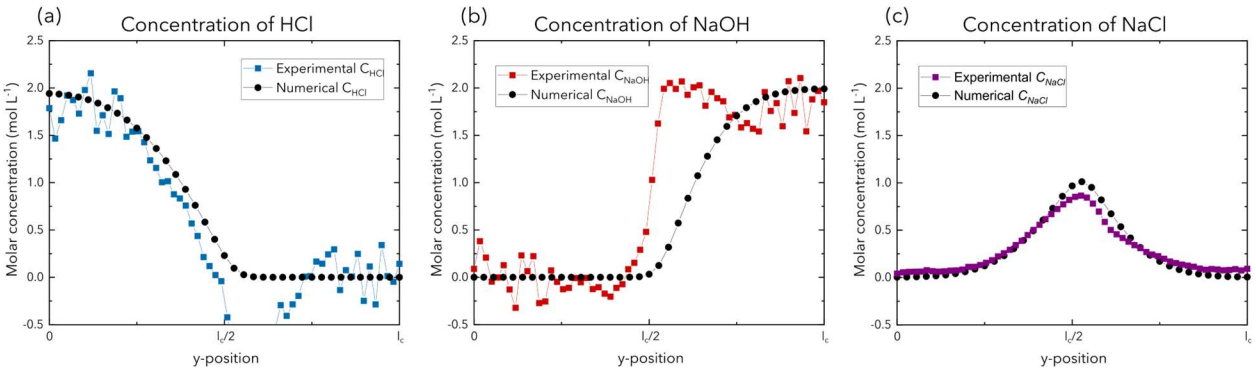

Fig. 3-8: The experimental concentration fields overlaid onto the simulated concentration fields for (a) HCl, (b) NaOH, and (c) NaCl.

The concentration profiles of NaCl were compared for experimental and numerical results to further evaluate the accuracy of the model. A comparison of the experimental and numerical C_{NaCl} results at each of the tested flow rates is shown in *Fig. 3-9*. The experimental concentration profiles were nearly identical to the numerical results, which validated the model for reproducing mass transport in the system. Moreover, the width of the diffusion cones in the experimental data were consistent with the simulated results at any x- position and across all tested flow rates.

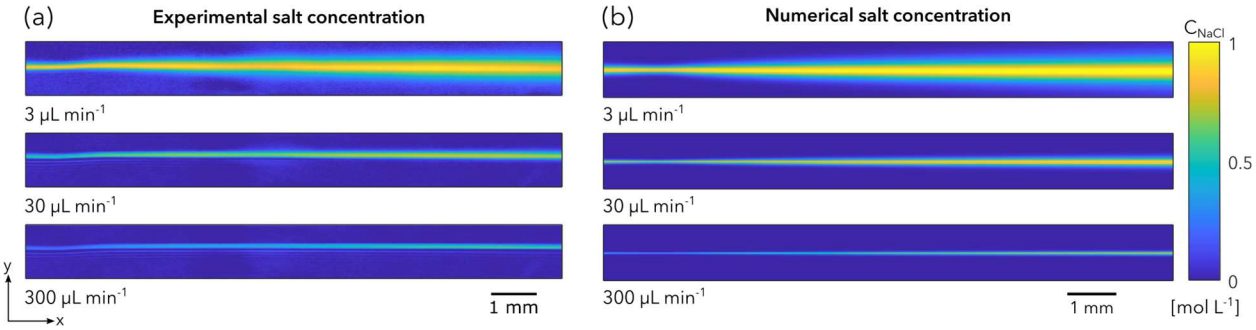

Fig. 3-9: The concentration fields of NaCl for the (a) experimentally measured data and the (b) numerical data at each of the tested flow rates.

3.4.2 Thermal fields and comparison with modelled results

In addition to comparisons between the concentration fields, the experimental thermal field images acquired as the proper emission of the sample were also processed and compared to the numerical thermal fields. At flow rates of 3 μL min^{-1} and 30 μL min^{-1}, heat produced by the exothermic reaction is at an order of magnitude that the camera was not sensitive enough to capture. However, at 300 μL min^{-1}, a noticeable variation in the thermal profile was observed at the inlet of the mixing channel. The experimental and numerical thermal fields were then compared at this flow rate, and are shown in *Fig. 3-10*. While these flow rates were initially chosen to compare the thermal diffusion pattern to the mass diffusion "cones" in the previous section, the thermal field profiles differed and did not resemble the conical shape observed for mass diffusion. This was attributed to the materials that the microfluidic chip is comprised of, as these materials are impermeable to mass transport, but not to heat transport. Sapphire in particular, which was used as the top and bottom wafer material, has the highest thermal conductivity of materials used to build the microfluidic chip.[51] However, the second reaction between H_2SO_4 and NaOH to produce Na_2SO_4 has a greater enthalpy of formation of liquid under standard conditions ($\Delta_f H°_{liquid}$) than that of the first reaction (-1356.38 kJ mol^{-1} for Na_2SO_4 compared to -385.92 kJ mol^{-1} for NaCl), producing a multiple of approximately 3.5 times more heat.[52] Consequently, this increase in reaction enthalpy produces temperatures in the chip that change the thermal profile observed in *Fig. 3-10c*, such that the temperature of the electrolyte in the mixing channel increases as it flows through the chip. As a result, the thermal distribution for the second reaction resembles that of a "cone" more than the first reaction.

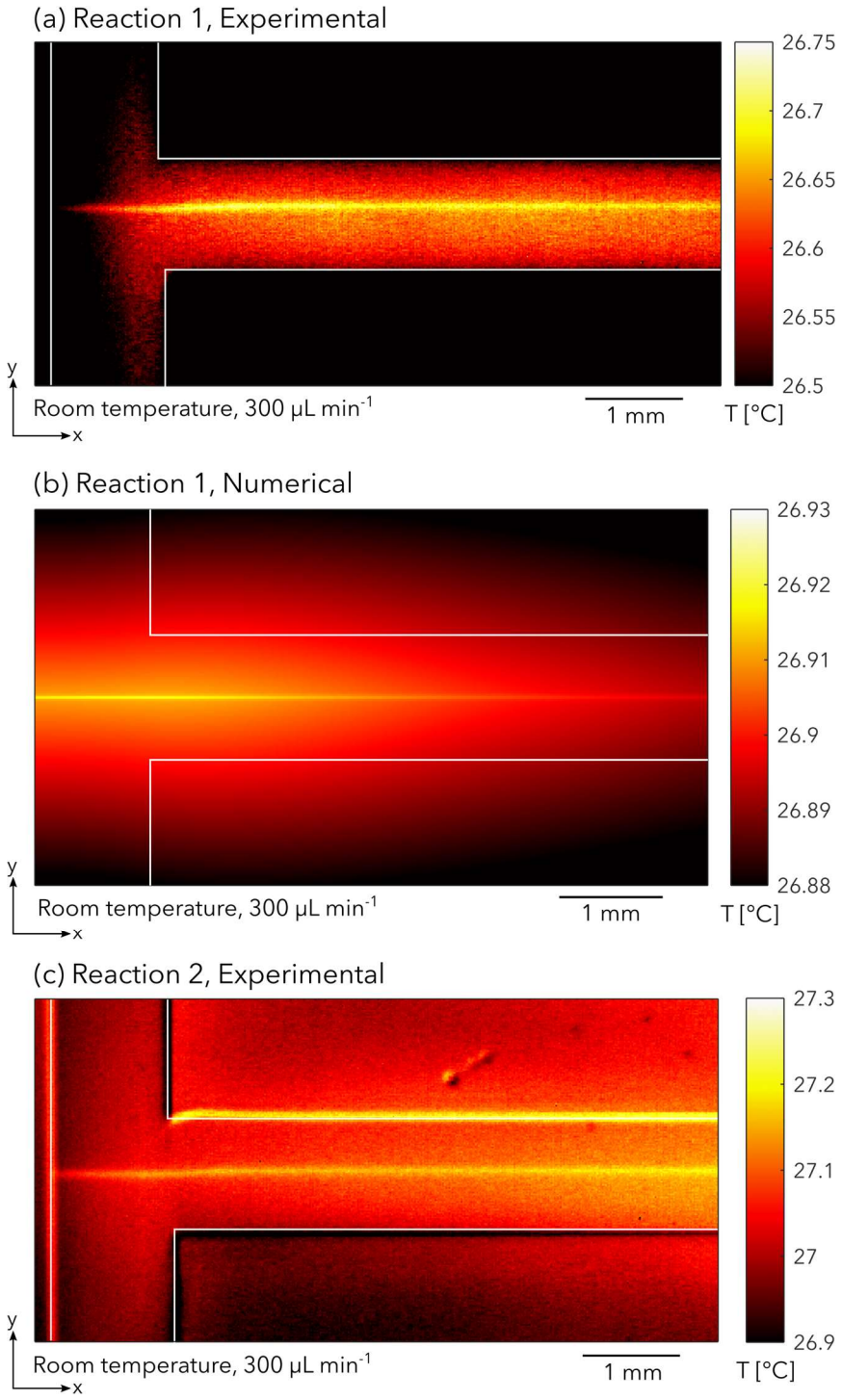

Fig. 3-10: The thermal fields for the (a) experimental results of the first reaction, (b) numerical results of the first reaction, and (c) experimental results of the second reaction at a flow rate of 300 µL min^{-1} in °C. The thermal field in (b) was produced as an average of all slices (through the plane of the image) computed from the simulation. A numerical simulation was not performed for the second reaction.

Thermal fields were not numerically modeled for the second chemical reaction shown in *Eq. 3-2*, therefore the subsequent comparisons between experimental and numerical results will only focus on the first chemical reaction between HCl and NaOH to produce NaCl (*Eq. 3-1*). The comparison between experimental and numerical thermal fields revealed similar profiles in the mixing channel, where the highest temperature for both images was measured at the inlet of the mixing channel at the reaction interface. The temperature then slowly dissipated along the length of the channel and away from the reaction interface.

Two main differences were observed between the experimental and modelled results. The first difference was in the magnitude of temperature change within the mixing channel (*Fig. 3-11*), and the second difference was in the temperature change outside of the channels.

For the first difference in the magnitude of temperature change within in the mixing channel, temperature profiles for three rows centered on the reaction interface and at y-positions spaced 280 μm away in both directions were compared for both datasets (dashed lines in *Fig. 3-11*). Considering the experimental data, while the error bars are large, the temperature at the reaction interface has error bars that do not overlap with those in the profiles spaced 280 μm away in either direction, showing a distinguishable increase in temperature at the reaction interface. Directly comparing the same temperature range for experimental and simulated temperature profiles showed that the reaction interface had the highest temperatures. The profiles spaced 280 μm away in either direction had lower temperatures for both cases, but the discrepancy was significantly less in the simulated data. Regardless, the modelled data reflects the experimental data to a certain extent in this aspect.

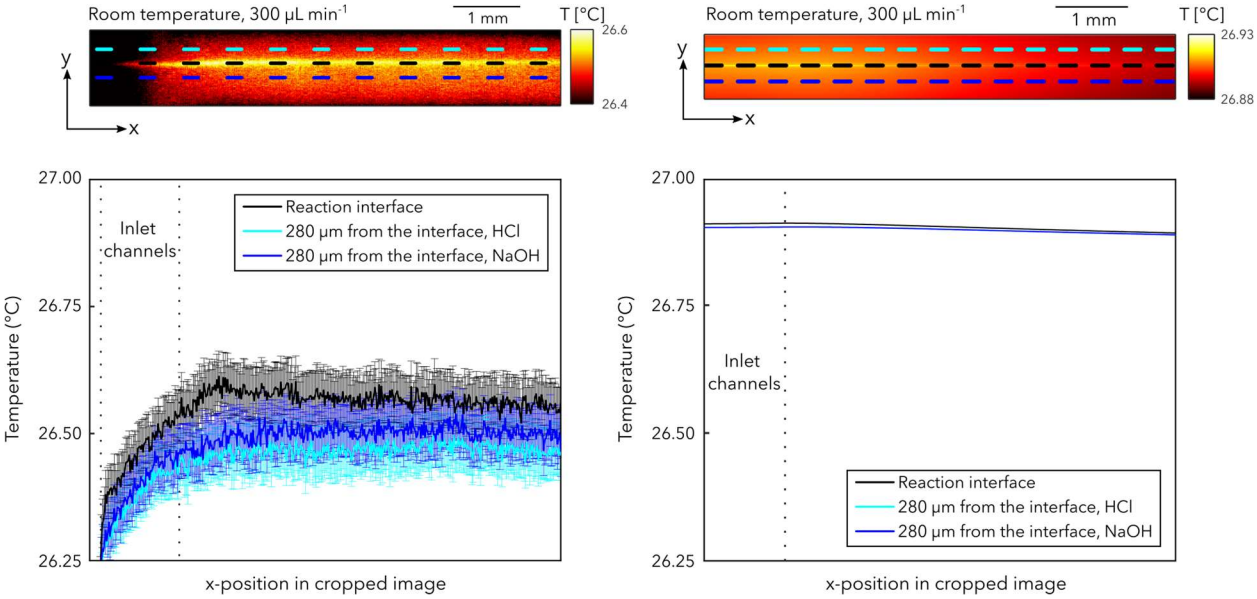

Fig. 3-11: The thermal profile at the reaction interface and for rows spaced 280 µm away in both directions for both the experimental and numerical data.

Regarding the second difference of temperature differences outside of the channels, the thermal conductivity of materials used to build the microfluidic chip were investigated. The thermal conductivity of PDMS and water are on the same order of magnitude (0.15 W m^{-1} K^{-1} and 0.61 W m^{-1} K^{-1}, respectively);[53,54] however, there is a stark contrast at the channel edges in the experimental thermal field that was not observed in the simulated thermal field. The thermal field from the simulated data was produced as an average of all slices, which does not necessarily reflect the behavior of proper emission for semi-transparent media. However, this discussion point is out of scope for the presented thesis and the study of thermo-transmittance in semi-transparent media is a popular research topic that has yet to be completely understood. Further research on this topic is under investigation by peers at I2M have researched.[55,56]

3.5 Chapter summary

In this chapter, a microfluidic reactor that is semi-transparent in IR light was developed and characterized via operando IR thermo-spectroscopic imaging. The imaging setup was developed to support two imaging configurations: FTIR spectroscopy and IR thermography. These imaging techniques were used to visualize heat and mass transport for two chemical reactions at three flow

rates. Additionally, a comprehensive 3D advection-diffusion model was developed to simulate chemical and physical behavior in the acid-base reactor. Experimental results were then cross-validated with the modelled results. The experimental setup used here was capable of capturing the heat generated from the exothermic acid-base reactions through contactless methods. While the heat produced from the exothermic reaction was less than 0.1 °C in the simulation, comparable experimental results were produced. However, the temperature measurements shown here approached the limits of detection for the combination of this specific experimental setup and chemical reaction. While further optimization of the techniques presented here may be used to pave the way towards achieving non-invasive methods for determining the enthalpy of reaction, two changes are recommended: (1) the fabrication of a microfluidic chip with materials optimized for heat transfer measurements, or (2) investigation using a chemical reaction that has a stronger enthalpy of reaction than those presented. These changes to the experiment would likely allow for more impactful measurements.

Nonetheless, the microfluidic chip and experimental setup presented in this chapter were developed as a proof of concept to refine fabrication techniques for the development and characterization of transport within a microfluidic polymer electrolyte membrane water electrolyzer through similar techniques. Since thermal measurements presented in this chapter faced limitations, the remainder of the work presented in this thesis will just be focused on mass transfer measurements in microfluidic water electrolyzers and heat transfer measurements will not be performed.

Part II. Implementing infrared spectroscopy with polymer electrolyte membrane water electrolysis

4 Background for polymer electrolyte membrane water electrolyzers

This chapter provides a background and review of previous works related to polymer electrolyte membrane (PEM) water electrolyzers that are relevant to the scope of the remaining chapters for this thesis. The key components that PEM water electrolyzer are comprised of and their impact on loss mechanisms are described. The working principles of the PEM in particular are detailed, as well as a review transport mechanisms and the tools used to characterize them within the PEM. Next, the characterization tools used to investigate these transport mechanisms are presented, with a focus on the PEM and the contribution of each characterization tool. Finally, infrared (IR) characterization techniques and their potential for electrochemical microfluidics are discussed.

4.1 Polymer electrolyte membranes

PEMs were first developed in the 1950s by General Electric, when the material was reported as a highly effective material for product separation while remaining permeable to ions.[16,17] Through the following decades, the benefits of this technology being increasingly attractive, as utilization of PEMs in water electrolysis was evaluated to be an efficient method of energy storage, through the conversion of electrical energy to chemical energy in the form of gaseous H_2.[57] Nafion, an ionomer developed by Dupont which uses a per/polyfluoroalkyl substance (PFAS) backbone, emerged as the most prevalent PEM which is still commonly used to this day.[58–61]

PEM electrolysis using Nafion or other PFAS-based membranes, benefits from higher current density operation than alternative electrolysis techniques. The higher achieved current densities reduces operational costs and consequently the overall cost of electrolysis. Almost all of the following benefits of PEM-based electrolysis can be attributed to the membrane's properties as a solid electrolyte:

1. Efficient product separation

The PEM is extremely efficient in separating anode and cathode compartments, as gaseous, liquid, and electrons are impermeable through it. This makes PEM electrolysis extremely effective for producing high purity H_2 gas, with purities greater than 99.9 % frequently reported in the

literature.[62–64] As a result, the dangers associated with mixing hydrogen and oxygen can be overlooked.

2. Fast response times

The use of a solid electrolyte allows the system to respond quickly to changes in power input, which are not delayed by inertial forces such as when using liquid electrolytes.[9]

3. High proton conductivity

PEMs are extremely advantageous due to their selective permeability to protons, as protons that are produced at the anode catalyst layer (CL) are able to flow through the PEM (with measured proton diffusion coefficients on the order of 1×10^{-5} cm^2 s^{-1}) to the cathode compartment, where they are converted to hydrogen gas.[65]

4. Low operating temperature

The low operating temperatures of PEM electrolysis relative to a competing type of electrolysis (solid oxide electrolysis), makes it more suitable for many practical applications such as transportation, as PEM-electrolysis is best at temperatures close to ambient and less than 100 °C.[11]

5. Low ohmic losses

Ohmic losses (and mass transport losses) typically limit the maximum achievable current densities for electrochemical systems. The solid property of the PEM allows ohmic losses to be minimized with thinner membranes.[66] The low ohmic losses in PEM electrolysis are part of what enables the high current density operation that the technology is known for.

6. Compact system design and high pressure operation

The use of a solid electrolyte enables compact system design that makes maintaining temperatures between ambient and 100 °C easier, while also enabling high pressure operation (30 MPa – 100 MPa).[12,67–71] Operating these devices at high pressures is advantageous for numerous reasons. First, high pressure operation means less energy is required for compressing and storing product hydrogen gas. Second, operating at high pressures may be accompanied by hazards associated with compressed oxygen, these can also be mitigated by using differential

pressure configurations where only the cathode side (hydrogen producing electrode) is under pressure. Third, mass transport losses are reduced by operating at high pressures, as the volume of gas at electrodes is reduced and gas removal from the CLs is improved. Finally, the PEM itself benefits as well as membrane expansion and shrinking relative to its hydration is decreased, resulting in improved CL integrity for catalyst coated membranes and less shear stress on the membrane in a built electrolyzer.

However, PEM configurations have several disadvantages as well, such as high material and production costs.[72] The corrosive reaction environment of acidic electrolysis can bring the reaction environment pH down to ~2 while operating at voltages greater than 2 V.[9] This limits the majority of electrolyzer materials to titanium, and catalysts to platinum group metals (e.g. Pt, Ir, and Ru) such that all materials that the electrolyzer is comprised of are corrosion resistant. Each of these materials considerably increases the capital cost of PEM electrolyzers, especially the catalysts, as iridium based catalysts are the most efficient in the market but is also one of the rarest elements in the earth's crust. Consequently, the market share of PEM electrolysis is intrinsically linked to the global iridium stocks.[73] Additionally, optimal operating conditions, such as high pressures, are also accompanied by higher rates of gaseous cross permeation. While thin membranes have reduced ohmic losses, they also become susceptible to punctures, especially when operating at higher pressures. Finally, improper disposal of Nafion and other PFAS materials can be extremely polluting as these materials are not expected to naturally degrade for millenia.[74–76] This has led to the development of many alternative PEMs to address the high capital costs and PEM fluorine content.[77–80] While researchers are optimistic about prospective cost reductions that these alternative PEMs may bring, Nafion and other PFAS membranes currently remain the 'gold standard' for PEM electrolysis due to their efficient mechanical stability, proton conductivity, and product separation.[72] As a result, the remainder of this thesis will be focused on PEM electrolyzers.

After decades of research, a complete understanding of transport phenomena within PEMs has yet to be achieved due to the complexity of the membrane's nanostructure. Transport mechanisms in PFAS materials during this time have been elucidated to an extent through a wide range of characterization tools. The flow of particles through PFAS membranes is comprised of several key mechanisms that occur at various length and time- scales, which will be explained in this section.

4.1.1 Water sorption in polymer electrolyte membranes

Prior to discussing water transport through the PFAS membranes, it is important to discuss their solvent sorption behaviors, which are directly tied to the electrochemical performance of PFAS membranes. Water absorption in PFAS membranes can be measured through a wide range of techniques, and is consequently reported through different metrics. One of the most common metrics for quantifying membrane water content is through 'λ' (and here as λ_{H_2O} for clarity), which is defined as the molar fraction of water molecules ($n(H_2O)$ [mol]) per sulfonic-acid group ($n(SO_3^-)$ [mol]) in the membrane.[65,81] λ_{H_2O} has values typically ranging from 0 to 30 depending on the membrane's material properties, its hydration, and operating conditions.[65] These values can be experimentally quantified using techniques like nuclear magnetic resonance (NMR) or they can also be determined macroscopically through the comparison of weight measurements in the dried and wetted states of the membrane:

$$\boldsymbol{\lambda_{H_2O} = \frac{n(H_2O)}{n(SO_3^-)} = \left(\frac{\Delta m_{H_2O}}{m_p}\right)\frac{EW}{M_{H_2O}}} \qquad \textit{Eq. 4-1}$$

where m and M denote the mass [g] and molar mass [g mol^{-1}], respectively, for water (H_2O) and the dry polymer (p). The $\left(\frac{\Delta m_{H_2O}}{m_p}\right)$ term specifically refers to the change in water content of the membrane by mass. Water content can also be cited in the literature as the water volume fraction (ϕ_w) and concentration (c_w). Each of these values are used to represent global measurements of membrane water content.

The water sorption (commonly referred to as water uptake) of PFAS membranes decreases with increasing equivalent weight (EW [$g_{polymer}$ $mol_{ionic\text{-}group}^{-1}$]) of the membrane,[82–85] heat-treatment temperature,[86,87] aging, contamination, and mechanical compression.[88–90] Each of these aspects can either be tied to chemical or mechanical changes in the membrane that affect its water sorption, and therefore its effectiveness to transport protons. The EW of a membrane in particular, is directly tied to the membrane's sulfonate acid site (SO_3^-) distribution and spacing. As the membrane absorbs water, protons (H^+) freely dissociate from SO_3^-sites, which are then mobilized by the absorbed water molecules. The EW of a membrane and its side-chain length (which is tied to a PFAS product and therefore the chemical formula of its backbone) have been observed to directly affect phase-separation and transport through the PEM. Specifically, increasing a membrane's EW

or backbone length has been shown to cause stronger aggregation, resulting in fewer and more sparse gas-liquid domains with higher pore sizes.[91,92] The backbone or side-chain length of a PEM is typically associated with a brand name of PEM (e.g. Nafion with long side chains from Dupont and Aquivion with short side chains from Solvay), and a PEM with a specific side-chain can then vary by EW, affecting the water distribution and its transport through the PEM.

The remainder of this section will highlight the driving mechanisms for water transport, a combination of water and proton transport (*Section 4.1.2*), and gaseous transport (*Section 4.1.3*) through PEMs. In these sections, particle transport through the membrane will be explained through the following four key transport mechanisms:[65]

1) Chemical diffusion, which is based on the concentration flux (ΔC) across the membrane and is dependent on the phase of the transported particle,
2) Hydraulic permeability, which is based on the pressure flux (Δp) across the membrane,
3) Thermo-osmosis, which is based on the temperature flux (ΔT) across the membrane,
4) And electro-osmosis, which is based on the proton flux ($\Delta \phi$) across the membrane.[93]

4.1.1.1 Chemical diffusion of water

Liquid water transport through a PFAS membrane occurs in absence of a concentration gradient. However, this is not representative of PEMs in working electrolyzers as both electrodes produce gaseous products which must be removed from the CL. Consequently, chemical diffusion must be considered, and can be separated into three major categories that are shown in *Fig. 4-1*: (1) interfacial diffusion – diffusion through the surface of the PEM, (2) bulk diffusion – diffusion through the PEM which occurs at a constant rate, and (3) pervaporation – diffusion from a PEM interface adjacent to liquid to the other side which is adjacent to vapor.[65,94,95] In pervaporation, the water that transports from the liquid side is vaporized while diffusing through the PFAS material, which emerges through the vapor compartment as a vapor as well. Pervaporation is irrelevant for the remainder of this thesis, and will consequently not be discussed further. Before discussing the

differences and impacts of interfacial and bulk diffusion, it is important to note that the diffusion of water through PEMs can be impacted by its pretreatment procedure.[86]

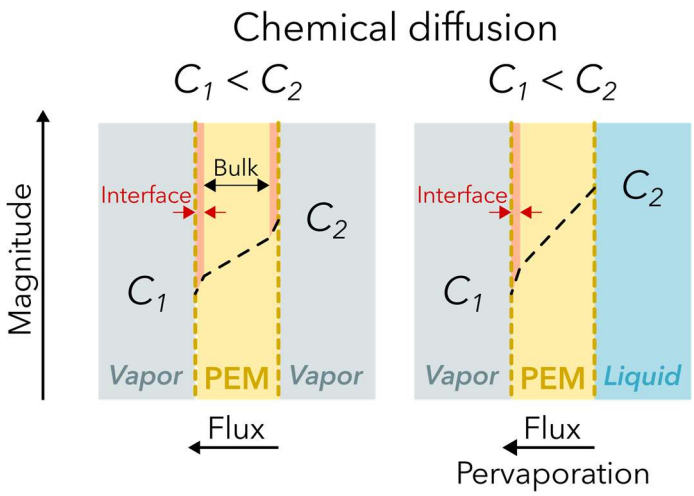

Fig. 4-1: Reproduced figure from Kusoglu et al. of mass diffusion through PEMs induced by concentration gradients.[65]

Interfacial diffusion can be distinguished from bulk diffusion through the Biot number, which is the ratio between the characteristic time scale of diffusion through the bulk of the PEM ($\tau_{diffusion}$) to the mass transport through the membrane's surface ($\tau_{interface}$).

$$\boldsymbol{Bi} = \frac{\boldsymbol{\tau_{diffusion}}}{\boldsymbol{\tau_{interface}}} = \frac{\boldsymbol{L^2/D}}{\boldsymbol{L/k_m}} \qquad \textit{Eq. 4-2}$$

where k_m is the mass-transport coefficient of the PEM [cm s^{-1}], L is the thickness of the membrane [cm], and D is the rate of diffusion through the PEM [cm^2 s^{-1}]. When the Biot number is small ($Bi \ll 1$ or $\tau_{interface} \gg \tau_{diffusion}$), water transport is limited by the interfacial resistance of the membrane ($k_m \to 0$). When the Biot number is large ($Bi \gg 1$ or $\tau_{diffusion} \gg \tau_{interface}$), the interfacial resistance becomes negligible ($k_m \gg 1$) and water transport is limited by the rate of diffusion through the bulk of the membrane. The Biot number is heavily influenced by the thickness of the membrane, so membranes with lower thicknesses (e.g. 50 µm or less) are more likely to be limited by interfacial resistance with small Biot numbers, and vice versa. Kusoglu and

Weber report that the critical value that determines which process dominates and which process is negligible is around a value of $Bi = 10$.[65]

Interfacial diffusion and bulk diffusion are heavily dependent on the boundary conditions immediately surrounding the system, as the interfacial resistance and bulk resistance are strongly affected by the water content of the PEM. Specifically, if the PEM is between liquid (or saturated vapor in the case of He et al.) interfaces on each side, the interfacial resistance and bulk resistance would both decrease. He et al. showed that if the PEM's surface is surrounded by saturated vapor on one side and liquid on the other, the interfacial resistance decreases significantly and bulk diffusion was dominant.[96] If any of the PEM surfaces were to be surrounded by low humidity vapor instead, the interfacial resistance would increase and interfacial diffusion would dominate bulk diffusion.[97,98]

4.1.1.2 Hydraulic permeability

Water transport through pressure differentials when the PEM is surrounded by liquid on each side is generally assumed to be relative to the hydraulic permeability of the PEM and the pressure differential across it. This assumption is founded on the basis that water transport driven by a liquid pressure gradient through the PEM follows an expression similar to Darcy's Law, shown below.

$$\boldsymbol{q} = -\frac{\boldsymbol{k}}{\boldsymbol{\mu L}}\boldsymbol{\nabla p} \qquad \textit{Eq. 4-3}$$

where q is the instantaneous flow rate through the medium [cm s^{-1}], k is the permeability of the medium [cm^2], μ is the dynamic viscosity of the fluid [Pa s], L is the thickness of the medium [cm], and ∇p is the pressure drop through the medium [Pa]. In the same case as chemical diffusion through the membrane, the hydraulic permeability of the membrane is also dependent on the pretreatment of the membrane.[99] However, experiments are rarely performed to measure the hydraulic permeability of the membrane as it does not represent the PEM during electrochemical operation where gas is consistently being produced at the CLs. Moreover, water phase effects for PEMs are attributed to the thermal treatment of the materials and water transport between liquid and vapor phases.[100–102] For the context of this thesis, pressure differentials between anode and

cathode compartments are not expected to significantly affect results, and will therefore be neglected.

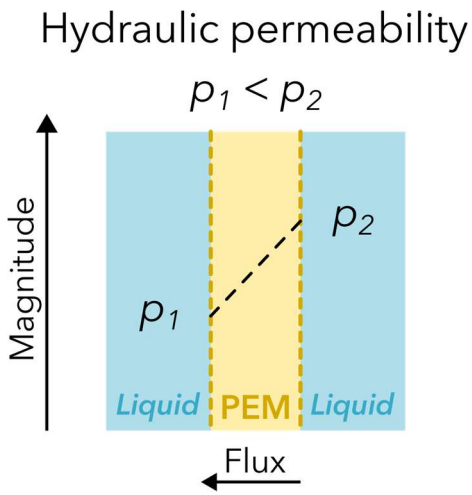

Fig. 4-2: Reproduced figure from Kusoglu et al. showing the effect of hydraulic permeability through the PEM induced through a pressure differential between liquid compartments.[65]

4.1.2 Phenomena involving both water and proton transport

Proton transport through PEMs is inherently tied to water transport, as the membrane water content changes the way that protons transport through the sulfonic acid groups within the PEM. Proton conduction through the membrane is one of the most well researched subjects in the decades of PEM research, with studies investigating the effects of hydration, membrane thickness, mechanical deformation, and much more.[103–105] The most relevant for the context of this thesis are those that investigate the effects of membrane hydration, for which the mechanisms driving both water and proton transport through PEMs will be further discussed in the following subsections.

4.1.2.1 Electro-osmosis

Electro-osmosis can be quantified through the electro-osmotic drag coefficient, which is the number of solvent molecules carried per ion.[93] For water electrolysis, this would refer to the drag

of water molecules by protons through the PEM from the anode to the cathode. The H^+ protons transport through the free volumes of a PEM's polymeric matrix, which electro-osmotically drags water molecules in the form of hydrated protons (H_3O^+) across the PEM.[106] Electro-osmosis occurs due to the nature of proton chemistry, where protons are unable to exist as a free species in a solution as they lack electron clouds.[107]

Consequently, proton transport in PEMs (*Fig. 4-3*) has been summarized through two mechanisms – the vehicle mechanism and the Grotthuss hopping mechanism. The vehicular mechanism occurs as a hydrated proton $(H_{2n+1}O_n)^+$ transports through the PEM similar to chemical diffusion (*Fig. 4-3b*). The hopping mechanism is a method of structural diffusion that occurs as a proton 'hops' through a chain of hydrogen-bonded water molecules (*Fig. 4-3c*). In a working electrolyzer, these two processes compete depending on the hydration of the PEM. Specifically, when the PEM has a relatively low hydration, the vehicular mechanism dominates protons transport. Conversely, when the PEM has a relatively high hydration, the Grotthuss hopping mechanism dominates protons transport across the PEM through a series of bond-breaking and forming, such that the proton that emerges out of the PEM is not the same as the one that went in. Grotthuss hopping is reported to be highly dependent on the PEM being sufficiently hydrated, as proton transport through this mechanism requires frequent reorientation of the water molecules.[108,109] These mechanisms are what enable the highly attractive proton conductivity of hydrated PFAS materials.

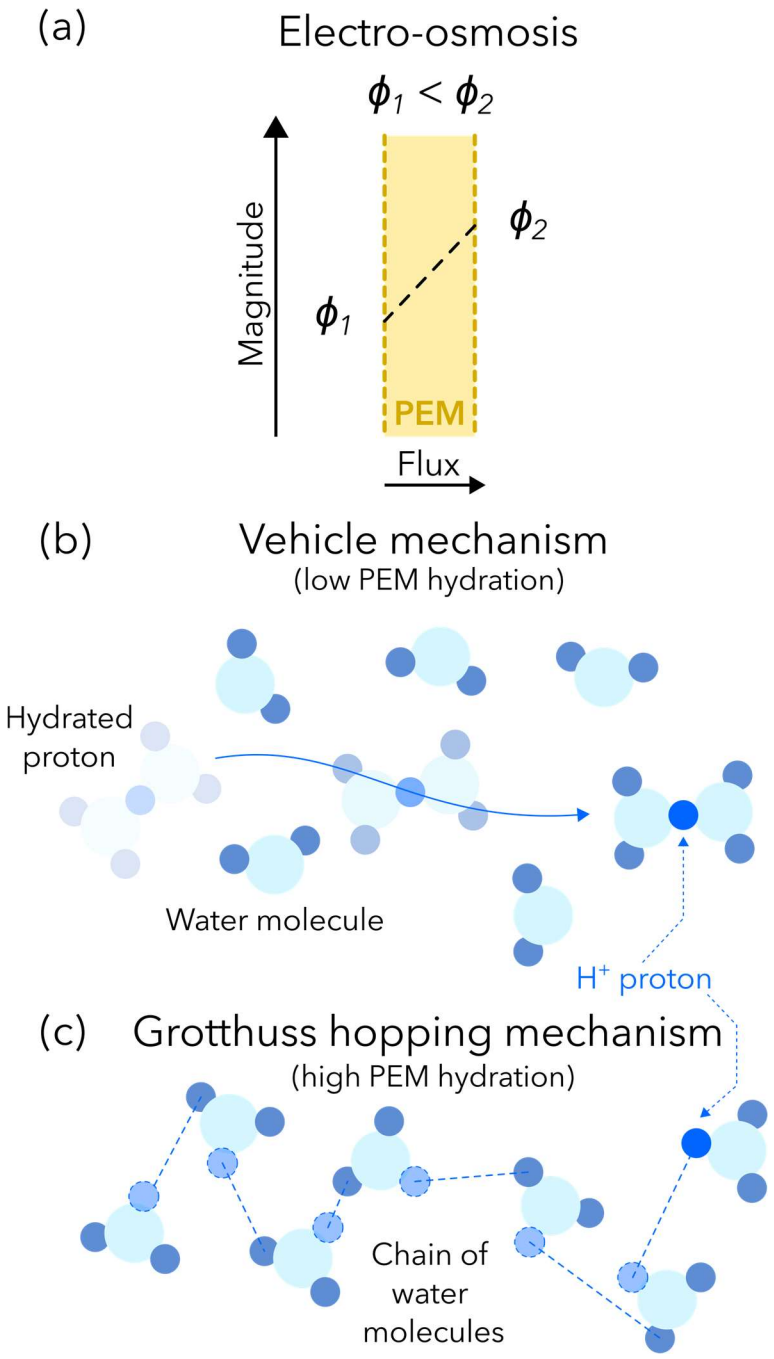

Fig. 4-3: Electro-osmosis through polymeric materials. (a) A reproduced schematic from Kusoglu et al. showing the effect of electro-osmosis induced through a proton gradient ($\boldsymbol{\Delta\phi}$) through the PEM.[65] *The transport mechanisms occur through the (b) vehicle mechanism, where a hydrated molecule carries a proton $(\boldsymbol{H_{2n+1}O_n})^+$ across the PEM, and (c) the Grotthuss hopping mechanism, where protons 'hop' down a chain of hydrogen bonded water molecules through repeated bond-breaking and forming.*

4.1.2.2 Thermo-osmosis

Thermo-osmosis occurs when a water flux is produced due to a temperature gradient (*Fig. 4-4*). This mechanism is driven by the entropy of water, which is challenging to define for individual ions. Villaluenga et al. showed that imposing a temperature gradient led to a proportional water flux that consistently flowed from the cold to hot side.[103] Kim and Mench confirmed this behavior for Nafion, Gore-Select, and Flemion membranes and found that the thermo-osmotic diffusivity exhibited an Arrhenius-type temperature dependency.[110] However, thermal-osmosis still remains one of the less explored transport phenomena, which could be elucidated through its interrelations with membrane swelling, proton differentials, and concentration differentials across it.

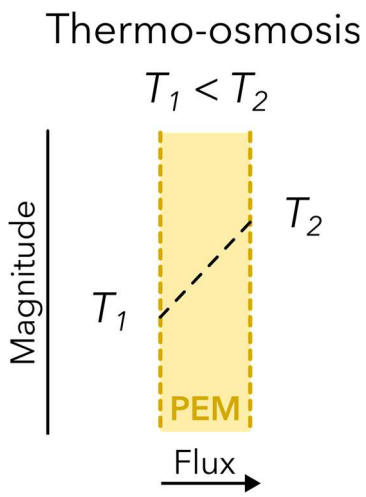

Fig. 4-4: Reproduced figure from Kusoglu et al. showing the effect of thermal osmosis through the PEM induced by a temperature gradient.[65]

4.1.3 Gas transport

Gas transport through PEMs is similar to gaseous diffusion in solutions. Gas diffusivity is relative to the size of the gas particles, the gas concentration, the free volume in the PEM, the PEM's structure and morphology, and more. As a result, the permeability of a gas through polymers is dependent on many factors that directly affect the PEM, such as its water content, temperature,

and condition.[111–114] Since gas permeability is commonly associated with the free volume in polymers, the same assumption is often extended toward PFAS materials. However, this assumption is not applicable to PEMs integrated in electrochemical devices, as it was found that gas permeability through PEMs is only valid when the PEM is dry.[115,116] Similarly, any factors other than hydration that influence the PEM structure or morphology would also affect the gas permeability through it. For example, the side chains that build the chemical structure of the PEM directly affect the EW and crystallinity of the PEM. These properties then affect the membrane's pore sizes and consequently its gas permeability.

4.2 Characterization techniques

In the previous section, the relevant transport mechanisms in PEMs were described to provide a background of PFAS materials, and the effect of these mechanisms on the PEM in electrolyzers was detailed. This section will be dedicated to reviewing prior research efforts to characterize the PEM through the techniques used to understand transport phenomena within PFAS materials, and their effects on electrochemical performance when integrated.

4.2.1 Quantifying electrochemical impedance

Electrochemical characterization techniques through electrochemical impedance spectroscopy (EIS) have become integral to the field, as these techniques can be used to discriminate losses in electrolyzers. Alternating current (AC) impedance analysis is one of the most commonly used techniques, as changes to operating conditions can be connected to mechanisms that affect the system's polarization.[117] Each loss mechanism in electrochemical devices (ohmic, activation, and mass transport) can be associated to different relaxation times, and therefore can be discerned when using time-resolved EIS techniques.[118–120] For example, the ohmic resistance can reliably be discerned through EIS as the high frequency contribution of an electrolyzer, while the low frequency measurements provide information on the activation and mass transport losses. Given an appropriate range of tested current densities or potentials, activation losses can be discriminated from mass transport losses through Tafel extrapolation, allowing the quantification of each source of performance loss in an electrolyzer.[121,122] However, the response of EIS techniques is highly

dependent on the design of the electrolyzer device, the materials used, the catalyst, etc. Consequently, EIS results must be evaluated for specific systems with reference cases to associate the effects of these differences to the imposed experimental variables.

The impedance of an electrolyzer can be further analyzed using equivalent electrical circuits (EECs), which can be used to model each component of the device. Consequently, the response of the system can be modelled as a function of its operating parameters, such as potential, current density, temperature, humidity, etc. The residuals of the EEC can also be further analyzed to provide realistic interpretations of the physical phenomena in the electrolyzer, such as reaction mechanisms.[13,123,124] For example, Niya and Hoorfar show how EEC models can be coupled with EIS techniques to isolate ohmic losses attributed to the membrane, as well as how to extract the membrane diffusion coefficient in PEM fuel cells.[125] When coupled with additional techniques, even more information can be extracted, such as the work by Chevalier et al., which combines EECs, EIS data, and X-ray images to investigate the liquid water distributions in custom electro-spun gas diffusion layers for PEM fuel cells.[126] These studies not only show the benefits of electrochemical diagnostic techniques, but that these techniques are increasingly effective for elucidating mechanisms in electrochemical devices when used together.

4.2.2 Characterizing transport within polymer electrolyte membranes

The measurement of ion and mass transport across PEMs has been performed via various characterization tools over the course of the past couple decades of research. This subsection will be dedicated to describing the characterization techniques used to measure proton transport and water transport through PEMs for electrochemical research.

Nuclear magnetic resonance, commonly abbreviated as NMR, was one of the first tools used to measure water sorption and diffusion in PEMs, as it can be used to clarify the distribution of the chemical compositional in polymers. NMR is particularly useful for measuring the membrane water content (λ_{H_2O}, *Eq. 4-1*), which is the ratio of water molecules per sulfonic acid site in the polymer matrix of a PEM. NMR is typically used in this context to measure tracer (or self) diffusion, which is defined as the spontaneous mixing of molecules in absence of a concentration gradient. These measurements are achieved through the excitation of a molecule, and then by

tracking its interactions and relaxation times. Specifically, NMR measures the radiofrequency electromagnetic radiations that are produced from the resonance between a strong magnetic field generated by the apparatus, and the nuclei of molecules for samples of interest. For example, Ise et al. utilized electrophoretic NMR to measure the electro-osmotic drag coefficient in two PEMs of different compositions, sulfonated polyetheretherketoneketone (PEEKK) and Nafion; and found that while the sulfonated PEEKK had lower water content than Nafion, it had higher proton conductivities and drag coefficients.[127] Lee et al. showed that the measured relaxation times of deuterated water from NMR increase with increasing membrane hydration (*Fig. 4-5*).[83] NMR techniques utilizing pulsed field gradient spin-echo (PGSE) have also been implemented to provide more information of the molecules within the sample. These studies have been able to quantify water diffusion for a wide range of conditions, and when coupled with electrochemical characterization techniques, can also simultaneously quantify proton transport.[128–130] Magnetic resonance imaging (MRI) is a similar technique that differs from NMR as information is generated through radiation intensity instead of radiation frequency. MRI has also been used to quantify water diffusion through PFAS materials, such as through the work of Suzuki et al., who used a combination of MRI and dew point measurements to quantify the in situ flux of water through the PEM and a CCM. They showed that the interfacial transport between membranes leads to differences in water properties due to the catalyst coating of the CCM.[131]

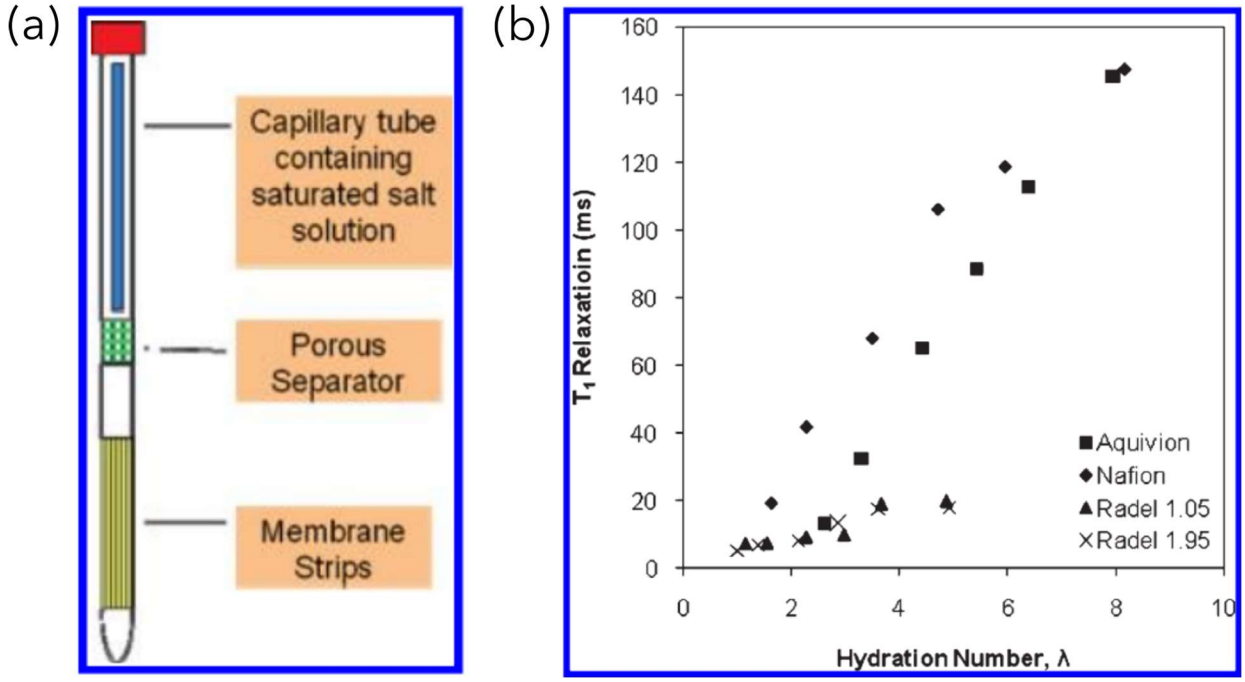

Fig. 4-5: Figures from the work presented by Lee et al. presenting the (a) experimental setup for the in situ NMR humidification, and (b) The deuterium (^2H) relaxation times (T_1) at 46.07 MHz for different proton-conducting membranes as a function of hydration number.[83]

Dynamic vapor sorption (DVS) is a gravimetric technique for quantifying the sorption of a solvent by a sample, which is frequently used as an ex situ and in situ method for measuring the water sorption of a PEM. DVS is performed by varying the vapor concentration around the sample, and measuring the corresponding changes in its mass. This technique is particularly useful for measuring water transport in the form of vapor at higher temperatures in PEM electrolyzers or fuel cells. DVS measurements reported in the literature have shown that an increasing water vapor uptake in PEMs was accompanied by an increasing humidity and a decreasing water diffusivity.[132,133] For example, Mangiagli et al. found that slower water sorption with high reactant relative humidities (RHs) was due to the smaller enthalpy of solvation for hydrated membranes, which reduced the rate of additional water uptake.[132] Results obtained through DVS have opposed those reported by NMR experiments, which have increasing diffusivity with increasing reactant RHs.

Atomic force microscopy (AFM) is a type of scanning force microscopy that utilizes a small probe that contacts the surface of a material and scans across it, and is capable of achieving high resolutions that can be as small as a fraction of a nanometer. AFM has been used to characterize

the surface of membranes and electrodes. For example, O'Hayre et al. demonstrated the use of AFM for characterizing various surfaces, such as electrodes and Nafion.[134] When AFM is combined with current sensing, the technique is modified and can be referred to as conductive AFM (CAFM). CAFM is more advantageous than AFM, as it can be used to measure the conductivity across the membrane. This was achieved in the work presented by Bussian et al., who performed CAFM via an AFM tip coated with platinum to act as electrodes for a PEM fuel cell (*Fig. 4-6*).[135] During their CAFM measurements, they found that around 60 % of the aqueous domains at the surface of a Nafion PEM were inactive.

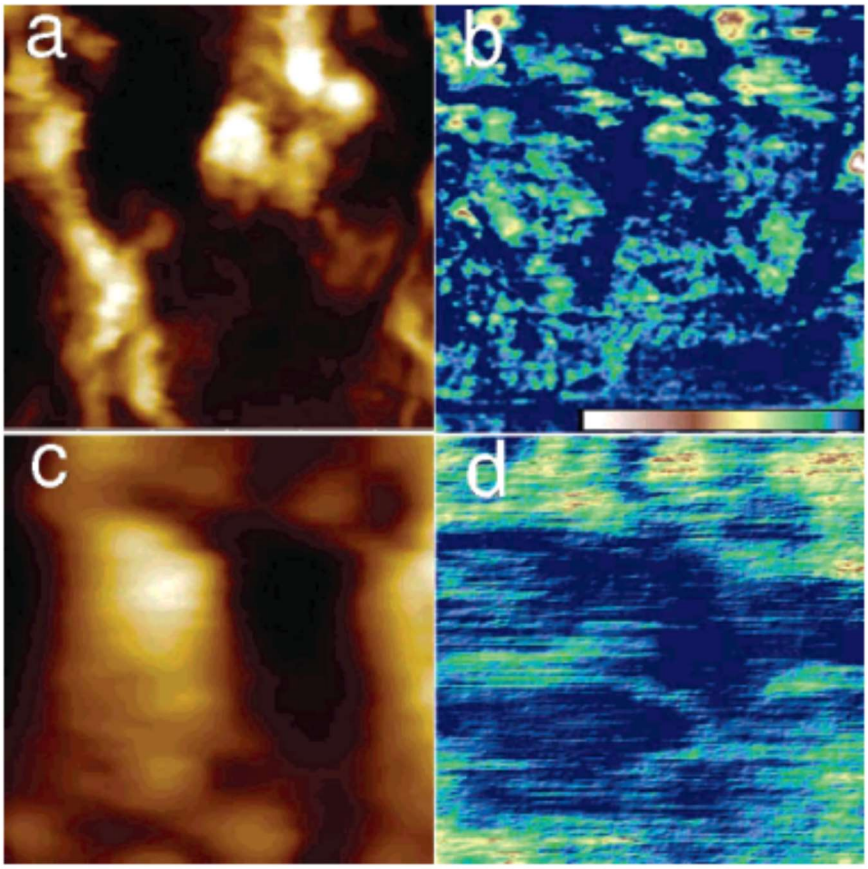

Fig. 4-6: Figure from the work presented by Bussian et al. showing AFM images of an active hydrogen fuel cell: (a) height (z-scale 75 nm) and (b) current (z-scale 20 pA, color bar with blue at 0 and maximum as white) regions of a 1 µm × 1 µm region; (c) height (z-scale 10 nm); (d) current (z-scale 5 pA) images of a 500 nm × 500 nm region taken from the center of the scan in (a).[135]

Confocal Raman microscopy is a spectroscopy technique based on the distribution of inelastically scattered light that has also been used to characterize the water content in PEMs. Deabate et al. describes the potential of Raman microspectroscopy for in situ and operando characterization of PEM water content, which their group implemented to show deviations from ex-situ measurement techniques, and for a range of working conditions and multiple PEMs.[136–138] Tabuchi et al. have also utilized confocal Raman spectroscopy to quantify water diffusion through PEMs, and compared those results to NMR results by Zawodzinski et al.[139,140] Additionally, Hara et al. showed that back-diffusion of water produced in a PEM fuel cell led to clearly detectable membrane humidification, and increased water transport through the membrane with increasing temperature.[141]

In addition to the previously described techniques, X-ray and neutron based imaging techniques have been implemented to characterize operando PEM water content in working fuel cells and electrolyzers. X-ray and neutron techniques are complementary techniques, as the beams produced by their respective sources are attenuated by the electron clouds of the incident materials for X-rays, and neutrons in the materials for neutron imaging.[142,143] As a result, this makes X-ray imaging effective for characterizing elements with low atomic numbers, such as carbon materials used in gaseous diffusion layers for fuel cells, as those materials are more transparent due to their relatively smaller electron clouds. In contrast, high atomic numbered elements are more transparent with neutron imaging, making this technique effective for visualizing changes in water transport through the titanium components commonly used in water electrolysis, as water strongly attenuates neutron beams while the titanium has higher transparency.

In 2004, Mauritz and Moore published an extensive review of the chemical structure of Nafion, citing morphological studies through the use of small-angle and wide-angle X-ray scattering (SAXS and WAXS, respectively).[59] Since then, significant progress has been made for not just the understanding of PFAS material structure, but also with X-ray techniques that investigate the PEMs in operating fuel cells and electrolyzers. Synchrotron based X-ray techniques have been used extensively to investigate these materials in situ and in operando with high spatial and temporal resolutions.[126,144] For example, Hwang et al. measured the water distribution in Nafion with spatial and temporal resolutions of 1 μm and 10 min, respectively, to show a nonlinear water profile through the PEM that had a continuous transition from dynamic to steady-state transport coefficients.[98] Wong et al. showed that the polytetrafluoroethylene (PTFE) content in standalone

microporous layers for operating PEM fuel cells created a tradeoff between membrane hydration and mass transport losses, where higher PTFE content leads to greater liquid accumulation adjacent to the CL, leading to improved hydration and proton conductivity while increasing the mass transport resistance (*Fig. 4-7*).[145] Another researcher from the same group coupled operando synchrotron x-ray radiography with EIS to quantify the effect of high current densities on membrane thickness with varied inlet gas RH in a PEM fuel cell.[146]

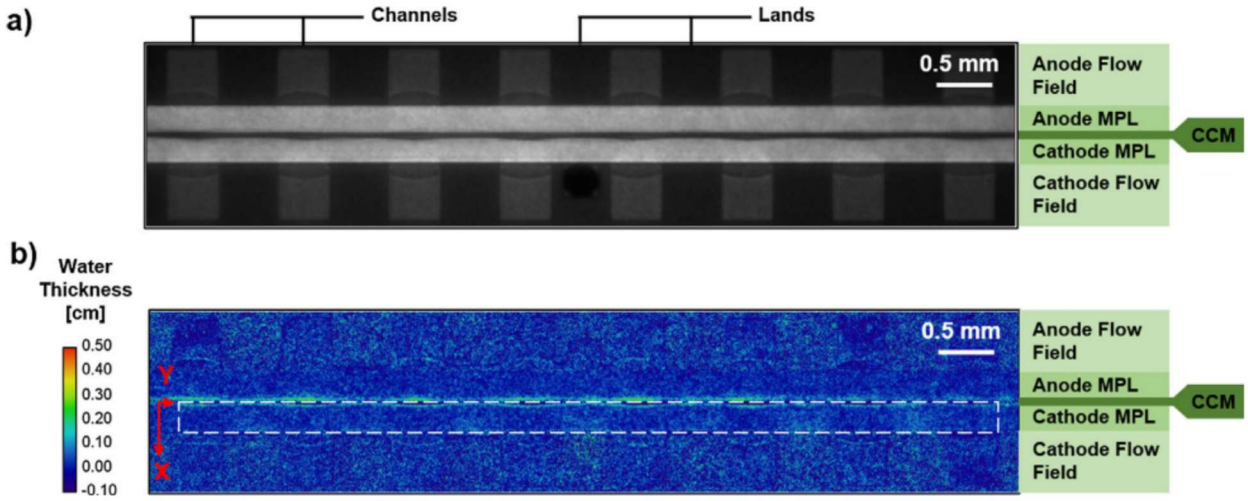

Fig. 4-7: Figure from the work presented by Wong et al. showing sample synchrotron radiographs, (a) raw image and (b) processed water thickness image. Microstructural layers and major structural components in the through-plane direction are highlighted beside both images. The direction of through-plane water profiles are indicated by the x-axis. The dashed box in the processed image indicates the cathode gas diffusion layer (GDL) where liquid water was quantified for this study. The color bar represents the thickness of water in the z-direction of the image.[145]

Neutron based techniques struggle with resolving the PEM water content in operating electrochemical devices due to the damage that neutron beams pose to PEMs, but have nonetheless been used to observe operando changes in membrane thickness. For example, Hickner et al. utilized neutron imaging used to evaluate the water content of the membrane electrode assembly (MEA) in a PEMFC for a range of current densities and temperatures.[147] Neutron radiography was also used to investigate PEM wetting in an operating fuel cell, where Quan et al. showed that the

wetting process for components in the cell was 1.4 times longer than the drying process.[148] In 2011, Morin et al. utilized small angle neutron scattering to measure the water content in Nafion 117 and showed that gravity improved water retention for the cell, which in turn led to improved membrane hydration.[149]

When coupled with operando imaging techniques, the field of view for the imaging technique is limited to the architecture of the device, as images are strongly affected by the orientation of the cell. Determining the PEM water content between anode and cathode compartments in these devices requires isolating the PEM for image acquisition. This can only be done when electrolyzer is visualized on its side such that the stack of the electrolyzer is visible and each component can be distinguished. However, this approach is infeasible for quantifying PEM hydration, as the PEM water content can only be determined as an average through the plane of the captured images. This challenge has been partially addressed through the refinement of technology that has led to the rise of tomographic techniques, which can be used to quantify gas and liquid phases in these devices through each of the materials at high spatial resolutions.[150,151] However, high spatial resolution computed tomography (CT) suffers from long acquisition time scales, typically longer than 1 hour, that are necessary for the lengthy image acquisition and image reconstruction routine. This limitation can obscure mass transport through these devices with flowing reactants, often leading to image acquisition with halted reactant and product flow. Nevertheless, these techniques are invaluable to the field for elucidating gas and liquid distributions in operating devices, with recent publications even combining both X-ray and neutron CT for resolving the distributions of gaseous and liquid phases through up to six PEM fuel cell components.[152,153]

4.2.3 Research gaps

The previous decades of research have elucidated many characteristics in PEMs, but only in the last decade have studies been able to move beyond ex situ and in-situ measurements. A complete understanding of ion and water transport in PEMs remains elusive due to the complex nanostructure of the membrane that reacts in a dynamic manner when these devices are in operation. By utilizing techniques that are novel to the field such as IR, the effects of ion and water transport through the PEM can be elucidated; and parameters that affect these phenomena can be identified. Advances that push our understanding of PEM structure and transport mechanisms that

occur within them are necessary for establishing a basis for experimental models, which would significantly contribute to improving the efficiency of PEM electrolysis.

4.3 Infrared characterization applied onto electrochemistry

Various infrared (IR) based techniques can be used to gain an understanding of the molecular chemistry of the studied sample. For IR spectroscopy, an IR beam is directed through a sample, which then attenuates the beam for IR frequencies that are the same as the vibrational frequency of molecular bonds – or groups of bonds – in the sample. IR spectroscopy can be performed with monochromatic beams through the use of a monochromator or with a polychromatic source through a Fourier transform infrared (FTIR) spectrometer (working principles detailed in *Section 2.2.1*). IR characterization techniques are non-intrusive, allowing the characterization of samples without alteration in any way or the need for any pre-treatment. These techniques also benefit from high spatial and temporal resolutions depending on the number of wavelengths or wavenumbers scanned. However, while IR techniques can be used to provide information on the molecular chemistry of samples, they are not able to provide full structural information of the sample as through other techniques like NMR. Therefore IR techniques are often coupled with others to study samples. Moreover, IR techniques are sensitive to impurities in the sample, which can cause unwanted IR spectral peaks or otherwise obscure acquired data. Water in particular absorbs infrared light very strongly, consequently leading to short effective path lengths at fractions of a millimeter through samples containing water.

4.3.1 Attenuated total reflection

Attenuated total reflection (ATR, *Fig. 4-8*) is a technique that is often coupled with IR spectroscopy to examine solid or liquid state samples. ATR is performed by directing an IR beam through an ATR crystal that is made of a material with a high refractance index at certain angles. The reflectance of the IR beam through the ATR crystal creates an evanescent wave that extends a couple microns beyond the surface of the crystal. With the sample placed on the ATR crystal, the sample absorbs energy protruding from the ATR crystal from the evanescent wave produced

by the IR beam, which then passes through the rest of the ATR crystal before being captured by the detector. The resulting signal from the detector can then be used to generate an IR spectrum.

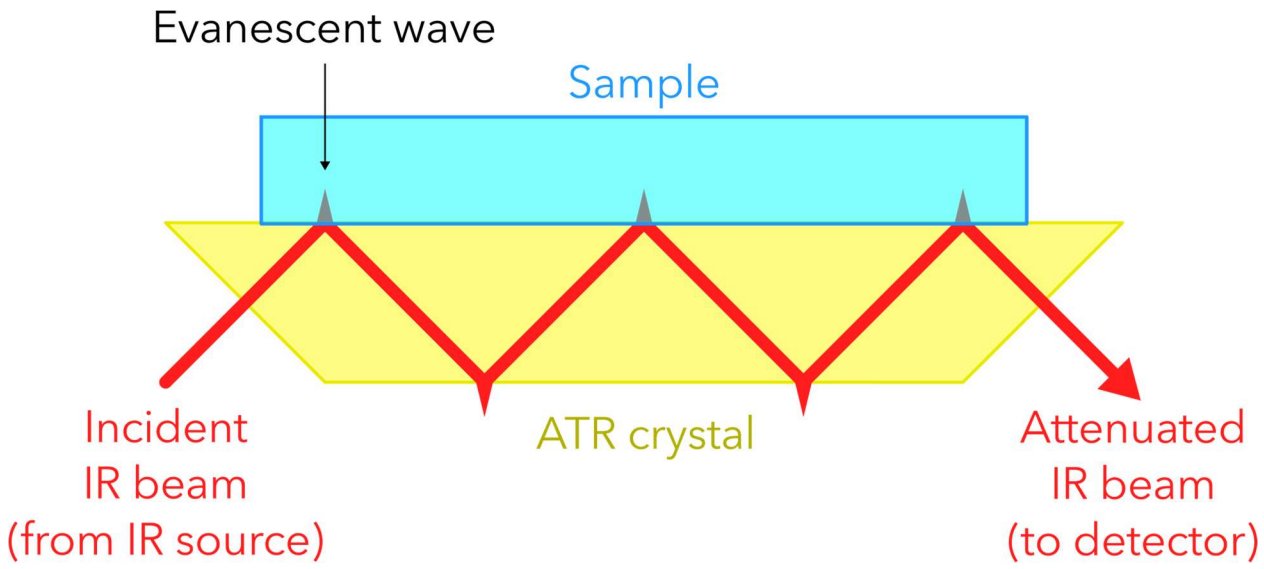

Fig. 4-8: Schematic of the working principle of ATR. The incident IR beam from the IR source passes through the ATR crystal, producing evanescent waves that extend a couple of microns past the surface of the ATR crystal, which are then absorbed by the sample. The attenuated IR beam then traverses through the rest of the sample and ATR crystal and is captured by the IR detector, which can be used to reproduce the IR spectrum of the sample.

4.3.2 Transmission infrared spectroscopy

Transmission IR spectroscopy produces IR spectra through the transmitted IR light that is measured through a sample, and benefits from higher quality IR spectra when compared to ATR due to quantifying IR light attenuation transmitted through the sample, not just from light reflected off its surface. While benefitting from higher quality IR spectra, transmission IR spectroscopy is more sensitive to light aberrations, such as those from bubbles in liquid analyses. When transmission based IR spectroscopy is applied to characterizing PFAS materials, it is commonly performed ex-situ and has been reported in the literature under varied conditions applied to the PEM (e.g. compression, membrane hydration as shown in *Fig.* ***4-9***, temperatures, etc.).[154–159]

While many comparable works have also been performed using ATR,[87,160–163] transmission based techniques are the only ones capable of performing imaging. Moreover, they also benefit from larger characteristic lengths, which are large enough to quantify hydration through the thickness of the PEM.

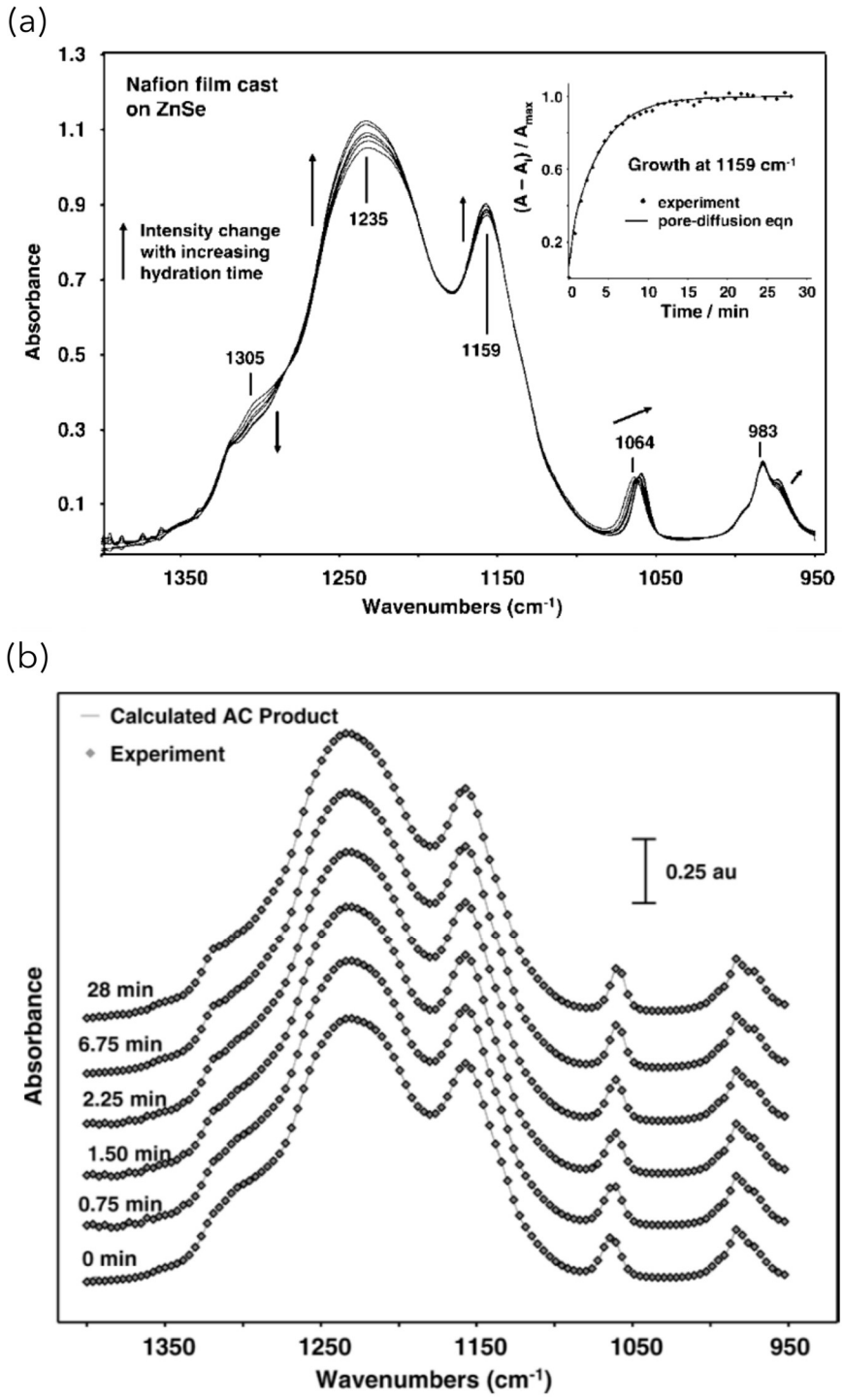

Fig. 4-9: Figure from the work presented by Korzeneewski et al.[154] *showing the (a) experimental infrared spectra of a thin Nafion film cast onto a ZnSe optical window recorded during hydration in 100 % relative humidity air starting from a dry state. Spectra were recorded at different exposure times to humid air. The arrows indicate the direction of band intensity. (b) Data from the experimental spectra with a point plotted every 4 cm^{-1}.*

The previously detailed IR techniques have been used to characterize water transport in PFAS materials through predominately ex-situ methods, as IR characterization techniques use long-wavelength light that has weak penetration and therefore short effective path lengths, especially through samples containing water. Zelsmann et al. used quantitative IR spectroscopy to measure the diffusion coefficients of water in PEMs that agreed with isolated permeation-sorption measurements.[164] Far-IR wavelengths have also been implemented to study the vibrational trends of Nafion.[159] Additional studies performed by Blanchard and Nuzzo as well as Shimoaka et al. investigated the structure of Nafion membranes when hydrated through IR spectroscopy for a range of conditions.[157,158] In addition to IR spectroscopy, FTIR spectroscopy was used by Lowry and Mauritz to monitor hydration at the sulfuric acid sites in Nafion, where IR absorption peaks were observed to shift to higher frequencies and broaden as the membrane water content decreased.[165] ATR coupled FTIR was implemented to quantify water diffusion by Hallinan,[161,162] and the spectral peak positions of SO_3^- sites in the PEM for various thicknesses of spin-cast Nafion by Zimudzi and Hickner.[163] The extent of research shown using both transmitted and reflected IR characterization techniques shows us the versatility of IR characterization. These IR techniques can be used to quantify structural changes to the SO_3^- backbones of PEMs, while also providing information relative to the hydration and identifying if a dependence or correlation exists between these parameters.

4.3.3 Research gaps

While IR techniques have been successfully used to characterize water transport through PFAS materials, this has only been achieved through ex-situ measurements. These works utilize IR techniques to gain a fundamental understanding of the effect of water on the chemistry of sulfonic acid sites within PEMs under various conditions. However, the IR techniques detailed in the previous section and *Section 2.2* have much more potential that have yet to be utilized. For example, PEM backbone and side chain analyses, such as in the work by Zimudzi and Hickner, can be simultaneously studied with regard to the PEMs hydration using in operando techniques.[163] When combining microfluidics with operando transmission IR imaging, far more effects of PEM hydration on structural information can be gained. While IR techniques have disadvantages associated with the physics of the techniques, such as the short effective optical path, many of

these disadvantages can be overcome through tailored cell design. Specifically, short effective path lengths can be overcome through the use of microfluidic chips, as shown in the previous chapter, where micro-scale dimensions become advantageous. Additionally, if IR imaging of PEM electrolyzers can be achieved in tandem with the other IR-based techniques, such as thermography, then poorly understood phenomena such as mass transport and thermo-osmosis could be simultaneously elucidated. Consequently, a greater understanding of PFAS materials would be achieved, which would also improve modeling efforts and ideally enable increased efficiency for electrochemical PEM devices.

4.4 Chapter summary

In this chapter, the background and review of polymer electrolyte membranes (PEMs) for use in electrochemical water splitting was introduced. The history, advantages, and disadvantages of PEMs was discussed for the context of water electrolysis, as well as the key mechanisms that govern ion and mass transport through PEMs. Next, common characterization techniques used to analyze the PEM were discussed and a literature review for each presented technique was provided. Additionally, the research gaps associated with analysis techniques for PEM research were detailed. Then, IR techniques that were not discussed in previous chapters were introduced in addition to a brief literature review regarding all relevant infrared techniques. Finally, the research gaps associated with utilizing IR techniques for investigating ion and mass transport through PEMs were discussed. IR techniques have immense potential for elucidating poorly understood phenomena within PEMs, such as the chemical diffusion of water and both electro- and thermo-osmotic drag through the PEM. In the following chapters, a combination of microfluidics and these IR techniques will be implemented to realize a novel operando IR imaging setup for characterizing these transport phenomena within the PEM of an operating electrolyzer.

5 Probing membrane hydration in microfluidic polymer electrolyte membrane electrolyzers via operando synchrotron Fourier transform infrared spectroscopy

5.1 Introduction

In this chapter, the first microfluidic polymer electrolyte membrane (PEM) electrolyzer that is semi-transparent in infrared (IR) light was developed as a platform for characterizing the PEM hydration during operation. The electrochemical performance of the chip was compared to its PEM hydration, which was measured via synchrotron Fourier transform infrared (FTIR) spectroscopy. The PEM water content was directly probed in the operating electrolyzer by measuring the transmitted light intensity at wavelengths around 10 μm. By supplying the electrolyzer with reactant starving flow rates, mass transport driven cell failure was provoked, which coincided with membrane dehydration. Furthermore, higher operating temperatures were observed to improve the stability in membrane hydration through increased membrane water uptake. The work presented in this thesis chapter acted as a first step towards evaluating the PEM hydration in an operating PEM electrolyzer using IR techniques. This work was published in *Lab on a Chip*.

5.2 Methods

5.2.1 Fabrication of the microfluidic electrolyzer

A custom microfluidic water-splitting electrolyzer (*Fig. 5-1*) was developed as an IR spectroscopy platform for characterizing PEM water-transport during electrochemical operation. The microfluidic electrolyzer was designed such that the spectral signatures of water and the PEM could be investigated using IR light. The microfluidic PEM electrolyzer was fabricated using four layers that are assembled in a sandwich stack as shown in *Fig. 5-1 a, b*. From bottom to top, the four layers include: (1) a double-side polished silicon wafer (279 μm thickness and 50.8 mm diameter, Siegert Wafer), (2) a commercially available polydimethylsiloxane (PDMS) film (PF-40/1.5-X0, 38 μm thickness, Gel-Pak), (3) a commercially available PEM (Aquivion E87-05S, Solvay), and (4) another double-side polished silicon wafer. A schematic of the complete

electrolyzer is shown in *Fig. 5-1c*, where the desired path of ion transport can be seen. The chip is semi-transparent in multiple windows of IR light ranging from 4 μm to 12 μm wavelengths (833 cm^{-1} to 2500 cm^{-1} wavenumbers), as shown in *Fig. 5-1d*. The transparency of the electrolyzer and of water determined the upper wavelength limit (or lower wavenumber limit) of the experimental spectral range (~11.3 μm wavelengths or 885 cm^{-1} wavenumbers), while its lower wavelength limit (or upper wavenumber limit) was determined by the instruments in the experimental setup (e.g. FTIR spectrometer and detector). Details of the spectral range of the spectroscopy setup are detailed in *Section 5.2.3*.

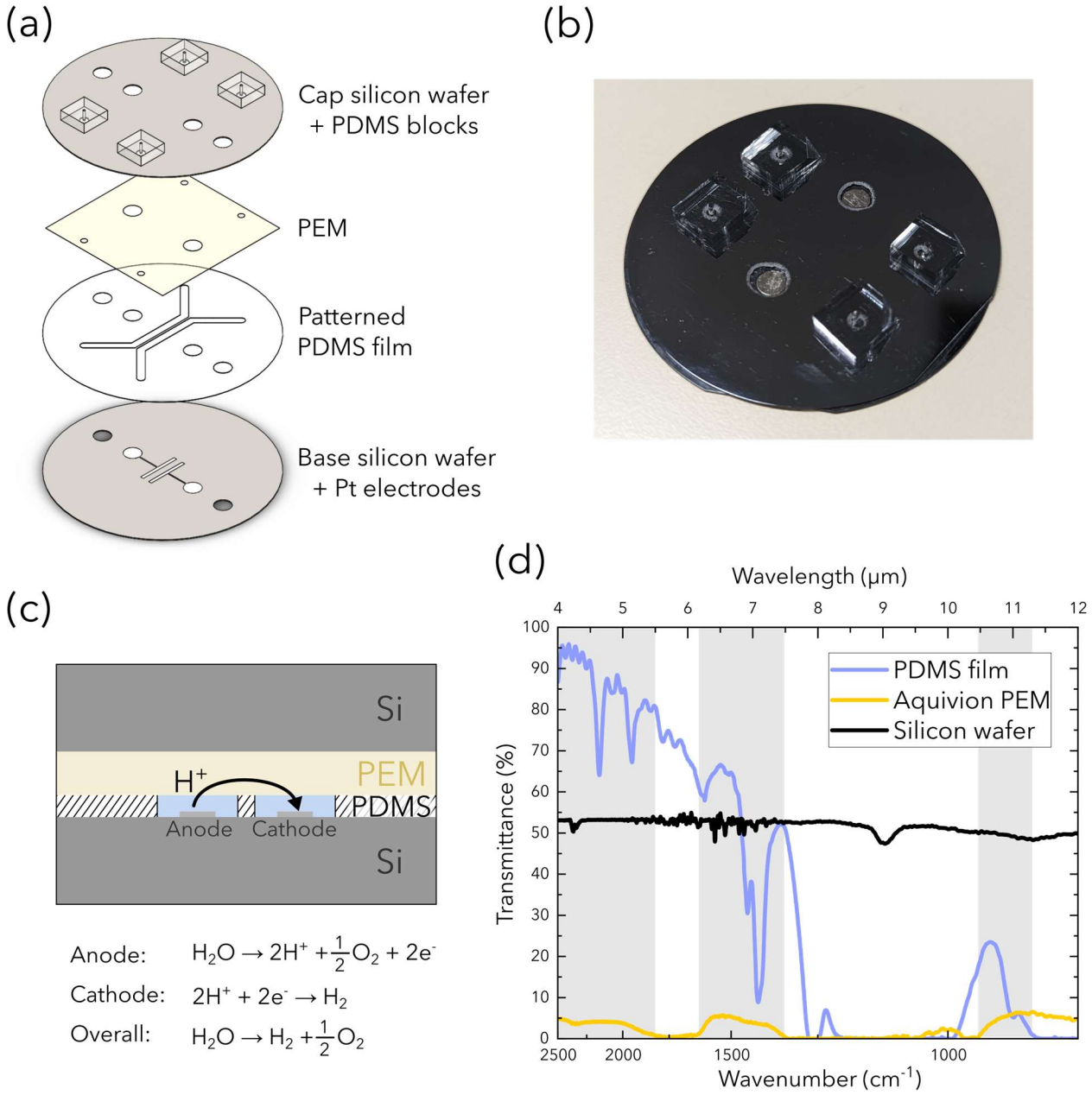

Fig. 5-1: (a) Exploded schematic showcasing each of the four layers that the microfluidic PEM electrolyzer is comprised of. (b) Photo of the fully assembled microfluidic electrolyzer. (c) Side-view of the electrolyzer showing the path of H^+ ion transport. (d) The transmittance of all materials that were used to fabricate the electrolyzer, where common transmission ranges for the materials are indicated with a shaded background.

Before fabricating the electrolyzer, each layer aside from the PEM required pre-treatment (*Fig. **5-2**a*). The bottom silicon wafer has two electrodes deposited onto its surface via two-stages of sputter-coating: first with a titanium adhesion layer (~60 nm thickness), second with platinum

(~300 nm thickness). The area occupied by a single electrode's parallel strip at the center of the wafer was considered to be the active area of the chip: 0.08 cm^2 (1 cm length × 0.08 cm width), with an inter-electrode distance of 1.2 mm. The PDMS film layer has microfluidic channels and electrode ports removed via a plotter cutter (Graphtec). The two parallel channels at the center of the chip were separated by 500 µm, and each channel has dimensions of 15 mm length × 1.8 mm width with a channel height of 38 µm (equal to PDMS film thickness). The cap silicon wafer needed to have tubing and electrode ports removed. As the wafer's transparency cannot be compromised to maintain the material's IR transparency, the front and back surfaces were protected with tape. The positions of tubing and electrode ports were marked using a permanent marker, then the holes were created with a sand blasting machine. Before proceeding with the electrolyzer fabrication routine, the tape was removed and the cap silicon wafer was cleaned with isopropanol to remove any remaining sand particles.

The chip assembly procedure consisted of four steps to create two subassemblies and adhere them together. First (*Fig.* ***5-2****b*), the PDMS film was adhered to the base silicon wafer by swelling the PDMS film with isopropanol, thereby reducing the friction between the PDMS film and bottom silicon wafer. This simplified alignment between the platinum electrodes and microfluidic channel features in the PDMS film. After alignment, the components were adhered together by insertion into a degassing chamber for 30 min to remove any remaining isopropanol or gas particles between the PDMS film and silicon wafer. This completed adhesion for the bottom subassembly.

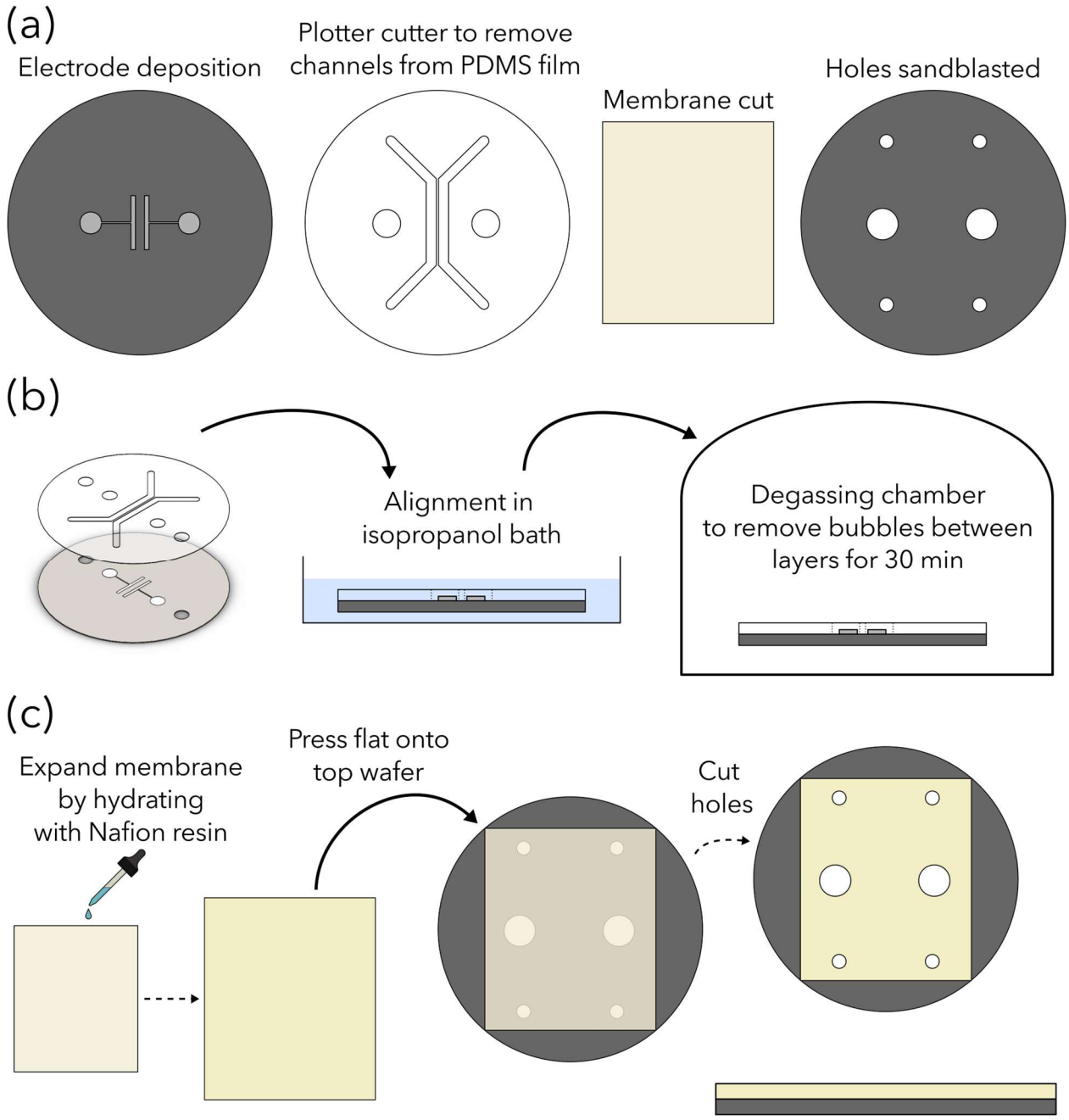

Fig. 5-2: (a) The pre-treatment of each component used to build the microfluidic PEM electrolyzer. (b) To create the first subassembly, the PDMS film with channels removed and bottom silicon wafer were inserted into an isopropanol bath and aligned. Then, they were inserted into a degassing chamber for 30 min to remove any remaining bubbles between the two layers, finishing the first subassembly. (c) The PEM was expanded with Nafion resin to reduce the effect of membrane expansion/shrinking, then pressed flat onto the top wafer, and dried. After drying, the holes for inlet, outlet, and electrode connections were cut to complete the second subassembly.

Second (*Fig.* ***5-2c***), the PEM was adhered to the top silicon wafer. In-plane expansion and shrinking is a key membrane characteristic that complicates the process of adhering the PEM to other materials, as PEMs can exhibit in-plane expansion of up to 200 % at 23 °C and 50 % relative humidity.[166] For chip fabrication specifically, excessive membrane expansion/shrinking would either lead to delamination between layers in the chip, or undesired repositioning of the electrode/tubing ports. In an attempt to reduce the range of membrane expansion and shrinking, the PEM was pre-swelled with a perfluorinated resin solution (Nafion 1100 W resin, Sigma-Aldrich). The PEM was then firmly pressed onto the cap silicon wafer to induce mechanical adhesion before being air dried. Once dry, electrode and tubing ports were carefully removed with a scalpel, then the PEM was subsequently inserted into an oven set to 65 °C overnight to complete the top subassembly.

Third (*Fig.* ***5-3a***), each subassembly was chemically bonded together through a method prepared by Pham and Barz.[167] The chemical bonding method is detailed as follows: a 4.0 wt% aqueous solution of vinyltriethoxysilane (VTES) in ethanol containing 10 vol% water was prepared and stirred for 1 h at room temperature. This created free-floating silane particles in the aqueous solution. The PDMS surface was air plasma treated, then immersed in the VTES solution for 2 min to allow silanes to migrate to the PDMS surface. The PDMS was then air dried and heated at 100 °C on a hot plate for 15 min to create siloxane linkages between the silanes and the PDMS. Towards the end of the 15 min hot plate heating, the PEM was also prepared for bonding with air plasma treatment. The two subassemblies were visually aligned, then the silane-grafted PDMS film and plasma-treated PEM surface were compressed together between two acrylic plates.

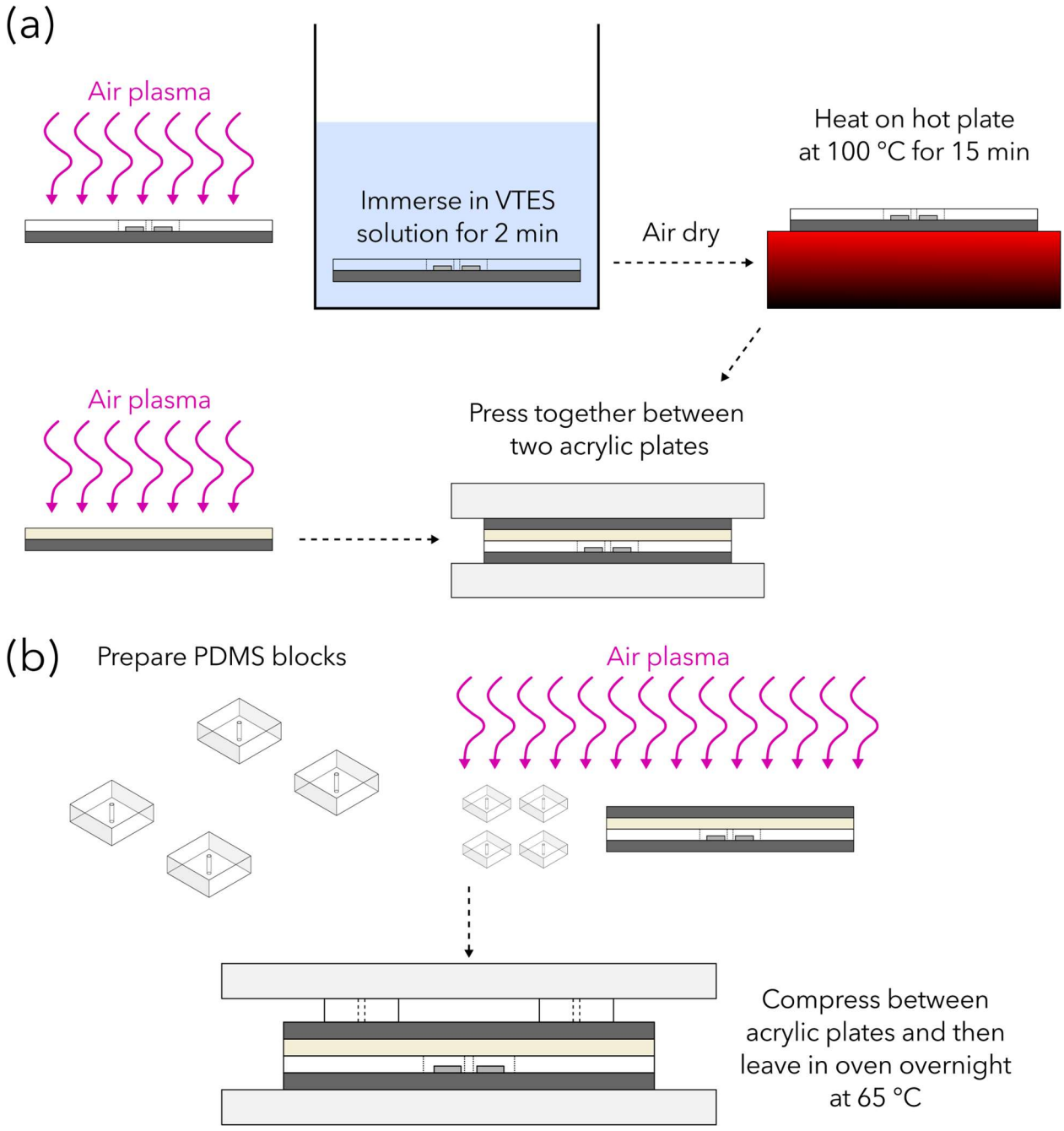

Fig. 5-3: (a) For the third step of the fabrication method, the lower subassembly was plasma treated then immersed in the VTES solution. After immersion, it was heated on a hot plate, and the top assembly was plasma treated then compressed together to bond subassemblies. (b) To complete the chip, PDMS blocks were attached used as tubing connections after plasma treating the PDMS blocks and the top of the incomplete subassembly. The chip was then complete and left compressed between acrylic plates in an oven overnight set to 65 °C.

Finally (*Fig.* ***5-3b***), four PDMS blocks with punched-holes as well as the top of the incomplete chip were prepared with air plasma treatment to bond these parts together. When attached, the PDMS blocks created inlet/outlet tubing ports on the chip. The chip was then compressed between the acrylic plates again, and inserted into the 65 °C oven overnight for completion.

5.2.2 Experimental procedure

Prior to the imaging experiments, the PEM electrolyzer was broken in using an alternating constant voltage script to improve the cell's electrochemical performance. The script was modified from the fuel cell procedure published by Klug for water electrolysis,[168] such that the break-in procedure for the electrolyzer cycled through potentiostatic operation at 2 V, 2.25 V, then 2.5 V for 1 min each and repeated for a total of 20 cycles over 1 hour (*Fig.* ***5-4***). Reactant water was supplied to both channels of the electrolyzer at a flow rate of 100 μL min^{-2} through a syringe pump (Cetoni Nemesys), and potentiostatic operation was applied through a potentiostat (BioLogic SP-300). At the beginning of the break-in script and at a potential of 2.5 V, the chip was achieved current densities of 3 mA cm^{-2}, which increased above 6 mA cm^{-2} at the same potential by the end of the break in script.

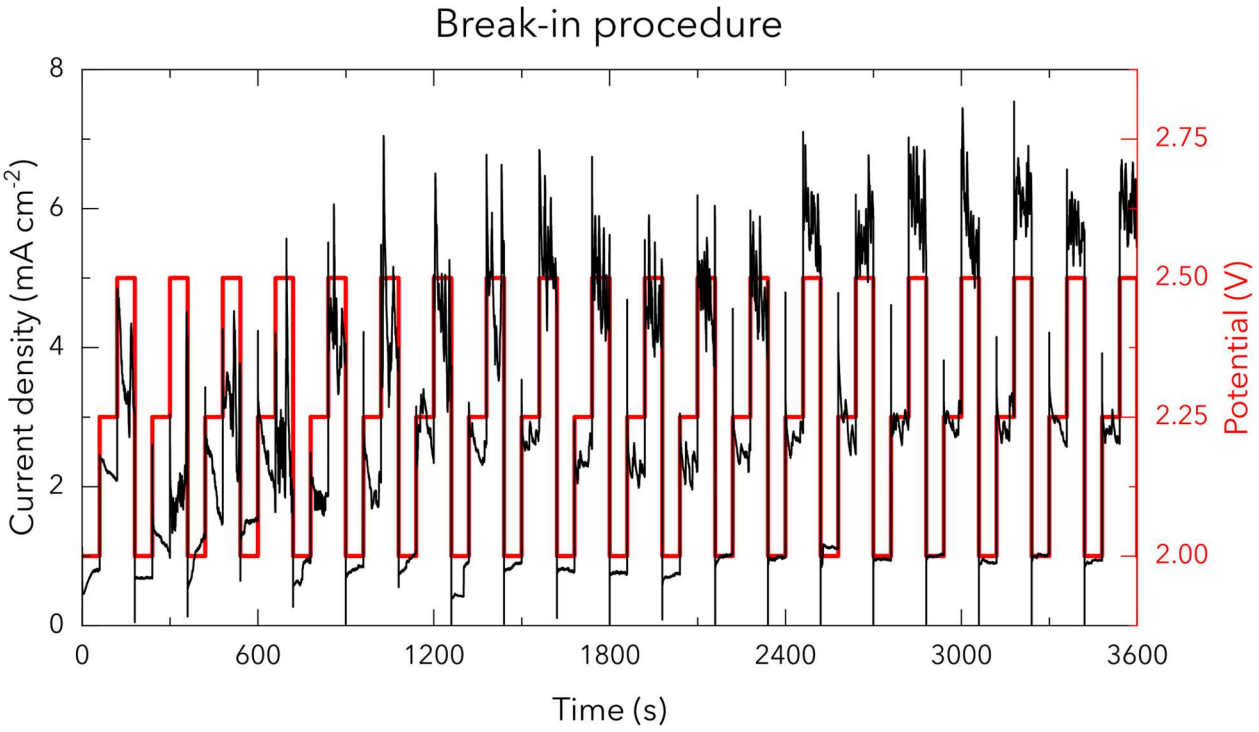

Fig. 5-4: Current density and potential as a function of time from the script to break-in the PEM of the microfluidic water electrolyzer.

The water content in the PEM of the microfluidic electrolyzer was evaluated over a range of operating conditions while IR spectra were concurrently acquired. The imaging experiments were performed for three temperature conditions and for two flow rates. The three temperature conditions (20 °C, 40 °C; and 60 °C) were selected to observe the effect of operating temperature on the PEM water content, and the two operating flow rates for the electrolyzer were 20 µL min^{-1} and 100 µL min^{-1}, which were respectively selected to induce ohmic and mass transport driven cell failure. The temperature of the electrolyzer was monitored and controlled via a copper thermistor (Captec, design shown in *Appendix A*) that is placed directly underneath the chip. The copper thermistor was operated through an externally connected proportional integral-derivative controller (working principles detailed in *Appendix A*). Dilute sulfuric acid (0.5 mol L^{-1}) was supplied to both channels to perform water splitting under acidic conditions. While a parasitic reaction is known to occur between platinum and sulfuric acid,[169] this reaction is only expected to occur at potentials lower than the standard potential of electrochemical water splitting (E_{rev} = 1.23 V at standard conditions). For these experiments, the reactant sulfuric acid was supplied to the electrolyzer through a syringe pump at the prescribed flow rate for 5 min before

current was applied. Current was delivered to the electrolyzer beginning at open circuit voltage (OCV) and was increased in increments of 25 mA cm^{-2} until cell failure for each operating condition. Cell failure was arbitrarily defined as $E > 5$ V to avoid excessive corrosion on the materials for the microfluidic chip. Each constant current was held for 20 min, and staircase galvanostatic EIS was performed between each constant current condition in increasing 2.5 mA cm^{-2} current density steps.[170] All tested experimental conditions are shown in *Tab. 5-1*.

Tab. 5-1: The experimental conditions achieved by the microfluidic PEM electrolyzer during the operando experiment.

Flow rate ***q*** (µL min^{-1})	Temperature ***T*** (°C)	Current density ***i*** (mA cm^{-2})
20	20 40 60	OCV, 25, 50, 75
100	20	OCV, 25, 50, 75, 100, 125
	40	OCV, 25, 50, 75, 100, 125, 150, 175
	60	OCV, 25, 50, 75, 100, 125, 150, 175, 200, 225

5.2.3 Operando synchrotron Fourier transform infrared spectroscopy

Experiments were performed at the far-infrared beamline Canadian Light Source synchrotron facility in Saskatoon, Canada (*Fig. 5-5 a, b*). IR light was extracted from one of the bending magnets of the synchrotron's storage ring using a split mirror and was redirected to the far-infrared beamline. At the far-infrared beamline, the light traveled to the entrance of a Bruker IFS125HR spectrometer equipped with a KBr beamsplitter via a series of optic elements. Optics within the

sample compartment of the spectrometer collimated the beam by directing it through a diamond window to a Cassegrain objective. The objective focused the beam to 90 µm spot (*Appendix B*) on the electrolyzer (*Fig. 5-5c*), the beam was then attenuated and collected by a second objective that recollimated it. Finally, the light was focused into a He-cooled detector using a gain of 500 (Ge:Cu element with a range of 335-1300 cm^{-1} wavenumbers or 7.69-30 µm wavelengths, QMC Instruments). The detector determined the lower wavelength limit for the experiment. When considering the transparency of the electrolyzer as shown before in *Fig. 5-1d*, the usable spectral range was roughly from 10.5 µm to 11.3 µm wavelengths (or 952 cm^{-1} to 885 cm^{-1} wavenumbers, respectively).

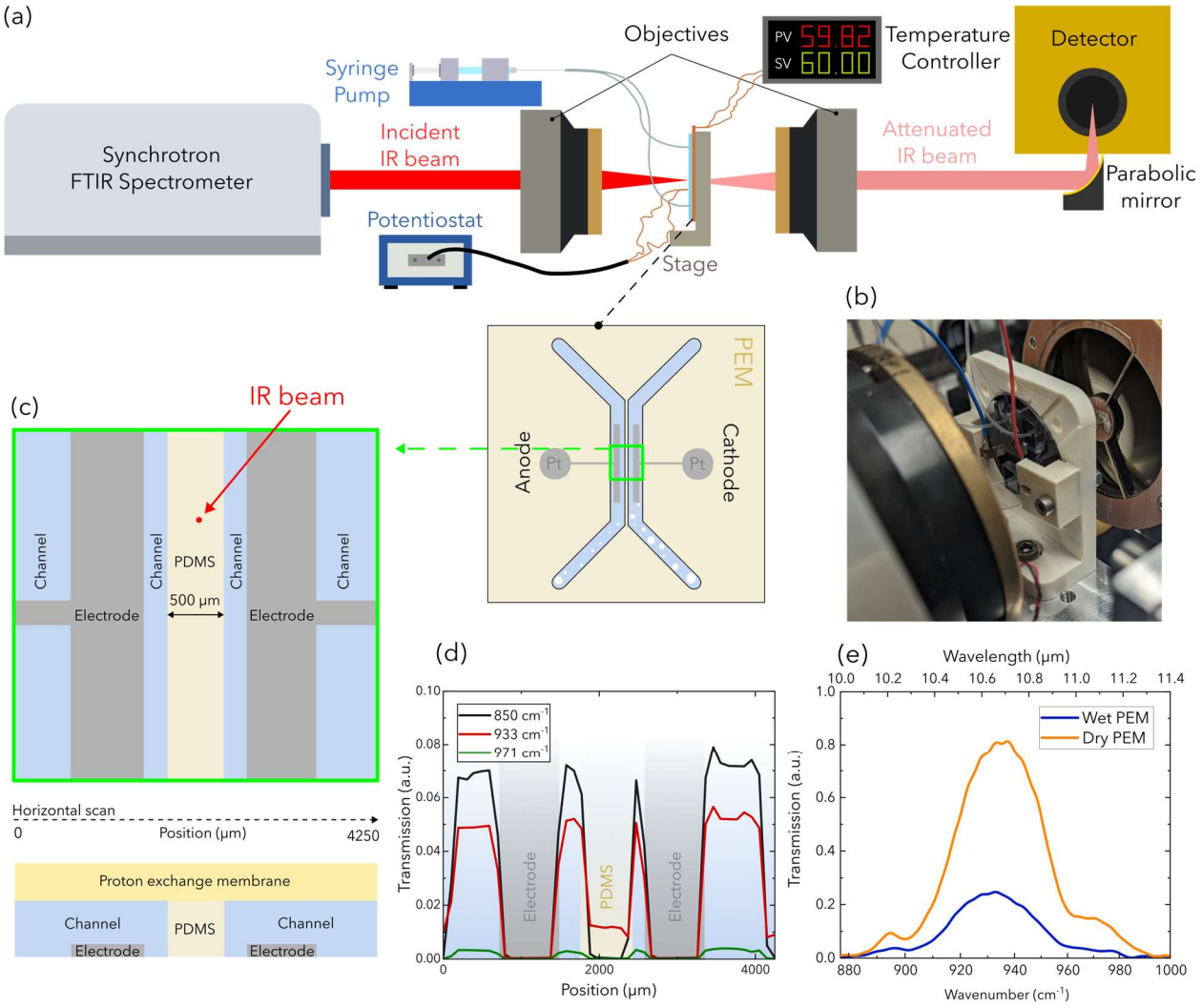

Fig. 5-5: (a) Schematic of the experimental setup for infrared spectroscopy at the Canadian Light Source synchrotron facility and (b) a photo of the chip mounted on the stage. Horizontal scans across both channels were performed with the following (c) beam position for the overhead view and the rotated view is shown directly underneath. (d) The corresponding transmissions of three wavenumbers near the common transmission range of each attenuating material were evaluated to position the beam. When centered on the PDMS strip, (e) the attenuated IR beam transmitted less IR light when the PEM was wet compared to when it was dry.

The microfluidic PEM electrolyzer was designed without any beam-alignment features, therefore the position of each chip feature had to be manually identified using individually acquired IR spectra. The chip was aligned to the beam, and then a series a horizontal scans across the chip were acquired using a monochromatic beam. The acquired scans were acquired for wavenumbers of 850 cm^{-1}, 933 cm^{-1}, and 971 cm^{-1} (11.76 µm, 10.72 µm, and 10.30 µm wavelengths, respectively) in *Fig. 5-5d*, where the transmission of each cell component in the horizontal scans is labeled. All subsequently acquired IR spectra were obtained with the beam positioned as shown in *Fig. 5-5c*, where the beam was only attenuated by the PEM, the PDMS film, and each silicon wafer of the chip. Consequently, any changes in the IR transmittance were attributed to water content changes in the PEM and PDMS film, such as the wet and dry conditions shown in *Fig. 5-5e*. IR spectra were acquired for the last 120 s of OCV and each constant current condition to allow the potential response of the chip to stabilize. Each IR spectra obtained was averaged over 300 measurements with a spectral resolution of 4 cm^{-1} and is shown in *Appendix C*.

5.2.4 PEM water content

The IR spectrum acquired during OCV was used as the reference state I_0 and IR spectra acquired with current applied to the chip were used as the operating states I. The attenuation coefficient for water μ_w was determined based on the transmission data for 1 µm of liquid water at room temperature (25 °C) published by Hale and Querry, which is also available on the Refractive index database for convenience.[171,172] The change in the transmission of water was neglected for higher temperatures, as changes in the thermal transmission coefficient can be on the order of 10^{-3} K^{-1}.[56] The transmission data of Hale and Querry was interpolated over the cropped wavelength range

between 9.8 μm and 11.5 μm (1020 cm^{-1} and 870 cm^{-1}, respectively) through the following polynomial fit:

$$\boldsymbol{T_w(\lambda) = -0.026\lambda^2 + 0.504\lambda - 1.497} \qquad \textit{Eq. 5-1}$$

where T_w is the transmission of water and λ is the wavelength of light being transmitted. The transmission for the characteristic length of 1 μm of water (l_c) was then converted to the absorbance per μm of water (μ_w [μm^{-1}]) through the following negative base 10 logarithmic function:

$$\boldsymbol{\mu_w(\lambda) = -\log_{10}\left(\frac{T_w(\lambda)}{100\%}\right)\frac{1}{l_c}} \qquad \textit{Eq. 5-2}$$

Acquired spectra or images were processed through the Beer Lambert law to determine the change in membrane water content l_w (μm) from its reference state I_0 to its operating state I:

$$\boldsymbol{l_w(\lambda) = -\frac{1}{\mu_w(\lambda)} log\left(\frac{I(\lambda)}{I_0(\lambda)}\right)} \qquad \textit{Eq. 5-3}$$

Following the Beer Lambert law, l_w values were averaged $(\overline{l_w})$ over wavelengths surrounding the IR transmission peak of interest (10.4 μm to 10.9 μm wavelengths or 962 cm^{-1} to 917 cm^{-1} wavenumbers). The following relation was used to convert $\overline{l_w}$ to the percent change in water saturation (ΔS [%]) relative to the thickness of the PEM and PDMS film:

$$\boldsymbol{\Delta S = \frac{\overline{l_w}}{t_{PEM+PDMS}}} \qquad \textit{Eq. 5-4}$$

where $\boldsymbol{t_{PEM+PDMS}}$ is the combined thickness of the PEM and PDMS film, measured ex situ to be 106 μm. Positive $\boldsymbol{\Delta S}$ values corresponded to increased membrane hydration, and negative $\boldsymbol{\Delta S}$ values corresponded to membrane drying. $\boldsymbol{\Delta S}$ was used to quantify changes in membrane hydration instead of through $\boldsymbol{\lambda_{H_2O}}$ as in *Eq. 4-1* for clarity. Specifically, values for $\boldsymbol{\lambda_{H_2O}}$ are unitless and unknown for the reference state acquired at $\boldsymbol{I_0}$, since IR spectra were only acquired after the PEM had been hydrated to a degree. Additionally, using a $\boldsymbol{\lambda_{H_2O}}$ value may be heavily skewed as only a single data point acquired through IR spectroscopy. Therefore, $\boldsymbol{\Delta S}$ was used to interpret changes in membrane hydration as a percentage.

5.3 Results and discussion

5.3.1 Electrochemical performance

The electrochemical performance of the chip was monitored to examine the performance of the PEM during operation. Polarization curves for all operating conditions are presented in *Fig. 5-6a*, where each point on the polarization curve was averaged from the final 120 s of constant current operation. Each flow rate was chosen to target either ohmic or mass transport dominated overpotential. Specifically, the lower flow rate (20 µL min^{-1}) was chosen to target mass transport dominated overpotential and exhibited exponential increases in cell potential followed by immediate cell failure. This was confirmed by each lower flow rate condition failing after an applied current density of 75 mA cm^{-2}. In contrast, the higher flow rate (100 µL min^{-1}) was chosen to target ohmic dominated overpotential. Considering the polarization curves with the higher flow rate, a linear trend was observed for each temperature condition, confirming ohmic dominated overpotential. Additionally, higher temperatures enabled higher current density operation and exhibited reduced slopes (*Fig. 5-6a*), which indicated either reduced ohmic overpotentials or improved reaction kinetics.

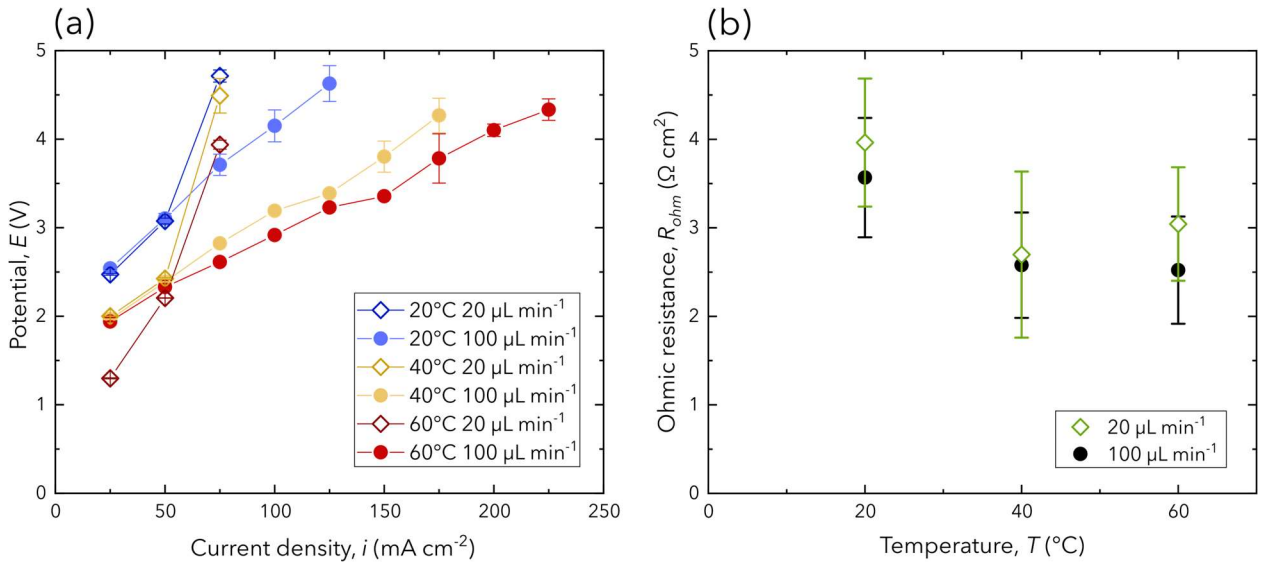

Fig. 5-6: (a) The polarization curve of all experimental conditions, where each point is presented as the average potential from the final 120 s of galvanostatic operation. (b) The ohmic resistance

averaged over each current density from staircase galvanostatic EIS. Error bars are reported as the standard deviation.

Given the novelty of the electrolyzer design, a comparison of its electrochemical performance to similar designs and industrial grade PEM electrolyzers needed to be evaluated to assess the viability of the acquired results. The ohmic resistance of the operating chip was extracted through a combination of EIS and fitting the equivalent electrical circuit used by Chevalier et al. and is reported in *Appendix D*.[126] *Fig. 5-6b* shows the ohmic resistance for each experimental condition, which was averaged over each current density from staircase galvanostatic EIS. While this design excels in its transparency in the IR domain bordering mid- and far-IR, the ohmic resistance was an order of magnitude higher than conventional electrolyzer and fuel cell stacks.[146,173] Additionally, ohmic resistance measurements were highly unstable due to the chip's high sensitivity to gas formation, residence, and removal at the small active area (0.08 cm^2). The high ohmic resistance and instability were due to the large path of ion transport. Ions were required to traverse from the anode through 38 μm of 0.5 mol L^{-1} sulfuric acid to the PEM, through a minimum of the 1.2 mm inter-electrode distance, then back through the sulfuric acid to the cathode. Nevertheless, the chip was able to achieve competitive current density operation (>25 mA cm^{-2} at 2.5 V) with other similarly designed electrolyzers (lit.,[174,175] 17.5 mA cm^{-2} at 2.5 V).

5.3.2 Polymer electrolyte membrane water content

The PEM hydration in the operating chip was quantified and compared to the respective potential response at each operating condition. The PEM hydration was expressed as the change in water saturation from the reference state (OCV), as calculated in *Eq. 5-4*. In *Fig. 5-7a*, the change in water saturation for each current density at a flow rate of 20 μL min^{-1} is shown, where mass transport overpotential was the cause of cell failure. At this flow rate, the PEM water content showed insignificant changes until the highest achieved current density (75 mA cm^{-2}), when a reduction in the membrane water content occurred. This behavior was observed for each temperature condition with the largest decrease of -0.57 % in water saturation at cell failure, which could be interpreted as membrane drying. Specifically, at the lower flow rate, product gas was less likely to be removed from the channel, which dried the membrane and increased mass transport overpotentials, causing cell failure. This behavior is confirmed in the literature using X-ray and

neutron based techniques,[19,146,176] and validates the presented FTIR spectroscopy setup as a method for discriminating the cause of cell failure based on the PEM hydration.

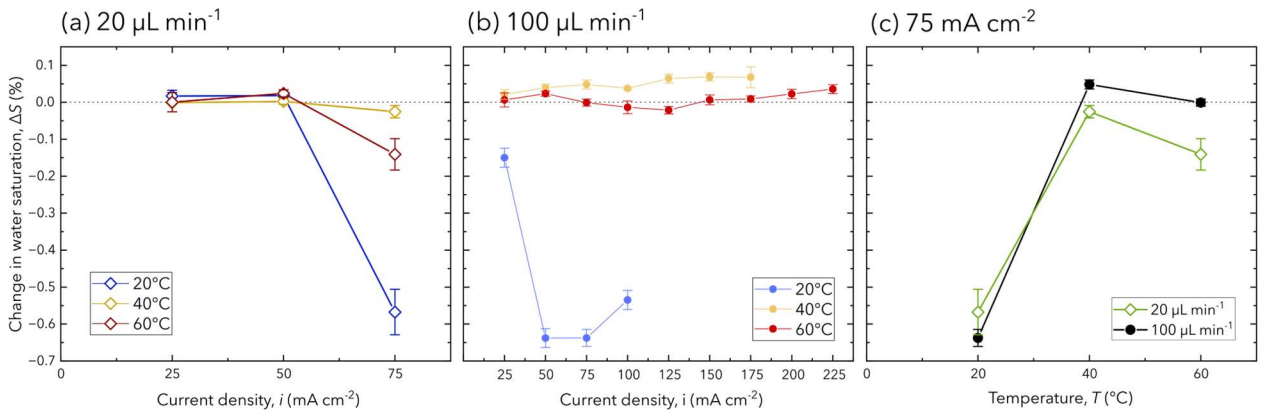

Fig. 5-7: The change in PEM water saturation for each operating condition at a flow rate of (a) 20 µL min^{-1}, (b) 100 µL min^{-1}, and (c) for both flow rates and at a current density of 75 mA cm^{-2}. Error bars are reported as the standard deviation for each measurement in the cropped IR spectrum.

At a flow rate of 100 µL min^{-1}, the change in PEM water saturation showed both increases and decreases (*Fig. 5-7b*), for which no concurrent changes in the electrochemical performance (*Fig. 5-6a*) were observed. Comparable membrane drying to the low flow rate condition was observed to occur at 20 °C for current densities from 50 mA cm^{-2} to 100 mA cm^{-2}; however, the higher flow rate of 100 µL min^{-1} was able to sustain electrochemical performance up to a failing current density of 125 mA cm^{-2}. This behavior was expected, as the higher flow rate was able to provide sufficient reactant delivery and product removal, which enabled improved current density operation dominated by ohmic losses. However, at temperatures of 40 °C and 60 °C, membrane drying was not observed, and changes in the PEM water saturation were within 0.1 % for all current densities. The difference in measurements across all temperature conditions at 100 µL min^{-1} was attributed to the nature of FTIR spectroscopy, as the area for characterization was limited to the 90 µm beam spot size.

For both flow rates, the change in membrane water content was significantly lower for higher temperatures. In *Fig. 5-7c*, the relationship between the change in water saturation and temperature

is presented for a current density of 75 mA cm^{-2}, for which the largest reductions in the membrane water content were observed at 20 °C. At higher temperatures (40 °C and 60 °C), all experimental conditions (flow rate and current densities) showed changes in membrane water content within -0.2 % to 0.1 %, which were attributed to the PEM's higher water uptake for higher temperatures. This was supported by the literature, which reported that higher temperatures in PEMs were associated with higher electro-osmotic drag coefficients, water uptake, and protonic conductivity.[177–180] Additionally, further increases in membrane hydration from the reference state did not occur, despite the performance increase from 40 °C to 60 °C (*Fig. 5-6a*). Therefore, the performance increase was attributed to improved ohmic performance or reaction kinetics at higher temperatures.

5.4 Chapter summary

A microfluidic PEM electrolyzer that is semi-transparent in the IR domain (bordering mid- and far-IR) was developed as a platform for characterizing the operando PEM water content. Two modes of electrochemical failure were explored to observe the membrane water content over a range of applied temperatures. The lower flow rate drove mass transport-dominated cell failure up to current densities of 75 mA cm^{-2}, for which a reduction in membrane water content occurred, while the higher flow rate drove ohmic-dominated cell failure and sustained improved current densities of up to 225 mA cm^{-2}. The electrochemical performance of this chip was comparable to similar architectures presented in the literature but was specifically designed to be semi-transparent in IR, enabling the membrane water content measurements. While the ohmic resistance of the chip was an order of magnitude higher than a conventional full-scale fuel cell or electrolyzer, this could be reduced by optimizing the large path of ion transport.

The membrane hydration was characterized via operando synchrotron FTIR spectroscopy for the first time, where the change in water saturation was measured while current was applied. A reduction in water saturation was observed immediately before cell failure for the lower flow rate conditions (largest reduction of ΔS was -0.57 %), which demonstrated membrane drying with cell failure. Furthermore, the change in water saturation and temperature was observed for both flow rates, where the improved water uptake with higher temperatures (i.e. 40 °C and 60 °C) caused the least variation in the membrane water content (which ranged from -0.2 % to 0.1 %).

The results presented in this chapter acted as a first step for evaluating the PEM in an operating electrolyzer using IR techniques. While results using this configuration were limited to local information at the IR beam's position on the chip, this aspect is improved for the work in the following chapter which implements a suitable IR source and camera, thus enabling the visualization of global water transport through the PEM. Nonetheless, these methods and results using FTIR spectroscopy were sufficient for determining effects of membrane hydration on electrochemical performance of the electrolyzer.

6 Investigating inter-electrode water diffusion in a microfluidic polymer electrolyte membrane electrolyzer via operando infrared spectroscopic imaging

6.1 Introduction

In this chapter, a combination of both classical and novel characterization techniques was applied to the infrared (IR) transparent electrolyzer fabricated in the previous chapter to distinguish loss sources and improve our understanding of transport mechanisms within the polymer electrolyte membrane (PEM) of the electrolyzer. This was achieved by operating the electrolyzer with three H_2SO_4 anolyte concentrations under potentiostatic operation. It was found that while electrochemical performance was relatively similar between each anolyte concentration, the standard deviation of the measured current densities increased with higher anolyte concentrations. A combination of electrochemical impedance spectroscopy (EIS) and distribution of relaxation times (DRT) was applied to quantify ohmic losses and to elucidate the effect of anolyte concentration on discrepancies between their electrochemical performances. Additionally, kinetic and mass transport losses were found through these techniques and was observed to become larger for higher anolyte concentrations. Then, global electrochemical results were compared to global imaging results presented as the channel wetness of the electrolyzer from images. The cathode channel wetness in particular was higher for higher anolyte concentrations while the anode channel wetness remained constant, indicating that a water diffusion gradient from anode to cathode developed for higher anolyte concentrations.

These water diffusion gradients were investigated through local regions within images. Profiles of water diffusion gradients in the PEM was found to be dependent on the local adjacent channel's wetness. Furthermore, the change in the PEM's water hydration between electrodes was visually quantified for the first time. Based on the results of this chapter, we recommend that the electrolyzer fabrication be further developed to include components similar to porous transport layers that are common in industrial water electrolyzers. Effective water management in the electrolyzer channels will promote consistent PEM and channel wetness, thereby enabling

investigation water transport in the PEM under improved conditions. This work is currently in preparation for submission as a journal article.

6.2 Methods

6.2.1 Break-in procedure

A pristine microfluidic PEM electrolyzer was fabricated (methods detailed in *Section 5.2.1*), and the same break-in procedure from Klug – used in the previous chapter that was modified for use with water electrolysis – was applied again here to improve the electrochemical performance of the electrolyzer.[168] Specifically, the electrolyzer was operated under potentiostatic conditions with a potentiostat (BioLogic SP-300) that cycled through 2 V, 2.25 V, and 2.5 V for 2 min at each potential and was repeated for 30 cycles for a total break-in time of 3 hours. As experiments in this chapter were performed at I2M, the length of the break-in procedure could be extended compared to the experiments performed at the synchrotron facility in the previous chapter, for which beam time was limited. The first 2 hours of the break-in procedure were performed with DI water (18.2 MΩ cm) to break in the membrane. The DI water was supplied to the electrolyzer with a syringe pump (Cetoni Nemesys) at a flow rate of 100 μL min^{-1} for each channel. For the last hour of the break-in procedure, reactants for both channels were replaced with 0.1 mol L^{-1} sulfuric acid to replicate the acidic water-splitting conditions that the electrolyzer would be operated at for experiments. DI water was used for the break-in procedure instead of H_2SO_4 to limit any possible corrosion of the Pt electrodes that may occur when interacting with H_2SO_4. This was to preserve the electrolyzer, as the fabrication method is irreversible. Nonetheless, Pt corrosion with 0.1 mol L^{-1} H_2SO_4 was not expected to be significant for the break-in procedure at this time scale.[169]

6.2.2 Experimental setup

An in-house IR spectroscopy setup (*Fig. 6-1*) was developed for operando imaging of the PEM electrolyzer. Light was produced from a black body source with a temperature of 1400 K. The emitted light was collimated (Thorlabs ID75Z/M) and then filtered to a wavelength of 4 μm

(wavenumber of 2500 cm^{-1}) using a band pass filter. The filtered beam was collimated again (Thorlabs ID25/M) before being attenuated by the sample, and then captured by an IR camera (FLIR SC7000 with InSb sensor). Images were captured with a spatial resolution of 21.6 μm px^{-1}. A computer was connected to the IR camera and a chopper positioned between the first collimator and the band pass filter to align the frequency of the chopper to the camera's frame rate. The synchronization between the chopper and the IR camera was configured such that captured images would alternate between raw images (I_{raw}) and dark-field images (I_{dark}), as shown in *Fig. 6-1c* and *Fig. 6-1d*. Raw images in *Fig. 6-1c* show the features of the microfluidic electrolyzer, where the PEM covers the entire image, each channel can be seen, as well as the respective electrodes that block the beam. Additionally, liquid reactants and gaseous products can be visually differentiated through differences in the image's digital level (DL). A higher concentration electrolyte flowed through the anode channel for the sample image shown *Fig. 6-1c* and *Fig. 6-1d*, which attenuated the beam more than the electrolyte that flowed through the cathode channel.

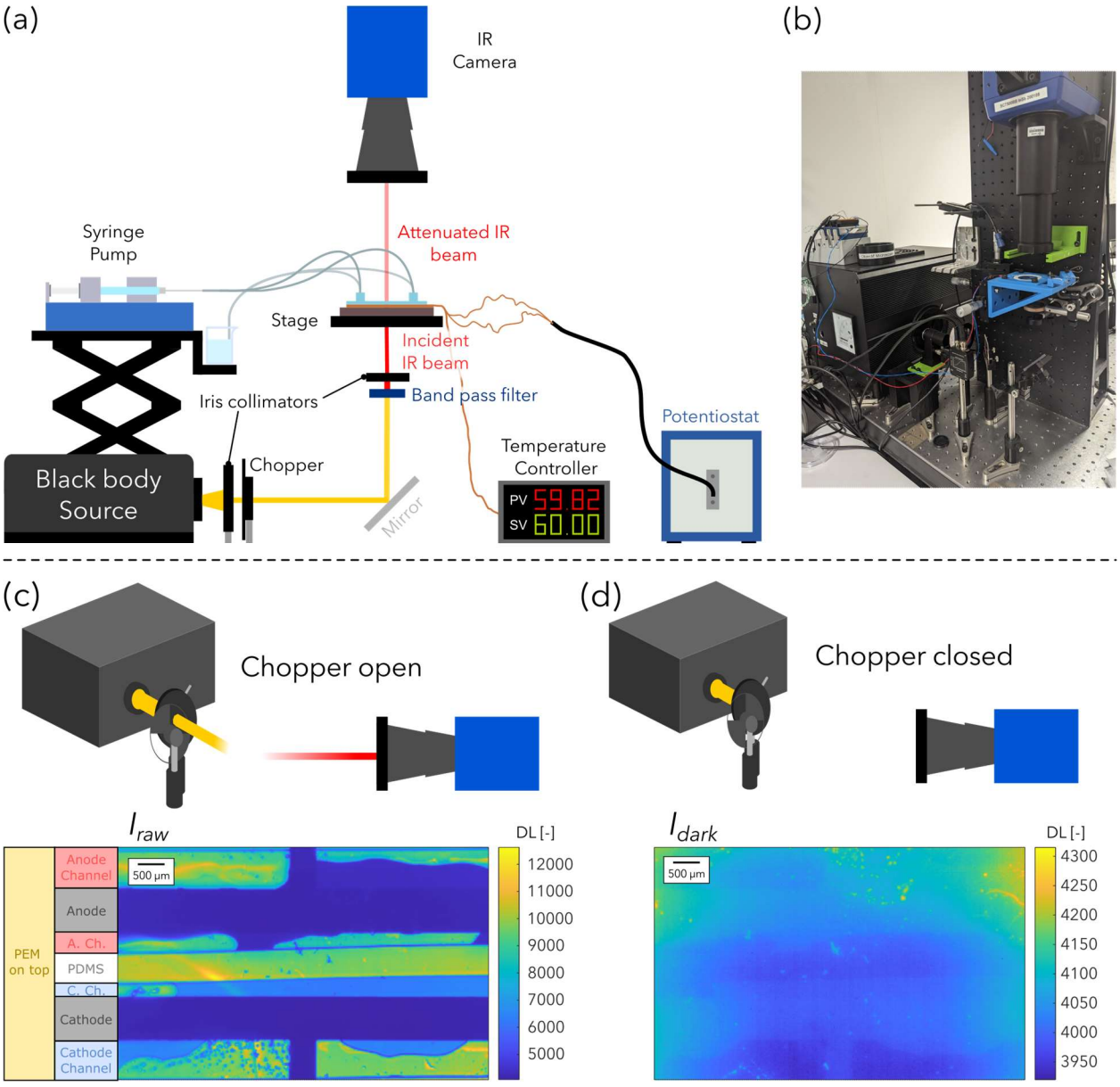

Fig. 6-1: (a) Schematic of the experimental setup used. (b) Photo of the experimental setup without the microfluidic electrolyzer, potentiostat, temperature controller, and syringe pump. When the chopper is (c) open, raw images I_{raw} are captured, and when the chopper is (d) closed, dark images I_{dark} are captured.

6.2.3 Experimental protocol

The water content in the PEM of the microfluidic electrolyzer was determined for acidic water splitting using dilute H_2SO_4 electrolyte while IR images were concurrently acquired. For acidic

water splitting, protons (H^+ ions) are consumed at the cathode (*Eq. 1-2*). Supplying higher anolyte H_2SO_4 concentrations was hypothesized to saturate the H^+ ion availability in the anolyte channel. Moreover, characterizing different electrolyte concentrations is well suited for the combination of microfluidics and spectroscopy. If the increased proton concentration in the anode channel increases the electro-osmotic drag rate of water molecules through the membrane to the cathode, water gradients would ideally manifest between the anode and cathode that could be visualized through the IR images.

To exaggerate this phenomenon, three anolyte concentrations (0.1 mol L^{-1}, 0.5 mol L^{-1}, and 1.0 mol L^{-1}) were selected and the catholyte H_2SO_4 concentration was held constant at 0.1 mol L^{-1}. A syringe pump was used to flow each reactant at 100 μL min^{-1}, and the temperature of the electrolyzer was held constant at 60 °C through a custom copper thermistor (Captec, *Appendix A*) that was inserted between the electrolyzer and the stage. The temperature of the copper thermistor was controlled through an externally connected proportional-integral-derivative (PID) controller (details in *Appendix A*). Both the reactant delivery to the electrolyzer and its temperature control were maintained for 15 min before potential was applied.

The electrolyzer operation was separated into 4 cycles per anolyte concentration for a total of 12 cycles. Each cycle consisted of open circuit voltage (OCV) operation for 30 s, then a constant potential step at 2.5 V for 15 min, followed by three potentiostatic EIS sweeps centered at 2.5 V with an amplitude of 10 mV (frequencies from 5 MHz to 50 mHz with 10 steps per decade). Immediately after beginning OCV, 500 frames of images were acquired at a frequency of 25 Hz every 5 min until the potentiostatic EIS sweeps were complete. Eight images were acquired for each cycle and concentration, with exceptions of seven images acquired for cycle 1 and cycle 3 with 0.1 mol L^{-1} anolyte. A schematic describing the experimental protocol is shown in *Fig. 6-2*. Each 500 frame image stack acquired images alternating between I_{raw} and I_{dark}, such that 250 frames of each were acquired per image stack.

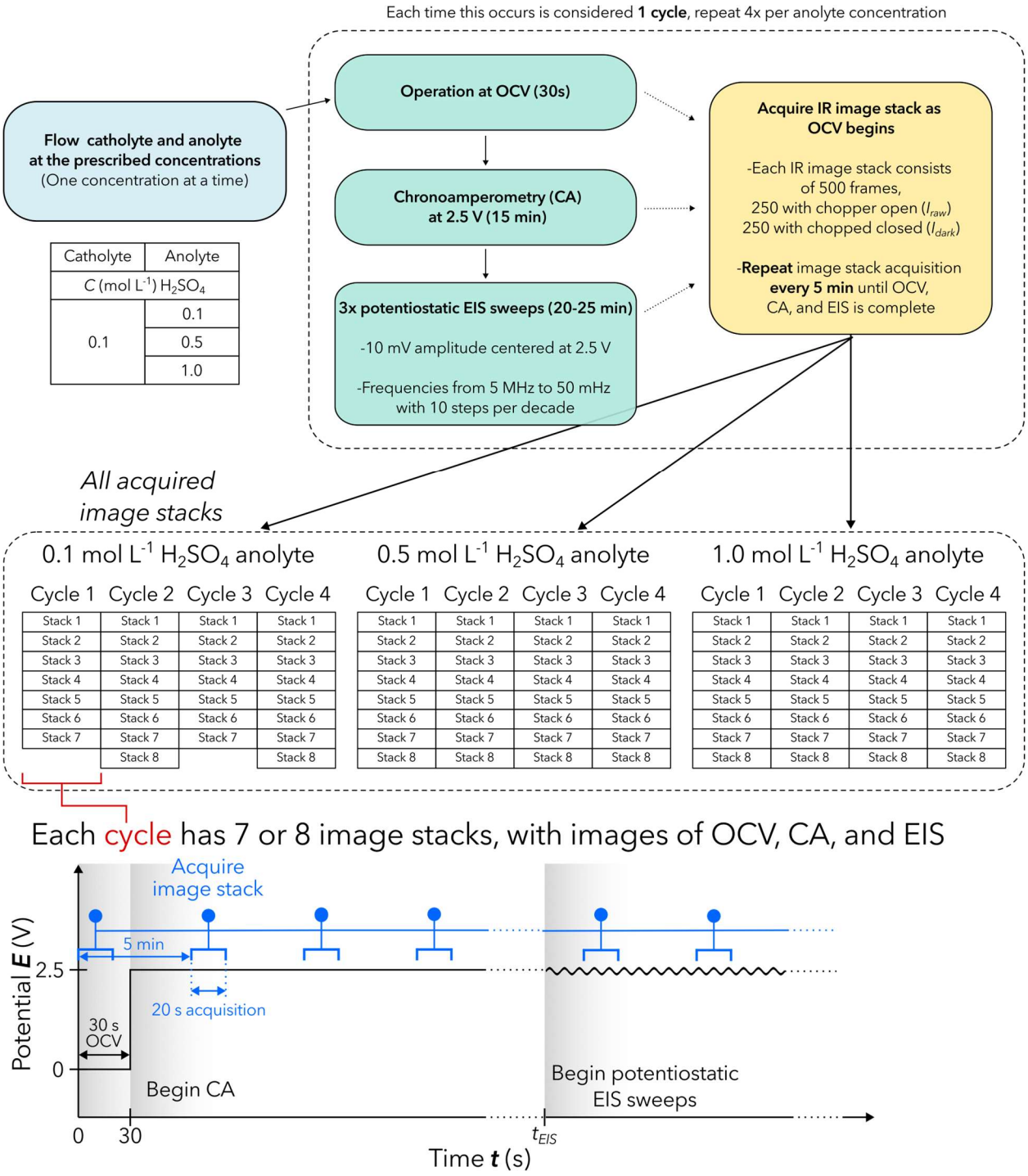

Fig. 6-2: Flowchart schematic of the experimental protocol. The number of acquired images for each cycle and anolyte concentration of the experiment is shown.

6.2.4 Anolyte concentration

As the anolyte concentration was varied for these experiments, the effects of its fluidic properties must be evaluated as they may strongly affect the electrolyzer performance. For example, the volume of electrolyte in contact with the electrode surface (i.e. the usable active area) may be affected by the changing anolyte viscosity. There are two measures of fluid viscosity, dynamic and kinematic. Dynamic viscosity is a measure of a fluids internal resistance, and kinematic viscosity is the ratio of the dynamic viscosity to its density.[181] The relevant parameters for the viscosities of each anolyte concentration are shown in *Tab. 6-1*. Relative to the lowest H_2SO_4 concentration of 0.1 mol L^{-1}, the intermediate H_2SO_4 concentration of 0.5 mol L^{-1} has a 6 % higher kinematic viscosity and an 8 % higher dynamic viscosity, and the highest H_2SO_4 concentration of 1.0 mol L^{-1} H_2SO_4 has a 13 % higher kinematic viscosity and an 18 % higher dynamic viscosity. Fluidic properties of the anolyte (and catholyte) are directly tied to the mass transport of the electrolyzer, as critical electrochemical mechanisms such as the usable active area of the cell or local/global bubble generation and removal are strongly influenced by these parameters.[14,15,182]

Tab. 6-1: Fluidic properties of H_2SO_4 for each concentration used in experiments.[183–185]

Concentration $\boldsymbol{C}$ (mol L^{-1})	Density $\boldsymbol{\rho}$ (g mL^{-1})	Kinematic viscosity $\boldsymbol{\nu}$ (cSt or mm^2 s^{-1})	Dynamic viscosity $\boldsymbol{\mu}$ (cP or mPa s)
0.1	1.01	1.01	1.02
0.5	1.03	1.07	1.10
1.0	1.06	1.14	1.21

6.2.5 Changes in membrane hydration

Acquired images must be processed using a rewritten Beer Lambert law due to the experimental setup. As the IR camera captures both IR light and the proper emission of the sample, the proper

emission component must be removed to determine the amount of IR light attenuated by the sample. The proper emission of the sample can be determined through simple means, either by turning the beam off or blocking it to capture dark-field images, such as when the chopper is closed. Consequently, the revised Beer Lambert law can be rewritten as such:

$$\boldsymbol{l_w(x,y,t) = -\frac{1}{\mu_w} log\left(\frac{I(x,y,t) - I_{dark}(x,y,t)}{I_0(x,y,t) - I_{0,dark}(x,y,t)}\right)} \qquad \textit{Eq. 6-1}$$

where I is the operating image acquired while potential is applied to the electrolyzer [-], I_0 is the reference image acquired while the electrolyzer is operated at OCV [-], I_{dark} is the dark-field image acquired with the chopper closed [-], μ_w is the attenuation coefficient for water at a wavelength of 4 µm [µm^{-1}], and l_w is the change in the length of water through which the beam is attenuated from the reference state to operating state [µm]. As images were acquired alternating between I (previously denoted as I_{raw}) and I_{dark}, the subsequent I_{dark} frame was subtracted from the previous frame of I when *Eq. 6-1* was applied. A water attenuation calibration was performed using the experimental setup detailed in *Section 6.2.2* to calculate μ_w at the specified wavelength, which was determined to be $5.9 \cdot 10^{-3}$ µm^{-1} (*Appendix E*). The change in the length of water in the beam path can be converted to the change in membrane hydration ($\overline{\lambda_{H_2O}}$) [-] through the following relation:

$$\boldsymbol{\overline{\lambda_{H_2O}}(x,y,t) = \frac{C_{w,px^2}(x,y,t)}{C_{SO_3H,px^2}}} \qquad \textit{Eq. 6-2}$$

where C_{w,px^2} is the concentration of water in the PEM per square pixel [mol px^{-2}] and C_{SO_3H,px^2} is the equivalent per sulfonate site in the PEM [mol px^{-2}]. Each concentration component can be determined through the following equations:

$$\boldsymbol{C_{w,px^2}(x,y,t) = \frac{l_w(x,y,t)\rho_w res_{px}}{M_w}} \qquad \textit{Eq. 6-3}$$

$$\boldsymbol{C_{SO_3H,px^2} = TAC\ \rho_{PEM}\ t_{PEM}\ res_{px}} \qquad \textit{Eq. 6-4}$$

where ρ_w and ρ_{PEM} are the densities for water and the PEM [g cm^{-3}], respectively, res_{px} is the resolution of a square pixel [μm^2 px^{-2}], M_w is the molar mass of water [g mol^{-1}], TAC is the total acid capacity of the PEM [g mol$_{SO3H}^{-1}$],[166] and t_{PEM} is the thickness of the PEM [μm].

In the literature, membrane hydration is typically denoted through λ (λ_{H_2O} here for clarity), which is the water content of the PEM.[94,101,177,180,186,187] λ_{H_2O} is typically measured ex-situ to quantify the PEM water content when hydrated from a completely dry reference state. It is important to note the difference between the λ_{H_2O} reported in the literature and $\overline{\lambda_{H_2O}}$ here, which is change in water content of the PEM from the reference state at OCV (from l_w in *Eq. 6-1*), instead of being completely dry. $\overline{\lambda_{H_2O}}$ is used as a value relative to λ_{H_2O}, as it is unfeasible to reliably and repeatedly acquire images of the a completely dry membrane for the electrolyzer design used here. This is because completely dehydrating the membrane causes membrane shrinkage, which introduces the risk of leaks for the electrolyzer channels. Furthermore, there are a couple more issues that make this unfeasible, such as accurately aligning the electrolyzer to the camera over the experimental time scale (ranging over a couple days) and a perfect experimental setup. As images were acquired throughout the experiment, any minor misalignments of the electrolyzer's positioning between the reference and operating images would require lengthy image post-processing routines. By a perfect experimental setup, this would be under the assumption that the power of the blackbody source is constant, and that the DL captured in images acquired by the camera would also be consistent over the experimental time period. None of these conditions represent real-world measurements, which is why $\overline{\lambda_{H_2O}}$ was determined with reference to the water content of the membrane from OCV.

Consequently, $\overline{\lambda_{H_2O}}$ values determined from *Eq. 6-2* were lower than other studies that present λ_{H_2O} through ex-situ measurements.[66,180] Therefore, a comparable metric to other studies, such as by Chadha et al.,[94] is the difference in membrane hydration between electrodes $\Delta\lambda_{H_2O}$, which is expressed as:

$$\boldsymbol{\Delta\lambda_{H_2O} = \lambda_{H_2O,a} - \lambda_{H_2O,c}} \qquad \textit{Eq. 6-5}$$

where $\lambda_{H_2O,a}$ and $\lambda_{H_2O,c}$ represent the membrane water content at the anode and cathode, respectively. $\lambda_{H_2O,a}$ and $\lambda_{H_2O,c}$ cannot be directly measured, as the IR beam is attenuated by either

the electrodes or any electrolyte in the channels near the electrodes. Therefore, $\overline{\lambda_{H_2O}}$ values can be substituted for $\lambda_{H_2O,a}$ and $\lambda_{H_2O,c}$, such that $\Delta\overline{\lambda_{H_2O}}$ can be determined.

$$\overline{\boldsymbol{\Delta\lambda_{H_2O}}}(\boldsymbol{x},\boldsymbol{y}) = \overline{\boldsymbol{\lambda_{H_2O,a}}}(\boldsymbol{x},\boldsymbol{y}) - \overline{\boldsymbol{\lambda_{H_2O,c}}}(\boldsymbol{x},\boldsymbol{y}) \qquad \textit{Eq. 6-6}$$

6.2.6 Distribution of relaxation times

The distribution of relaxation times (DRT) is a method that when combined with electrochemical impedance spectroscopy (EIS) data (e.g. Nyquist plots), can transform the data from the frequency domain to the time domain. This enables another angle of data analysis without prior knowledge of the dataset it is applied to.[124,188–190] The DRT algorithm detailed in the remainder of this section was developed by Adèle Crête Lawrence under the supervision of Stéphane Chevalier.[190] When considering data that is dependent on multiple time constants, such as EIS applied to water electrolysis, DRT analysis essentially allows the time constants to be pseudo reverse engineered by fitting them to the Voigt model. The Voigt model is a series of N_τ (total number) parallel RC circuits, for which each RC circuit has an individual time constant $\tau_k = R_k C_k$, and is described as follows:

$$\boldsymbol{Z_{DRT}} = \sum_{\boldsymbol{k=1}}^{\boldsymbol{N_\tau}} \frac{\boldsymbol{h_k}}{\boldsymbol{1 + j\omega\tau_k}} \approx \boldsymbol{Z_{meas}} \qquad \textit{Eq. 6-7}$$

where Z_{DRT} is the DRT fit of the impedance density [Ω cm^2], Z_{meas} is the measured impedance density [Ω cm^2], h_k is the absolute polarization contribution of each RC element [Ω cm^2], ω is the angular frequency, and $j = \sqrt{-1}$ is the unit imaginary number. The relationship between the distribution function $h(\tau)$ and the time constants (τ) will be used to extract information from the DRT model. Then, the DRT function $h(\tau)$ can be obtained by solving the following non-negative linear least squares problem:

$$\boldsymbol{x} = \mathbf{argmin}\left|\left|\boldsymbol{Ax} - \boldsymbol{b}\right|\right|^{\boldsymbol{2}}, \text{ such that } \boldsymbol{x_k} \geq \boldsymbol{0}\ \forall\ \boldsymbol{k} \in [\boldsymbol{1}, \boldsymbol{N_\tau}] \qquad \textit{Eq. 6-8}$$

Considering the EIS data, each matrix and vector for the problem can be expanded to consider the DRT.

$$\boldsymbol{x} = \left(\boldsymbol{h_1} \cdots \boldsymbol{h_k} \cdots \boldsymbol{h_{N_\tau}}\right)^{\boldsymbol{T}} \qquad \textit{Eq. 6-9}$$

$$\boldsymbol{b} = \begin{pmatrix} \boldsymbol{Re}\{\boldsymbol{Z_{meas}}\} \\ \boldsymbol{Im}\{\boldsymbol{Z_{meas}}\} \end{pmatrix} \qquad \textit{Eq. 6-10}$$

$$\boldsymbol{A} = \begin{pmatrix} \boldsymbol{Re}\left\{\frac{\mathbf{1}}{\mathbf{1}+\boldsymbol{i\omega_1\tau_1}}\right\} & \cdots & \boldsymbol{Re}\left\{\frac{\mathbf{1}}{\mathbf{1}+\boldsymbol{i\omega_1\tau_{N_\tau}}}\right\} \\ \vdots & \ddots & \vdots \\ \boldsymbol{Re}\left\{\frac{\mathbf{1}}{\mathbf{1}+\boldsymbol{i\omega_{N_f}\tau_1}}\right\} & \cdots & \boldsymbol{Re}\left\{\frac{\mathbf{1}}{\mathbf{1}+\boldsymbol{i\omega_{N_f}\tau_{N_\tau}}}\right\} \\ \boldsymbol{Im}\left\{\frac{\mathbf{1}}{\mathbf{1}+\boldsymbol{i\omega_1\tau_1}}\right\} & \cdots & \boldsymbol{Im}\left\{\frac{\mathbf{1}}{\mathbf{1}+\boldsymbol{i\omega_1\tau_{N_\tau}}}\right\} \\ \vdots & \ddots & \vdots \\ \boldsymbol{Im}\left\{\frac{\mathbf{1}}{\mathbf{1}+\boldsymbol{i\omega_{N_f}\tau_1}}\right\} & \cdots & \boldsymbol{Im}\left\{\frac{\mathbf{1}}{\mathbf{1}+\boldsymbol{i\omega_{N_f}\tau_{N_\tau}}}\right\} \end{pmatrix} \qquad \textit{Eq. 6-11}$$

However, this model cannot be applied directly to EIS data from an electrolyzer, as the measured impedance from these systems includes a constant contribution from the ohmic resistance of the electrolyzer. Therefore, an extended DRT (eDRT) to include the Ohmic resistance (R_Ω) is rewritten as:

$$\boldsymbol{Z_{eDRT}} = \sum_{\boldsymbol{k=1}}^{\boldsymbol{N_\tau}} \frac{\boldsymbol{h_k}}{\mathbf{1}+\boldsymbol{i\omega\tau_k}} + \boldsymbol{R_\Omega} \qquad \textit{Eq. 6-12}$$

The equivalent electrical circuit (EEC) for the eDRT is shown in *Fig. 6-3*. The addition of the R_Ω component can be processed simply as this parameter can be appended to the solution vector $x = \left(h_1 \ldots h_{N_\tau}, R\right)$, while no changes in vector b are required, and the A matrix required an additional column:

$$\boldsymbol{A} = \begin{bmatrix} \boldsymbol{A_{Re}} \in \mathbb{R}^{\boldsymbol{N_f}\times\boldsymbol{N_\tau}} & \mathbf{1} \in \mathbb{R}^{\boldsymbol{N_f}\times\mathbf{1}} \\ \boldsymbol{A_{Im}} \in \mathbb{R}^{\boldsymbol{N_f}\times\boldsymbol{N_\tau}} & \mathbf{0} \in \mathbb{R}^{\boldsymbol{N_f}\times\mathbf{1}} \end{bmatrix} \qquad \textit{Eq. 6-13}$$

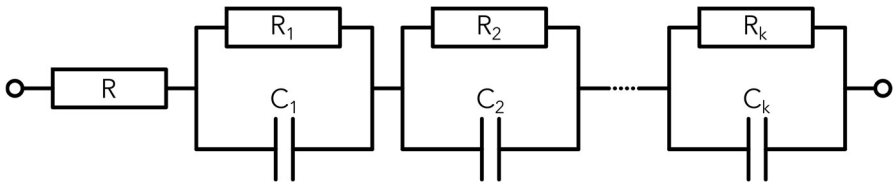

Fig. 6-3: The equivalent electrical circuit used for the DRT model circuit.

Then, the problem could be solved to obtain the distribution function $h(\tau)$ from the eDRT. The total area under the fitted eDRT curve was expected to be relative to the total polarization of the system. Next, the eDRT can be decomposed into individual Gaussian peaks, where each peak provides information of a unique physical process and is represented by one RC element in the EEC. The time constant τ of each peak is considered to be the frequency at which the average of each Gaussian peak is centered. The capacitance of each RC element can then be estimated by dividing the average by the area of the Gaussian peak. It is important to note that the number of decomposed peaks obtained is dependent on the quality of the dataset, and that the physical processes in the electrochemical device do not directly correspond to the behavior of RC elements.

DRT optimization problems are ill-posed, therefore requiring regularization to obtain meaningful results. Tikhonov regularization is the most widely used DRT regularization method, which is known to introduce bias to the cost function in order to reduce the variance of the solution.[191] The following 0th order regularization is used to bias the parameter estimates towards zero.

$$\boldsymbol{x} = \boldsymbol{argmin}\left(\left|\left|\boldsymbol{Ax} - \boldsymbol{b}\right|\right|^{\mathbf{2}} + \boldsymbol{\Lambda}\left|\left|\boldsymbol{Ix}\right|\right|^{\mathbf{2}}\right) \qquad \textit{Eq. 6-14}$$

where I is the identity matrix and Λ is the regularization parameter. The larger that the regularization parameter is, the shorter and wider that distribution function peaks will be. If the parameter is too small, the impact of noise will affect the distribution, and if the parameter is too large, peaks will combine and obscure results. While higher order Tikhonov regularization exists, 0th order regularization is best suited for this application, as distribution function values are expected to be close to zero.

A sample of the EIS data was processed through the DRT method to provide a sample distribution functions for the first cycle of lowest and highest anolyte concentrations as shown in *Fig. 6-4*, where 5 peaks are observed for each dataset. Each peak corresponds to a time constant τ that is

relative to a RC element in the eDRT, for which the capacitance can be estimated as a function of the area and average of the peak. The time constants of the highest frequency peaks on the left side of graphs shown in *Fig. 6-4* correspond to the ohmic properties of the electrolyzer, which are expected to be largest for lower anolyte concentrations. On the contrary, the time constants of the lowest frequency peaks on the right side of graphs shown in *Fig. 6-4* correspond to the electrolyzer's kinetics and mass transport. Results derived from the DRT will be interpreted in a following section.

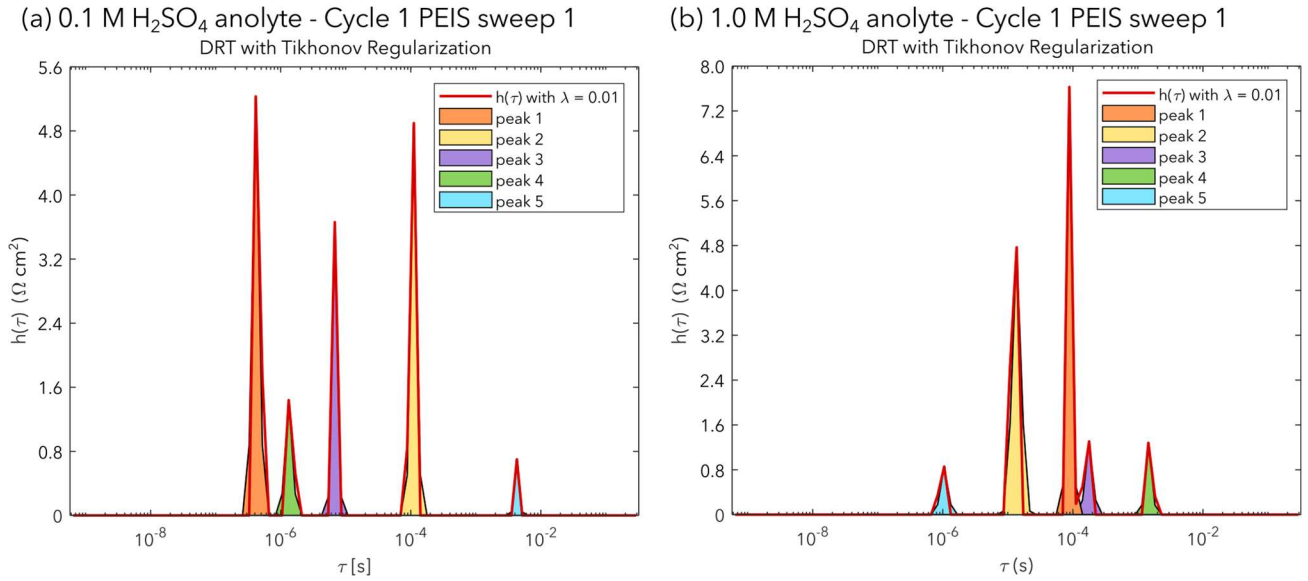

Fig. 6-4: DRT plots with Tikhonov Regularization $\mathbf{h}(\boldsymbol{\tau})$ *of the first cycle and sweep for anolyte concentrations of (a) 0.1 M* H_2SO_4 *and (b) 1.0 M* H_2SO_4*. As the input is EIS data, the highest frequency peak (left) likely corresponds to the ohmic properties of the electrolyzer, while the lowest frequency peaks (right) correspond to its kinetic and mass transport.*

6.3 Results and discussion

6.3.1 Electrochemical performance

The current density of the electrolyzer was investigated for each anolyte concentration at a potentiostatic voltage of 2.5 V. In *Fig. 6-5 a-c*, the measured current density is shown for each

anolyte concentration and cycle, for which each anolyte concentration operated in comparable current density ranges. At the beginning of operation, the current density for each anolyte solution varies between 25 mA cm^{-2} and 30 mA cm^{-2}. Towards the end of measurements, the current density drops between 15 mA cm^{-2} and 20 mA cm^{-2}. While each anolyte concentration has comparable current density performance, a clear difference can be observed for the standard deviation in current density for each anolyte concentration. Specifically, the lower the anolyte concentration, the lower its standard deviation for the measured current density. These results contrast with those reported in the literature, that report improved current density operation with increased anolyte concentration.[192,193]

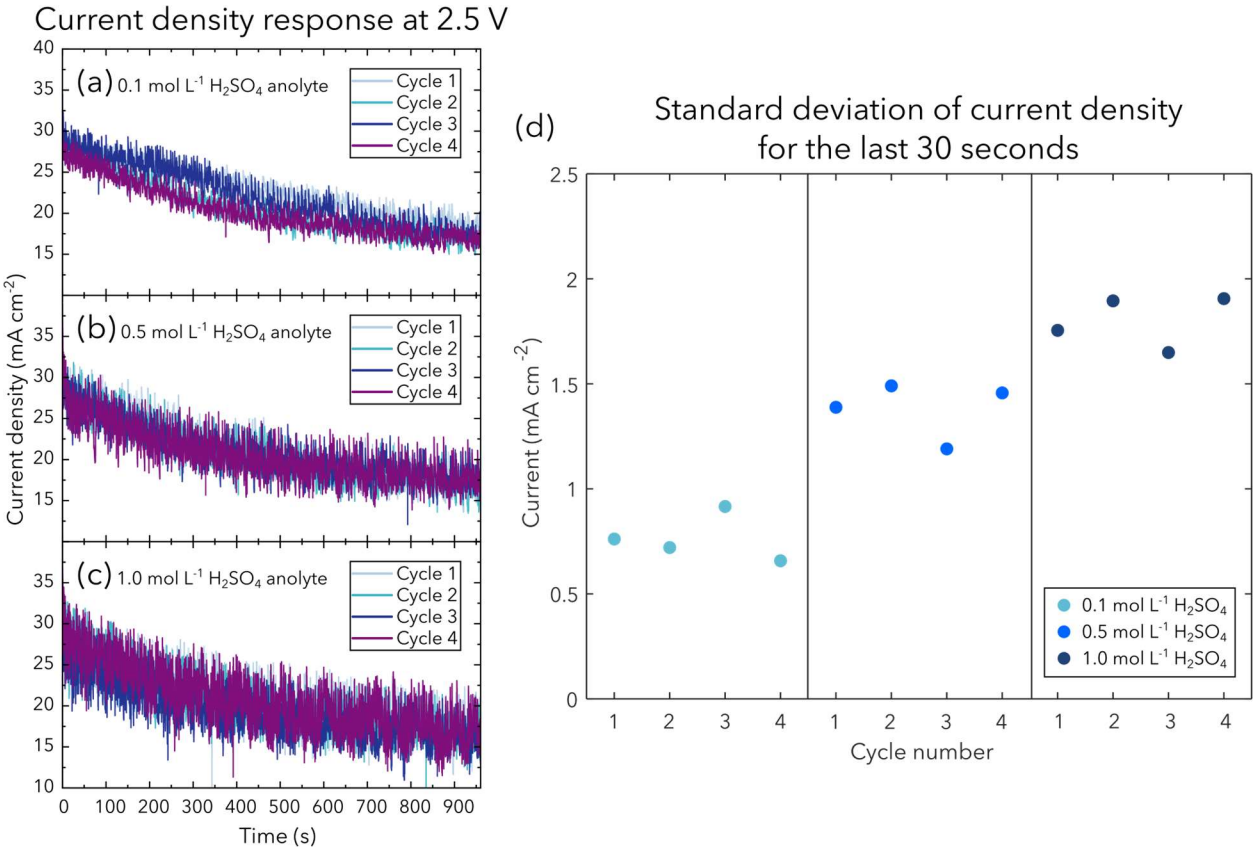

Fig. 6-5: The current density response of the microfluidic PEM electrolyzer under potentiostatic operation at 2.5 V for anolyte concentrations of (a) 0.1 mol L^{-1} H_2SO_4, (b) 0.5 mol L^{-1} H_2SO_4, and (c) 1.0 mol L^{-1} H_2SO_4. (d) The standard deviation for the last 30 seconds of current density is observed to be higher with higher anolyte concentration.

Since the difference in standard deviation measurements is unintuitive, it will be investigated through the ohmic and mass transport losses of the electrolyzer. Considering the ohmic losses, changes to the standard deviations are challenging to discern due to the geometry of the electrolyzer, as the reduction in the electrolyzer's ohmic resistance for higher anolyte concentrations are marginal due to the long path of ion transport. The impact of ohmic resistance is discussed further in *Section 6.3.2*. Considering the mass transport losses, the higher standard deviation as a response for higher anolyte concentrations could also imply higher mass transport losses for the microfluidic electrolyzer. Specifically, mass transport losses may occur due to the absence of a porous transport layer or a complex electrode surface morphology.[15] The inefficient mass transport may be dependent on the fluidic properties of the anolyte (*Tab. 6-1*). Specifically, higher anolyte concentrations have higher dynamic viscosities, which lead to reduced anolyte movement. Additional mass transport losses may occur due to dry regions in the channel that stem from the reduced anolyte movement, thereby effectively reducing the active area. The following sections will investigate the source of the measured higher current density standard deviations through DRT, EIS, and imaging data.

6.3.2 Coupling distribution of relaxation times with electrochemical impedance spectroscopy

The combination of EIS and DRT analysis can be used to clarify the physical processes that occur within the PEM electrolyzer. To reiterate how data was acquired for relevant parameters, three potentiostatic EIS sweeps were performed for each cycle and anolyte concentration. Therefore, a total of 12 sweeps (3 per cycle) were acquired for each anolyte concentration. Nyquist plots with an overlapping DRT fit for the first cycle and sweep of each anolyte concentration are shown in *Fig. 6-6 a-c*. As high frequency data provides information of the electrolyzer's ohmic resistance, the measured high frequency resistance (HFR) for each cycle and anolyte concentration is shown in *Fig. 6-6d*. The HFR is observed to be lower for each higher anolyte concentration, ranging around 4.3 Ω cm^2 for 0.1 mol L^{-1} H_2SO_4 anolyte to 4 Ω cm^2 for 1.0 mol L^{-1} H_2SO_4 anolyte. This trend in HFR measurements was expected, as the ohmic conductivity of each anolyte increases with its concentration, so 1.0 mol L^{-1} H_2SO_4 anolyte was expected to have the lowest R_Ω.

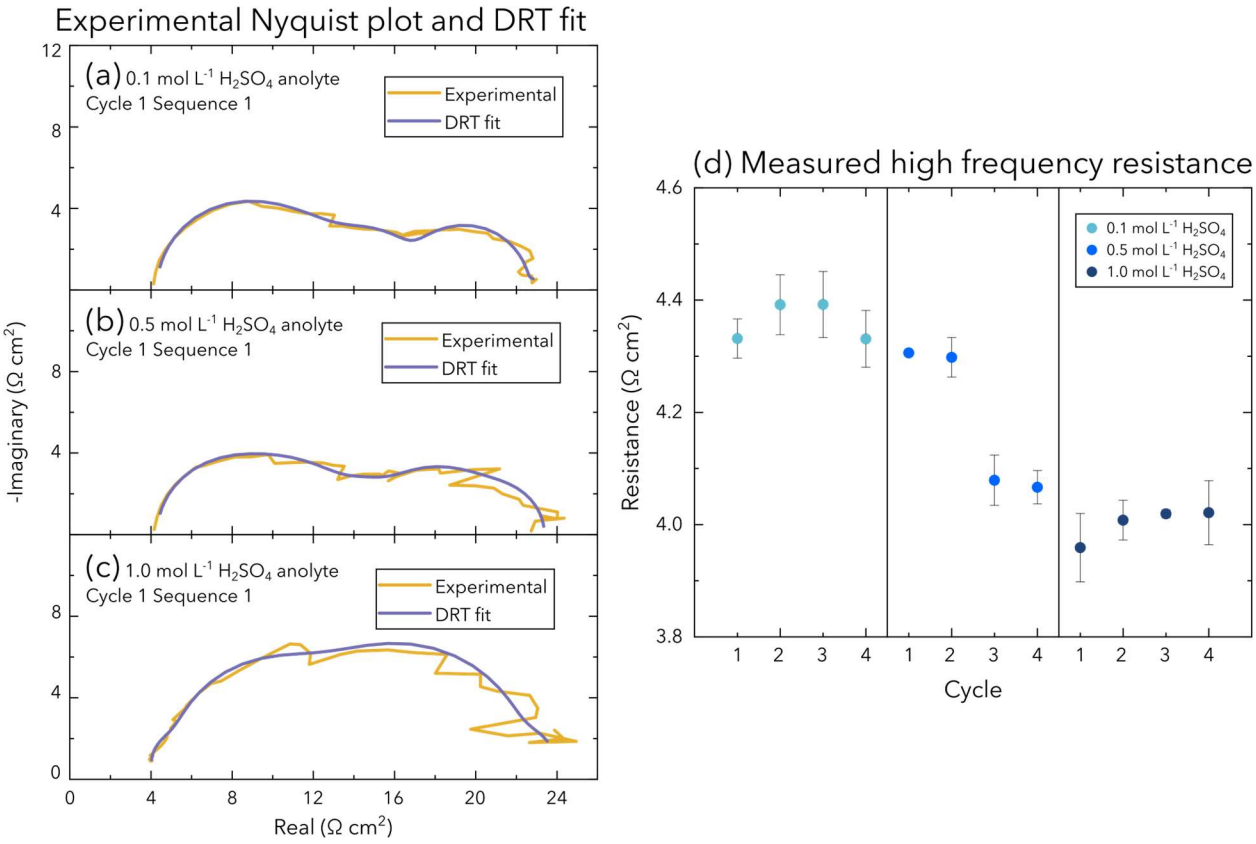

Fig. 6-6: Nyquist plots and their respective DRT fits for (a) 0.1 mol L^{-1} H_2SO_4, (b) 0.5 mol L^{-1} H_2SO_4, and (c) 1.0 mol L^{-1} H_2SO_4. (d) The measured HFR for each anolyte concentration and cycle with error bars equal to the standard deviation for the three acquired potentiostatic EIS sweeps. The HFR of an electrolyzer is associated to its ohmic resistance.

In the Nyquist plots, experimental measurements acquired at high frequencies were less noisy than those acquired at low frequencies. This can be observed in *Fig. 6-6 a-c*, for which HFR measurements (left side of Nyquist plots) align with the DRT fit much better than low frequency resistance (LFR) measurements (right side of Nyquist plots). Given that HFR measurements correspond to the ohmic losses (due to ohmic resistance) of the electrolyzer, LFR measurements correspond to the kinetic and mass losses of the electrolyzer. While LFR measurements are noisy in EIS measurements, the DRT fit can be used to discriminate the sources of losses for the electrolyzer, providing information of the cells ohmic, kinetic, and mass transport losses.[124]

The highest and lowest frequency peaks from the regularized DRT are visualized in *Fig. 6-7* for which each peak that is shown was processed through a simple low-pass area filter to remove peaks that may be produced from noise. Specifically, for each cycle, the highest, lowest, and second

lowest frequency peaks for the three EIS sweeps with an area of at least 0.8 Ω cm^2 s (10 Ω s multiplied by active area of 0.08 cm^2) were averaged. These peaks were averaged for the three sequential EIS measurements acquired during the same cycle to reduce the impact of the instability of electrochemical measurements, which can be observed in *Fig. 6-6*. For each anolyte concentration, the frequencies for the highest frequency peaks align with HFR measurements from Nyquist plots shown in *Fig. 6-6*. While the HFR can already be easily measured from Nyquist plots, information from the regularized DRT peaks provide comparable information through the areas of the peaks and the time constants which those peaks are centered around. The averaged peak areas for each anolyte concentration (from lowest to highest) and time constants can be found in *Tab. 6-2*. From low to high anolyte concentration, the time constants became larger (i.e. frequencies became smaller, respectively) while the areas became smaller. This trend in averaged peak area aligned with the trend in HFR measurements, which was expected as higher anolyte concentrations are accompanied by higher electrolyte conductivites.[194]

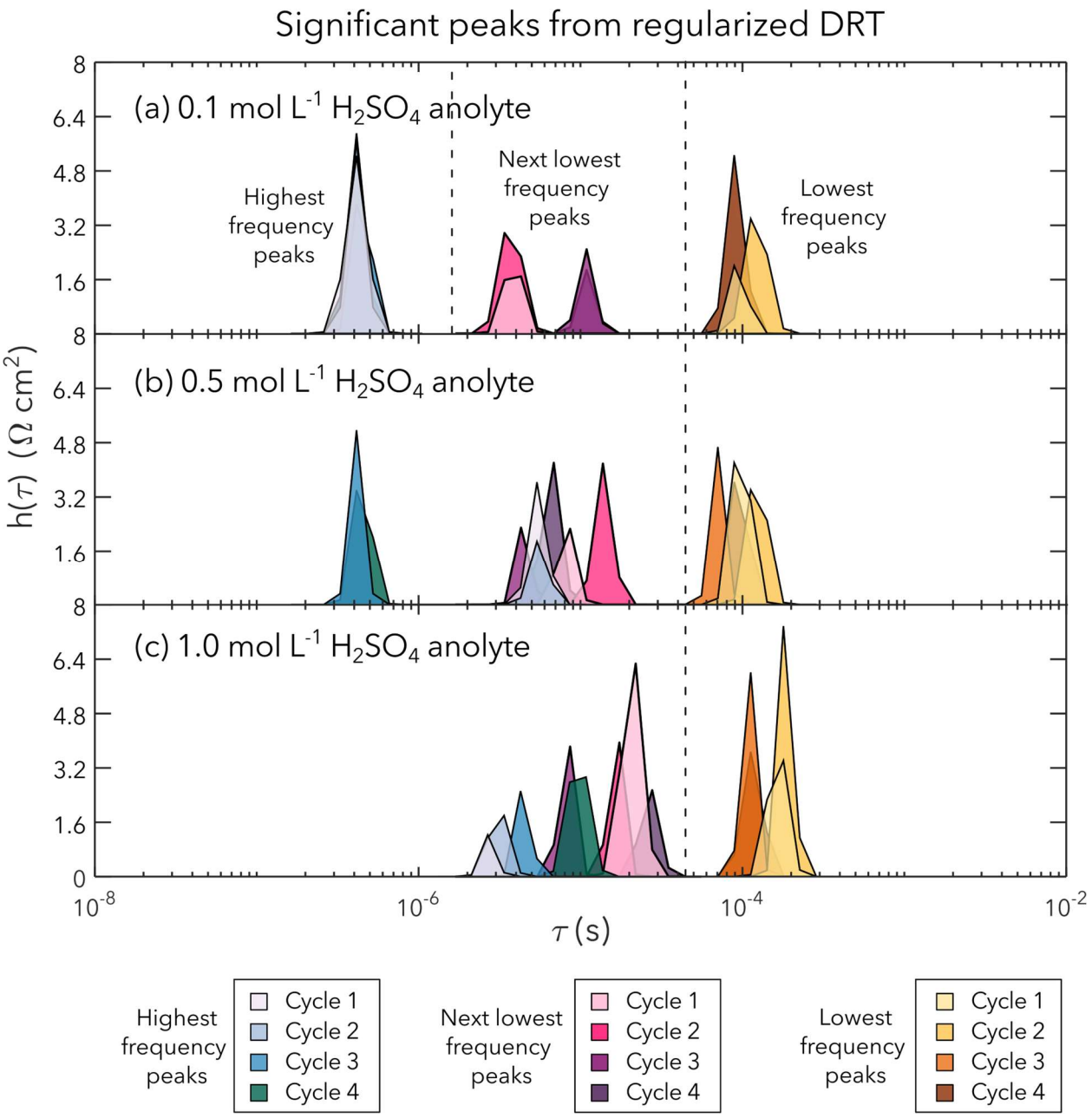

Fig. 6-7: The peaks from DRT with regularization at the highest, lowest, and second lowest frequencies after applying a low-pass area filter to remove any peaks that may be produced by noise. Highest frequency peaks correspond to the ohmic resistance, second lowest frequency peaks correspond to reaction kinetics, and lowest frequency peaks correspond to mass transport of the electrolyzer. Shown peaks are averaged from 3 sequences of potentiostatic EIS over each cycle for anolyte H_2SO_4 concentrations of (a) 0.1 mol L^{-1}, (b) 0.5 mol L^{-1}, and (c) 1.0 mol L^{-1}.

*Tab. 6-2: Peaks shown in Fig. 6-7 were averaged by peak area and time constants (**τ**) for each anolyte concentration to observe the trends, informing of ohmic, kinetic, and mass transport losses in the electrolyzer.*

Anolyte conc. (mol L^{-1})	Average of highest frequency peaks (ohmic resistance)		Average of second lowest frequency peaks (reaction kinetics)		Average of lowest frequency peaks (mass transport)	
	Time constant **τ** (s)	Area (Ω cm^2 s)	Time constant **τ** (s)	Area (Ω cm^2 s)	Time constant **τ** (s)	Area (Ω cm^2 s)
0.1	0.42×10^{-6}	7.49	1.47×10^{-5}	3.67	1.05×10^{-4}	5.05
0.5	2.98×10^{-6}	4.74	1.65×10^{-5}	4.44	0.96×10^{-4}	6.12
1.0	5.00×10^{-6}	3.41	3.59×10^{-5}	5.94	1.43×10^{-4}	6.82

The second lowest frequency peaks from the DRT are centered around a time constant of 10^{-5} (*Fig. 6-7* and *Tab. 6-2*) and represent the reaction kinetics of the electrolyzer. From low to high anolyte concentrations, the averaged time constant became larger (1.47×10^{-5} s, 1.65×10^{-5} s, and 3.59×10^{-5} s, respectively) (i.e. frequencies became smaller, respectively) while the averaged peak area became larger as well (3.67 Ω cm^2 s, 4.44 Ω cm^2 s, and 5.94 Ω cm^2 s, respectively). These trends indicate that from low to high anolyte concentrations, the reaction kinetics became slower and the corresponding losses became larger, as determined through the increasing time constants and peak areas measured for the second lowest frequency peak. The lowest frequency peaks from the DRT representing mass transport losses all roughly align at a time constant of 10^{-4} (*Fig. 6-7* and *Tab. 6-2*). From low to high anolyte concentrations, the averaged peak area became larger (5.05 Ω cm^2 s, 6.12 Ω cm^2 s, and 6.82 Ω cm^2 s, respectively). For these lowest frequency peaks, the averaged time constant does not have a monotonic trend from low to high anolyte concentration. The highest time constant (and therefore lowest frequency) is measured for the

highest anolyte concentration (1.05×10^{-4} s, 0.96×10^{-4} s, and 1.43×10^{-4} s, from low to high anolyte concentration).

For both the reaction kinetic and mass transport related DRT peaks, the averaged peak area became larger for higher anolyte concentrations. Referencing the increasing standard deviation with anolyte concentration from the previous section, the determined DRT time constants and areas can explain why the increase in the standard deviation of current density occurs for higher anolyte concentrations. Specifically, higher anolyte concentrations were accompanied by larger kinetic and mass transport losses. The larger kinetic losses could be attributed to the increased rates of platinum electrode corrosion when using higher anolyte concentrations. However, this conclusion is challenging to validate in the electrolyzer without assessing the surface quality of the electrodes between supplying different anolyte concentrations, which was not performed for the work presented in this chapter. While reaction kinetics cannot be visualized with IR images due to the platinum electrode's complete attenuation of IR, mass transport phenomena such as bubble growth and detachment can, and will be investigated in the following section to elucidate these behaviors.

6.3.3 Mass transport in images compared to low frequency measurements

The effects of mass transport in the microfluidic PEM electrolyzer were quantified in the previous section through DRT measurements from the lowest frequency EIS data. In this section, the anode and cathode channel wetnesses will be used as a global PEM hydration measurement for comparison over similar time scales. Of the 8 image sets acquired per cycle, the fifth to seventh images were considered for channel wetness calculations, as potentiostatic EIS sweeps were performed during the acquisition of these images. Recall the geometry of the electrolyzer as shown in *Fig. 6-8 a* and *b*. The wetness in each channel was determined for the two areas between the electrodes and PDMS channel separator (red bars in *Fig. 6-8c*), each with heights of 5 px and widths of 320 px (spanning the entire image). These regions were selected as H^+ ions must pass through these regions during electrochemical operation of the cell. A sample image with the areas of interest in red is shown in *Fig. 6-8c*. These respective areas were binarized through the DL thresholding method presented in *Appendix F*, such that wet pixels are assigned values of 1, and dry pixels are assigned values of 0. Then, the global wetness for the area of interest of each channel was determined by: (1) averaging over the height of the area of interest (5 px), (2) averaging over

the width of the entire image (320 px), (3) averaging for the images of interest (image 5-image 7 out of 8 images), and finally (4) averaging over the 250 frames with the chopper open. When considering other regions of interest for determining channel wetness percentage (i.e. in each corner of the image), none were suitable for investigation as there would be little to no electrolyte movement for some images, especially for higher electrolyte concentrations in the anode channel. This was attributed to the larger proximity from the channel separator or H^+ ion pathways, and results from those regions were random and inconsistent.

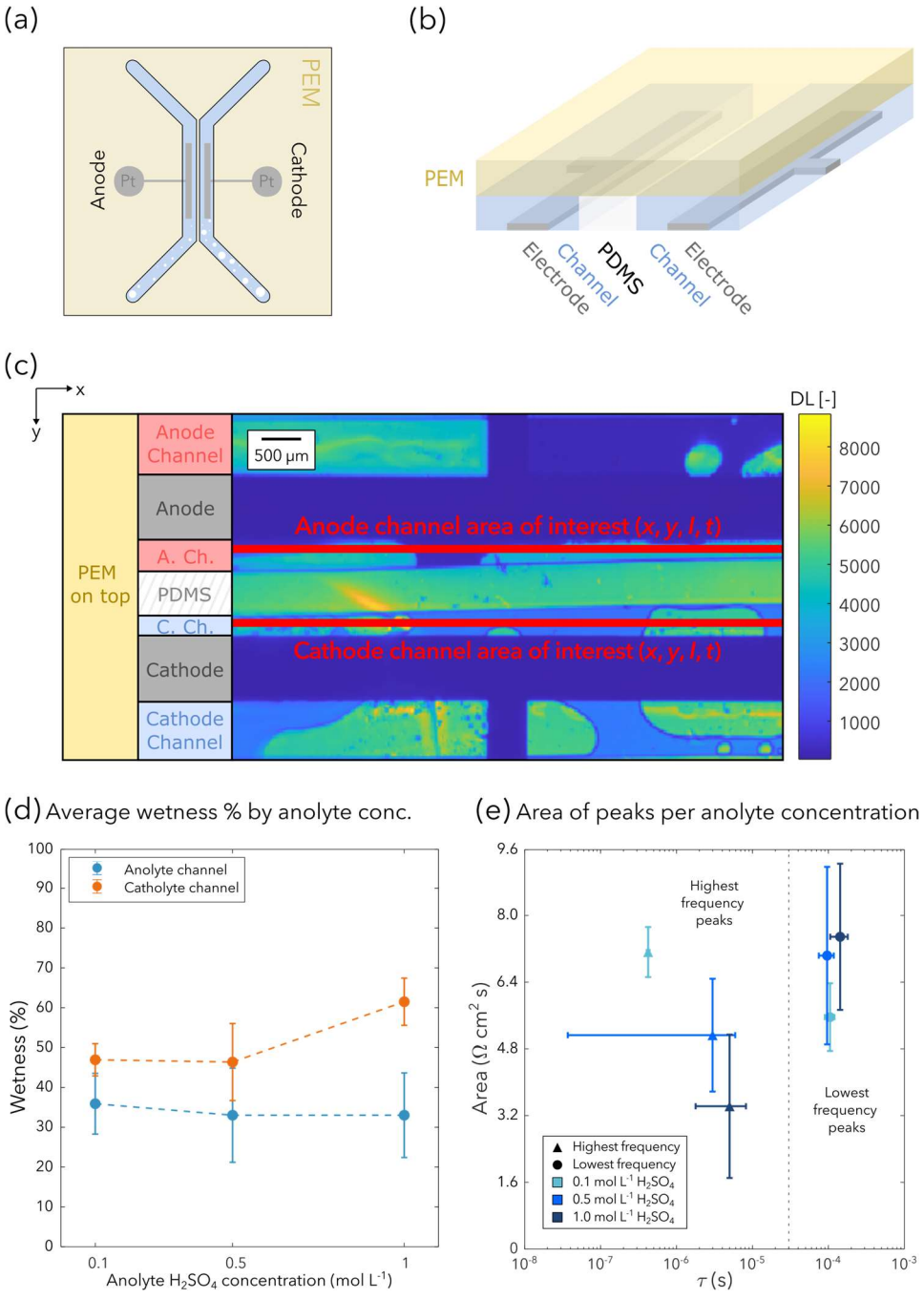

Fig. 6-8: (a) A 2D overhead view with (b) an isometric view of the cell geometry used to make the PEM electrolyzer. (c) A sample image of the PEM electrolyzer with areas of interest for the anode and cathode channels marked by the red box in between the respective electrode and the PDMS strip. (d) The averaged wetness percent for this area in images acquired during EIS measurements and the corresponding (e) area and time constants for the highest and lowest frequency peaks from the regularized DRT.

The wetness for the areas of interest (adjacent anode and cathode channels) are presented in *Fig. 6-8d* as an average of the 4 cycles for each anolyte concentration to compare to the corresponding lowest and highest frequency peaks (*Fig. 6-8e*). In *Fig. 6-8d*, the anolyte channel wetness is observed to remain relatively constant (35 % on average) for all anolyte concentrations. The increase in cathode wetness percentage (from 46.9 % ± 4.0 % to 61.5 % ± 5.9 % for 0.1 mol L^{-1} to 1.0 mol L^{-1} anolyte) is an interesting observation, especially when also considering the mass transport losses. For the intermediate anolyte concentration of 0.5 mol L^{-1} in *Fig. 6-8e*, the trend for low frequency peaks relative to mass transport is obscured due to the large error bars, but the area is larger and the frequency is lower for 1.0 mol L^{-1} anolyte in comparison to the 0.1 mol L^{-1} anolyte. While the magnitude of mass transport-associated phenomena is larger for the highest anolyte concentration, they also occur over a longer time period. Consequently, the increase in wetness percentage of the cathode channel could be associated with higher mass transport losses. The higher observed cathode wetness percentages could be attributed to excessive gas accumulation onto or poor gas removal from the cathode surface, which would thereby manifest as more water flowing around the electrode instead of over its surface.

6.3.3.1 Summary of global electrochemical and imaging results

Unfortunately, imaging the electrolyzer through this particular orientation is one of the technique's shortcomings, as the fraction of reactant water and product gas flowing across the electrode surface cannot be visualized. This is due to IR light being completely attenuated by the platinum electrodes, obscuring mass transport effects at electrode surfaces. Overall, during electrochemical operation of the microfluidic PEM electrolyzer presented here, a couple key phenomena were identified.

(1) With increasing anolyte concentration, electrochemical performance did not show any significant changes aside from an increase in the standard deviation in current density measurements.

A combination of DRT and EIS were employed to investigate the effect of each loss source (ohmic, activation/kinetic, and mass transport).

(2) The ohmic resistance of the electrolyzer slightly decreased with anolyte concentration, indicating that the increase in current density standard deviations were instead due to activation/kinetic and/or mass transport contributions. Correspondingly, DRT and EIS showed that activation/kinetic and mass transport losses were largest with the highest anolyte concentration.

Global imaging results presented as the adjacent channel wetness was compared to the increase in mass transport losses derived from the DRT.

(3) Only the cathode channel wetness was observed to show significant changes, which increased with mass transport losses, increased with anolyte concentration, and increased with the standard deviation in current density measurements.

Comparisons between electrochemical and imaging results were only compared to this extent for global measurements. However, investigating local regions through imaging may unveil the observed discrepancy in anode and cathode channel wetness for higher anolyte concentrations, which could manifest as visible water diffusion gradients across the PEM-PDMS strip between electrodes.

Peighambardoust et al. referred to two suggested water transport mechanisms in the PEM: (1) electro-osmotic drag and (2) concentration gradient driven diffusion, which can both be investigated through imaging.[106] Visualization of and then interpreting water gradients induced by either electro-osmotic drag from H^+ ion transport across the PEM or water diffusion across the membrane could be promising for elucidating membrane transport mechanisms in the PEM when given certain interfacial wetness conditions.

6.3.4 Segmenting images into local regions

Here, the membrane hydration in local regions of the same operating electrolyzer was visualized through processed images using combination of both raw and $\overline{\lambda_{H_2O}}$ image sets. Both image sets were used for analysis to investigate changes in membrane hydration (determined from $\overline{\lambda_{H_2O}}$ images) for local regions that contained different combinations of adjacent channel wetness/dryness (determined from raw images). Water transport in the electrolyzer was then

investigated for three characteristic regions (**wet**: anode and cathode channels both contain electrolyte, **dry**: anode and cathode channels both in absence of electrolyte, and **hybrid**: dry anode channel and wet cathode channel). In *Fig. 6-9a*, each component of the electrolyzer is shown for a sample raw image with three red boxes that represent the areas for each characteristic region. For this analysis, only one sample image was used (1.0 mol L^{-1} anolyte, cycle 1 image 7), for which the sample image was selected such that these three characteristic regions could be observed simultaneously. These same regions are labeled for the $\overline{\lambda_{H_2O}}$ image in *Fig. 6-9a*, where the water gradient in these characteristic regions was used to investigate PEM water transport mechanisms. $\overline{\lambda_{H_2O,a}}$ and $\overline{\lambda_{H_2O,c}}$ from *Eq. 6-6* will be considered at the y values in the red boxes from *Fig. 6-9 a* and *b* that are closest to the respective electrodes.

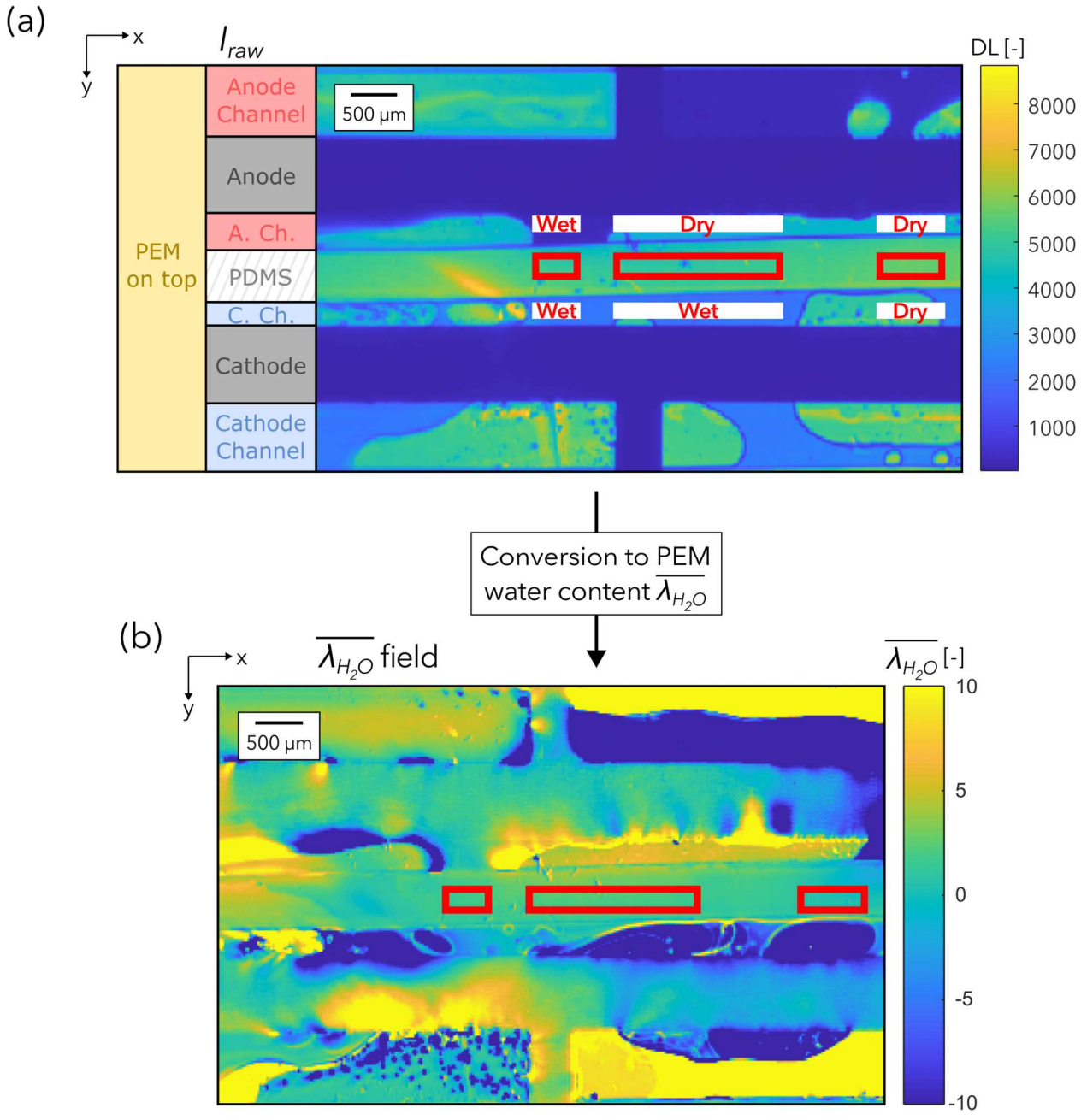

Fig. 6-9: (a) A corresponding sample image at cycle 1 with 1.0 mol L^{-1} anolyte with all cell components labeled on the left, and the three local regions that are denoted by red boxes were investigated. From left to right, first is the wet region, where the adjacent channels contain the electrolyte. Second is the hybrid region, where the immediately adjacent anode channel is dry while the adjacent cathode channel is wet. Third is the dry region, where both adjacent channels are dry. The (b) change in membrane hydration $\boldsymbol{\overline{\lambda_{H_2O}}}$ *is characterized for the red boxes that represent each of these regions.*

Each region was defined based on the wetness in the immediately adjacent channel (white box above/below red box in *Fig. 6-9a*). Specifically, the channel wetness was determined for pixels within the white boxes in *Fig. 6-9a*, which have the same length in the x-direction as each respective region and a height in the y-direction of 5 px. Each frame of the image stack is binarized and each pixel was converted into values of 0 for dry and 1 for wet based on a DL threshold. Specifically, a histogram of the DL for images was applied to the image, and the DLs for dry and wet pixels were compared. Details for the DL threshold binarization can be found in *Appendix F*. The wetness of each channel was then expressed as a percentage determined from the average of all pixels in the white box per frame, which was averaged again for all 250 frames with the chopper open.

Considering the experiment with 1.0 mol L^{-1} anolyte from cycle 1 image 7 and the specific regions in *Fig. 6-9 a* and *b*, the leftmost region has an anode channel wetness of 100 % and cathode channel wetness of 87.5 % and will be hereon referred to as the wet region. Next, the middle region has an anode channel wetness of 43.0 % and cathode channel wetness of 70.6 % and will be referred to as the hybrid region, and finally the rightmost region has an anode channel wetness of 0.3 % and a cathode wetness of 38.2 % and will be referred to as the dry region. Binarized images were averaged to visualize the movement of water in the adjacent channels where 0 corresponds to a dry channel and 1 corresponds to a wet channel. It is important to note that the influence of bubbles on the fluid dynamics in this particular electrolyzer are inefficient due to the morphology of the electrodes, and also because the cell was fabricated in absence of a porous transport layer. The smooth electrode surface combined with the lack of a porous transport layer causes low bubble contact angles that can complicate bubble removal.[15,195] The reported wetness percentages for each characteristic region may be strongly influenced by the lack of components/morphology for improving mass transport. The following section will investigate the sample image from the experiment with 1.0 mol L^{-1} anolyte, cycle 1 image 7, for which the images can be found in *Appendix G* (wetness percentages for each characteristic region were determined from these images).

6.3.5 Effect of local channel wetness on PEM hydration

With each region defined in the previous section, changes in membrane hydration ($\overline{\lambda_{H_2O}}$) will be investigated. In each region, $\overline{\lambda_{H_2O}}$ will be compared in terms of five evenly spaced columns and rows to observe how the adjacent channel wetness affects local PEM hydration. Each column of interest in the characteristic regions can be directly related to $\Delta\overline{\lambda_{H_2O}}$, as the columns of interest can represent the path of proton transport from the anode to cathode. However, particles/imaging artifacts that interfere with imaging may also affect the $\overline{\lambda_{H_2O}}$ profile of each column. $\Delta\overline{\lambda_{H_2O}}$ values would consequently be especially sensitive to noise from these artifacts because each characteristic region only has 10 px in the y-direction. To dampen the effect of these imaging artifacts, a linear trend is assumed for $\Delta\overline{\lambda_{H_2O}}$ changes over the y-direction of the region of interest, and is then fitted over the 10 px length in the y-direction. For any column of interest at a given x-position, the fitted change in membrane hydration across the y-direction (between the electrodes) can be defined:

$$\boldsymbol{\Delta\overline{\lambda_{fit}}(x) = a_1 x + a_0} \qquad \textit{Eq. 6-15}$$

where a_1 and a_0 are coefficients fitted for each column of interest which is shown in *Fig. 6-10b* as dotted fit-lines and the values for each coefficient is summarized in *Appendix G*. For each of the five rows of interest in the characteristic regions, the $\overline{\lambda_{H_2O}}$ profiles can be used to elaborate the effects of adjacent channel wetness in the direction of flow, and any biases in membrane hydration that may exist towards electrodes can be identified.

The wet region is shown in *Fig. 6-10a*, with the positions for five evenly spaced columns and rows of interest shown along the edge of the $\overline{\lambda_{H_2O}}$ field. The $\overline{\lambda_{H_2O}}$ profile for each line of interest was plotted in *Fig. 6-10b* for columns and *Fig. 6-10c* for rows. Considering the columns of interest, a slight increase in $\overline{\lambda_{H_2O}}$ can be seen in the direction of flow. As shown in *Tab. 6-3:* and *Fig. 6-10d*, the corresponding fitted values of $\Delta\overline{\lambda_{fit}}$ ranges from -0.23 to -0.089 and has an average value of -0.16, indicating a slight reduction in membrane hydration between the electrodes of the wet region from the reference state at OCV. However, each row of interest (*Fig. 6-10c*) increases in $\overline{\lambda_{H_2O}}$ from values around 1.4 to 2.0 in the direction of flow, regardless of the respective row's y-position. These changes in $\overline{\lambda_{H_2O}}$ indicate that when the adjacent channels contacting the PEM are wetted

and contain electrolyte, the membrane hydration will consequently increase in the direction of flow, without a bias towards either electrode.

Tab. 6-3: A compilation of all $\boldsymbol{\Delta\overline{\lambda_{fit}}}$ *values determined from each of the three characteristic regions. The same* $\boldsymbol{\Delta\overline{\lambda_{fit}}}$ *values for each characteristic region is shown in Fig. 6-10d, Fig. 6-11d, and Fig. 6-12d for the wet, hybrid, and dry regions, respectively. Values used to determine* $\boldsymbol{\Delta\overline{\lambda_{fit}}}$ *can be found in* **Appendix G**.

Column of interest	Wet region $\boldsymbol{\Delta\overline{\lambda_{fit}}}$	Hybrid region $\boldsymbol{\Delta\overline{\lambda_{fit}}}$	Dry region $\boldsymbol{\Delta\overline{\lambda_{fit}}}$
	-0.18	1.14	-0.10
	-0.095	0.88	-0.23
	-0.23	0.90	-0.51
	-0.22	0.83	-1.02
	-0.089	0.70	-1.04
Average	-0.16	0.89	-0.58

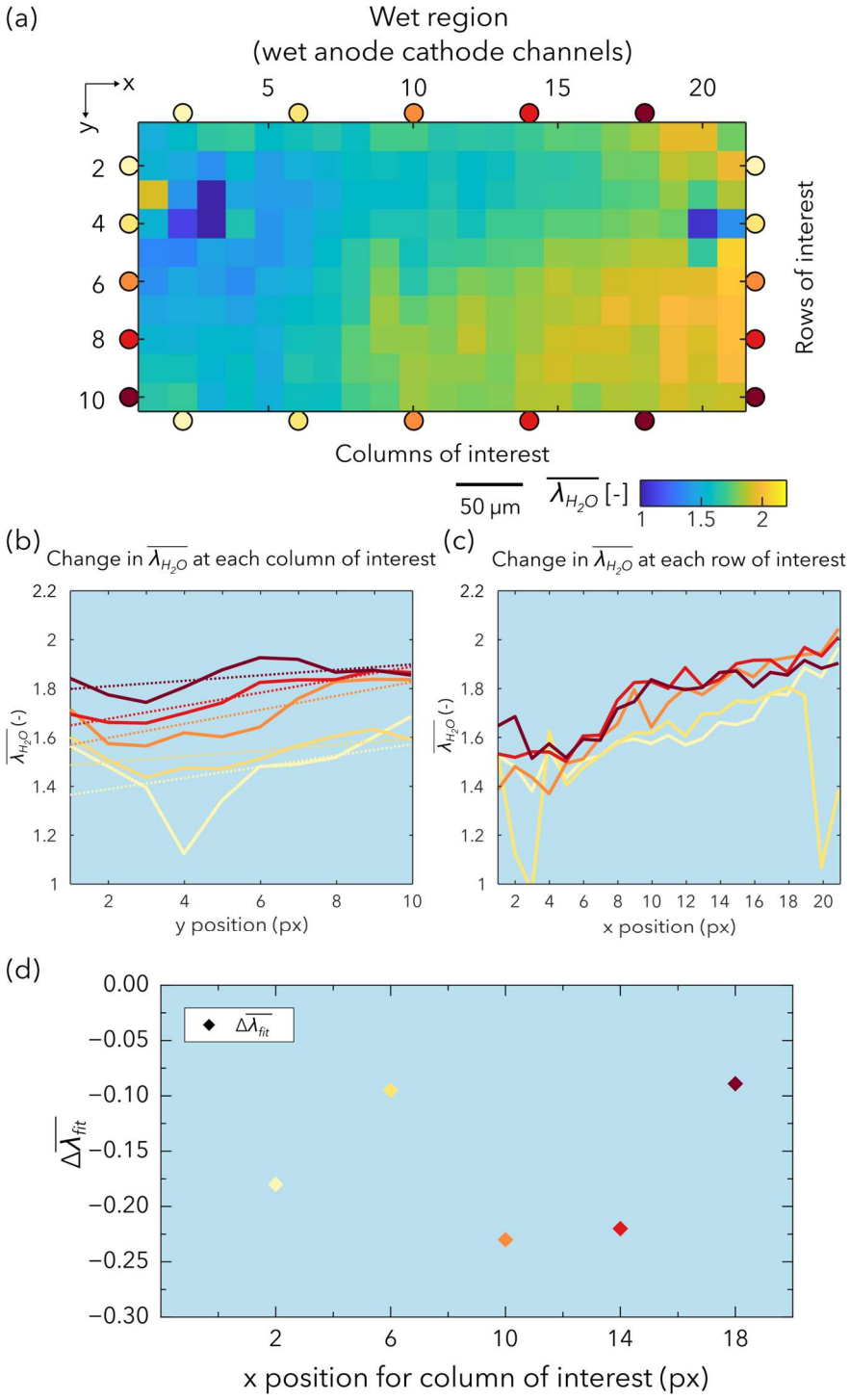

Fig. 6-10: (a) The wet region of interest with the change in membrane hydration for five (b) columns and (c) rows shown for the chip. Column and row positions are indicated by color on (a), which correspond to the plotted colors on (b) and (c). In (b), the profile of each column is fitted using Eq. 6-15 and the coefficients can be found in **Appendix G**. *(d) The* $\boldsymbol{\Delta\overline{\lambda_{fit}}}$ *values with respect to each column of interest in (b). The electrolytes flow from left to right.*

While the membrane hydration consistently increased along the direction of flow for the wet region, in the hybrid region, changes in membrane hydration for both $\overline{\lambda_{H_2O}}$ and $\Delta\overline{\lambda_{flt}}$ followed a different trend. The change in membrane hydration for the hybrid region is shown in *Fig. 6-11*. In this characteristic region, column data shows that $\overline{\lambda_{H_2O}}$ is highest on the anode side (y = 1, top of *Fig. 6-11a*) and lowest on the cathode side (y = 10, bottom of *Fig. 6-11b*), creating a water gradient from the anode to cathode that was alluded to in *Section 6.3.3*. The corresponding $\Delta\overline{\lambda_{flt}}$ values (shown in *Tab. 6-3* and *Fig. 6-11d*) have an average of 0.89 for the hybrid region, and in the direction of flow $\Delta\overline{\lambda_{flt}}$ decreased from 1.14 to 0.70. As the hybrid region immediately followed the wet region in the direction of flow (or by increasing x-position), the column with the smallest x-position in the hybrid region was expected to have the highest $\overline{\lambda_{H_2O}}$ values. Since the hybrid region is drier for both the anode (from 100.0 % to 43.0 % channel wetness) and cathode channels (from 87.5 % to 70.6 % channel wetness), the decreasing trend of $\overline{\lambda_{H_2O}}$ in the direction of flow was expected. Considering the rows of interest, the water gradient from the columns of interest could also be visualized, as the rows closest to the anode consistently have a higher $\overline{\lambda_{H_2O}}$ than those closest to the cathode side. Overall, the results from the hybrid region show higher PEM water uptake at the anode side from OCV, despite the anode channel wetness of 43.0 % being lower than the cathode channel wetness of 70.6 %. While the anode channel wetness is lower than that of the cathode, the change in PEM hydration was still higher on the anode side. This result supports the previous hypothesis (*Section 6.3.3*) of the higher mass transport losses being tied to the cathode for this anolyte concentration.

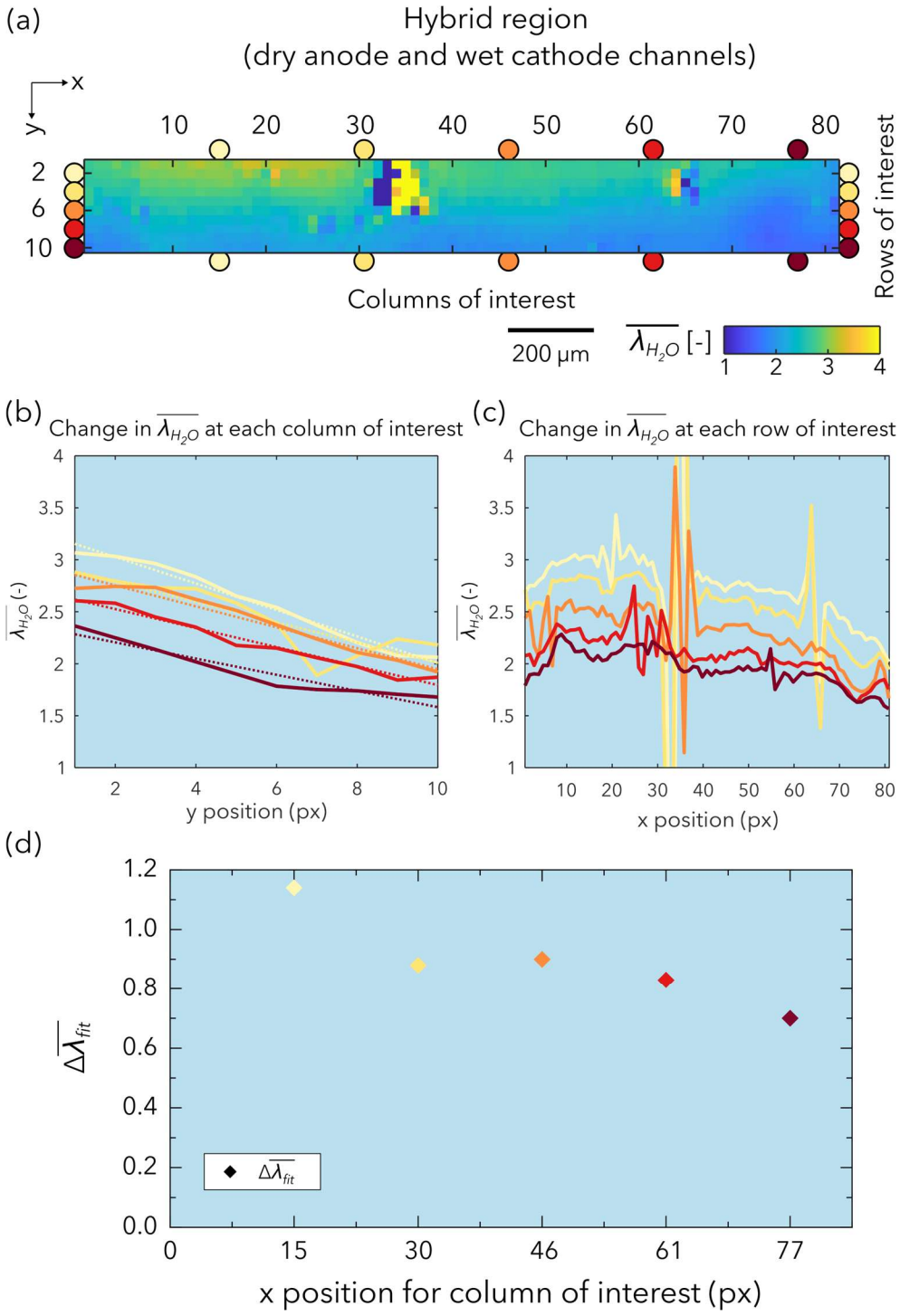

Fig. 6-11: (a) The hybrid region of interest with the change in membrane hydration for five (b) columns and (c) rows shown for the chip. Column and row positions are indicated by color on (a), which correspond to the plotted colors on (b) and (c). In (b), the profile of each column is fitted using Eq. 6-15 and the coefficients can be found in **Appendix G**. *(d) The* $\boldsymbol{\Delta\overline{\lambda_{fit}}}$ *values with respect to each column of interest in (b). The electrolytes flow from left to right.*

For the dry region, the PEM hydration was observed to decrease in both $\overline{\lambda_{H_2O}}$ and $\Delta\overline{\lambda_{flt}}$. In *Fig. 6-12a*, the dry region of the membrane is shown, where $\overline{\lambda_{H_2O}}$ gradients can again be observed both in the direction of flow (x-direction) and between the electrodes (y-direction). Considering the columns of interest in *Fig. 6-12b*, the dryness of the channel was observed in parallel with $\overline{\lambda_{H_2O}}$ becoming increasingly dry in the direction of flow. Specifically, the lightest colored columns have the highest $\overline{\lambda_{H_2O}}$ values and has the lowest $\Delta\overline{\lambda_{flt}}$ value of -0.10, indicating very little change from the reference state at OCV. As the columns of interest get darker in color, the $\overline{\lambda_{H_2O}}$ values decrease, in addition to reduced $\Delta\overline{\lambda_{flt}}$ values down to -1.04, as shown in *Tab. 6-3*. The average $\Delta\overline{\lambda_{flt}}$ value for the dry region was-0.58, and the clear reduction in $\Delta\overline{\lambda_{flt}}$ relative to the columns x-position can be observed in *Fig. 6-12d*. The reduction in both $\overline{\lambda_{H_2O}}$ and $\Delta\overline{\lambda_{flt}}$ indicate that the PEM is drying for the whole characteristic region, and at a faster rate at the anode side. Considering the rows of interest, all rows begin with roughly the same $\overline{\lambda_{H_2O}}$ value at 1, but the rows closest to the anode (top of *Fig. 6-12a*) dry the most while the rows closest to the cathode (bottom of *Fig. 6-12a*) dry the least, confirming the aforementioned hypothesis. The adjacent channel wetnesses also correspond to the observed preferential drying on the anode side, as the anode channel wetness is 0.3 %, while the cathode channel wetness is 38.2 %.

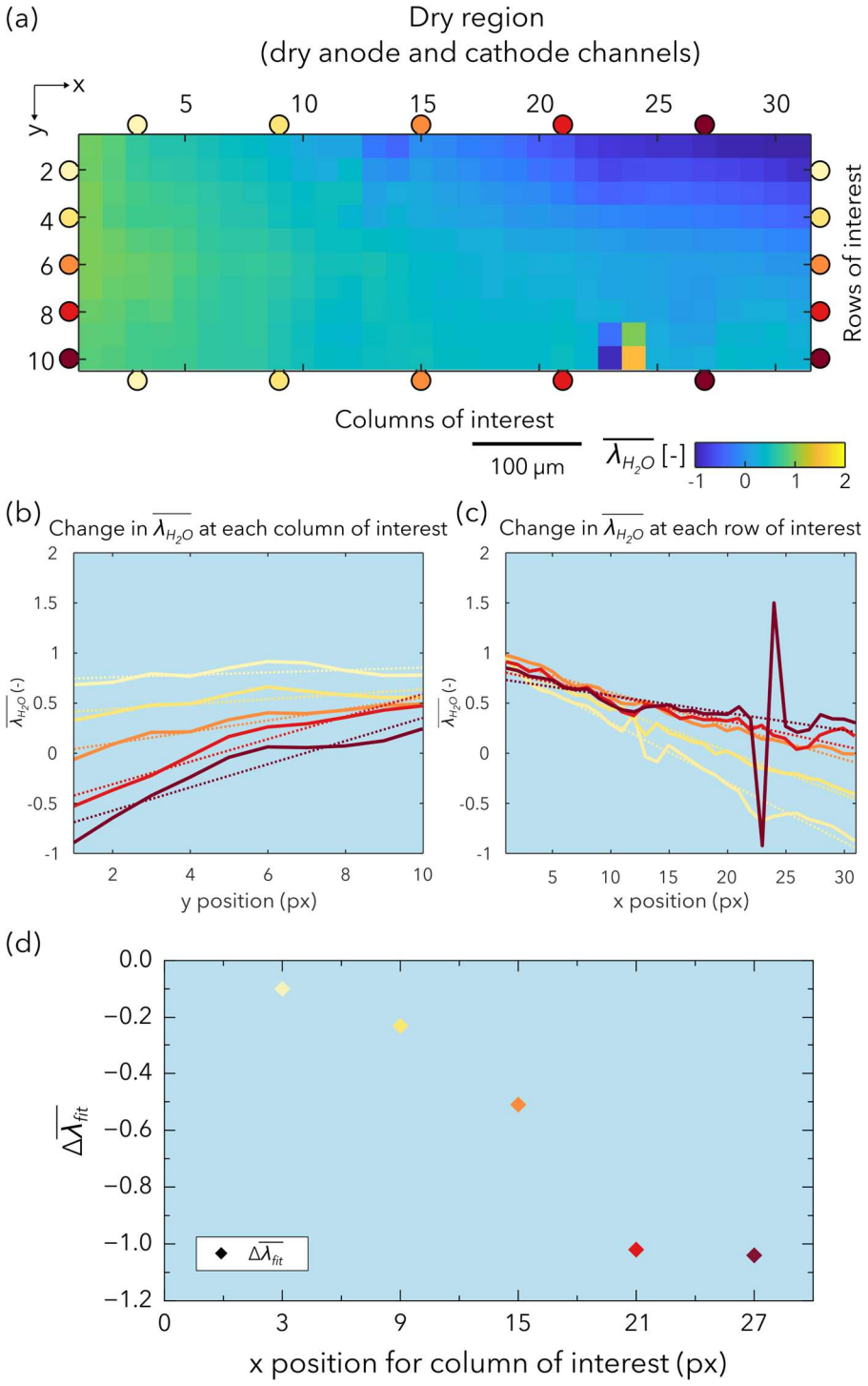

Fig. 6-12: (a) The dry region of interest with the change in membrane hydration for five (b) columns and (c) rows shown for the chip. Column and row positions are indicated by color on (a), which correspond to the plotted colors on (b) and (c). In (b), the profile of each column is fitted using Eq. 6-15 and the coefficients can be found in **Appendix G**. *(d) The* $\boldsymbol{\Delta\overline{\lambda_{fit}}}$ *values with respect to each column of interest in (b). The electrolytes flow from left to right.*

Overall, the three characteristic regions for the sample image taken (1.0 mol L^{-1}anolyte, cycle 1 image 7) were found to each affect the membrane hydration in unique ways, as shown in *Fig. 6-13a*. Considering the change in membrane hydration from OCV, $\overline{\lambda_{H_2O}}$ consistently increased in the direction of flow for the wet region (*Fig. 6-10b*). In the hybrid region, the highest $\overline{\lambda_{H_2O}}$ values were observed, with a higher PEM hydration towards the anode. However, outside of the channel splitter, the anode channel was drier than the cathode channel (43.0 % anode channel wetness vs. 70.6 % cathode channel wetness). The dry region had the lowest $\overline{\lambda_{H_2O}}$ values, where the adjacent cathode wetness was higher than the anode (38.2 % at the cathode vs. 0.3 % at the anode). The PEM correspondingly dried closer to the anode channel at a significantly faster rate than the region closer to the cathode.

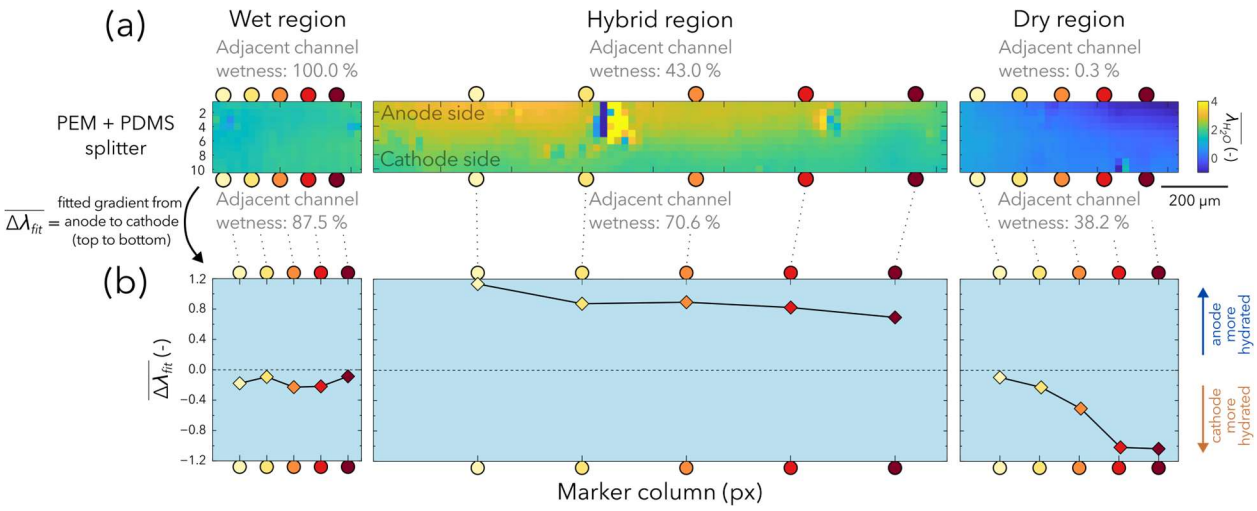

Fig. 6-13: (a) The PEM hydration field for each characteristic region of interest with reference to the hydration of the background acquired during OCV. (b) The gradient in PEM hydration from the anode to cathode. In the wet region, the PEM water distribution is even between channels. The hybrid region provokes a gradient in PEM water content that is higher and more hydrated on the anode side. The dry region provokes a gradient in PEM water content that is higher and more hydrated on the cathode side.

When considering $\Delta\overline{\lambda_{flt}}$ values for each region (*Tab. 6-3* and *Fig. 6-13b*): there is a negligible effect on $\Delta\overline{\lambda_{flt}}$ for the wet region (e.g. low average $\Delta\overline{\lambda_{flt}}$ value of -0.16), indicating that water was

distributed evenly within these areas of the PEM. The hybrid region has the largest observed $\Delta\overline{\lambda_{flt}}$ values with an average $\Delta\overline{\lambda_{flt}}$ of 0.89 indicating that the anode side of the PEM was more hydrated, and the dry region has the lowest observed $\Delta\overline{\lambda_{flt}}$ values with an average of -0.58 indicating that the cathode side of the PEM was more hydrated. These λ_{H_2O} values are the first reported for an operating electrolyzer through contactless imaging methods, and the first time operando imaging of a PEM electrolyzer has been performed using transmission IR techniques.

Recalling the work performed by He et al., they showed that mass transport at the surface of the PEM was qualitatively correlated to its fractional area for water entry.[96] Specifically, the wetness of the PEM's interface directly affects transport mechanisms through the bulk of the membrane. The local imaging data presented in this section cannot be discerned from electrochemical results from EIS or DRT due to the difference in acquisition time scales. However, our results may suggest that the PEM's water sorption increased as its interfacial and bulk resistance decreased. This currently cannot be verified through the results presented in this chapter; however, these results are still significant for elucidating the effects of local PEM hydration. The findings from this section prove the viability of using transmission IR techniques to characterize operating microfluidic PEM electrolyzers, as the water gradients in the PEM of an operating electrolyzer can be visualized. While a connection between channel wetness or PEM hydration to mass transport losses have not been identified at this point, this work confirms the need for even water distributions throughout the channels, especially when investigating hydration in the PEM. By improving upon the electrolyzer design used in this thesis, IR characterization of PEM electrolysis would bring us closer to visualizing water transport, and hopefully even ion transport through the PEM.

6.4 Chapter summary

In this chapter, the electrochemical performance and PEM wetness of a microfluidic water electrolyzer were evaluated using a combination of EIS, DRT, and IR spectroscopic imaging. The electrochemical performance of the microfluidic PEM electrolyzer was evaluated for three anolyte concentrations. These diagnostic tools enabled quantification of ohmic, activation/kinetic, and

mass transport losses. During electrochemical operation of the microfluidic PEM electrolyzer, a couple key phenomena were identified.

(1) With increasing anolyte concentration, electrochemical performance did not show any significant changes aside from an increase in the standard deviation in current density measurements.

DRT and EIS were both utilized to investigate the impact of loss sources (ohmic, activation/kinetic, and mass transport) on the performance of the electrolyzer.

(2) The ohmic resistance decreased with increasing anolyte concentration, indicating that the increase in current density standard deviations was instead due to activation/kinetic and/or mass transport contributions. DRT and EIS results showed that activation/kinetic and mass transport losses were largest with the highest anolyte concentration.

IR imaging results were then investigated relative to the adjacent channel wetness, and mass transport losses from the DRT were compared.

(3) The cathode channel wetness increased with increasing mass transport losses, anolyte concentration, and standard deviation in current density measurements. However, the anode channel wetness did not change significantly for each anolyte concentration. This phenomenon in combination with the higher mass transport losses measured through DRT and EIS implied that higher mass transport losses could be attributed to inefficient transport particularly in the cathode channel. This issue would likely be removed with the integration of PTLs during cell fabrication.

Local imaging results were studied to investigate the effect of local channel wetness on the PEM hydration. Different characteristic regions (wet, hybrid, and dry) were observed, each selected based on the wetness of the adjacent channels.

(4) Clear gradients between anode and cathode channels were visualized, enabling the first quantification of λ_{H_2O} fields via operando IR imaging.

(5) Water distribution through the PEM and its changes on the local and global scale showed the need for components such as PTLs to distribute water evenly within the

channels. Once a microfluidic PEM electrolyzer is developed with improved water distribution, the variables affecting λ_{H_2O} can be isolated and investigated more easily. Additionally, mass transport losses would be lower at the same conditions.

The results from this work can immediately be improved in the next design iteration with the inclusion of PTLs for improved water management in the channels. The microfluidic PEM electrolyzer and IR imaging setup were developed as a platform for characterization, for which we have effectively shown its potential through the measurement of PEM hydration during electrochemical operation. Integrating a porous hydrophilic component into the microfluidic electrolyzer fabrication will improve the quality of measurements and the cell architecture would better reflect the geometry of electrolyzers used in the industry. While the fabrication of a microfluidic chip integrating a PTL and a PEM simultaneously has yet to be achieved, the technology already exists as long as the proper instruments, laboratory equipment, and materials are used. Following the integration of PTLs for improved water management, other parameters such as the PEM thickness or the side-chain or backbone length of the PEM structure can be varied and then investigated through the techniques presented here. Moreover, the work presented in this chapter utilizes a beam that is filtered to be monochromatic. An appropriate experimental setup capable of polychromatic transmission IR imaging may be used to interpret changes in membrane chemistry during electrolyzer operation. If the recommended design changes can be integrated during cell fabrication, our understanding of both ion and water transport within PEMs of operating water electrolyzers may improve.

7 Conclusion

In this thesis, water transport within the membrane of PEM water electrolyzers was investigated through the combination of a microfluidics and operando IR spectroscopy. The development of the microfluidic PEM electrolyzer and its integration with the presented experimental setup was achieved through two parts. The contributions and key findings from each part and the chapters they are comprised of are summarized below.

In Part 1, the development of the microfluidic fabrication method, the experimental setup, and the image processing routines were achieved. Part 1 was comprised of Chapter 2 and Chapter 3. In Chapter 2, a brief overview of microfluidic applications and their potential in combination with transmission IR characterization techniques was presented. The material considerations necessary for the fabrication of a microfluidic chip were detailed. The working principles of the relevant IR techniques (FTIR spectroscopy and thermography) were introduced as well as their associated image processing methods.

In Chapter 3, a microfluidic chip that was semi-transparent in IR light was developed for characterization using the mid-wave IR spectrum. In this microfluidic chip, mass and heat transfer were quantified through FTIR spectroscopy and IR thermography, respectively, for two exothermic acid-base reactions. Experimental results were compared to an advection-diffusion numerical simulation made to reproduce the microfluidic chip used in this study. Mass transfer was visualized for each of these reactions through the segmented concentration gradients of each chemical species (e.g. acid, base, and the product salt) and for three flow rates. Heat transfer was visualized for each of these reactions through thermal fields, where the heat produced from each of the reactions was most clearly visualized at the reaction interface. The experimental mass and heat transfer results for one reaction were cross-validated to the numerical simulation and a strong agreement between the two datasets was found. The study showed the potential in coupling microfluidic chips with IR techniques, establishing the necessary techniques for the fabrication of a microfluidic PEM electrolyzer and its integration with IR spectroscopy.

Part 2 begins with Chapter 4, where a literature review of transport mechanisms through the PEM was conducted to present the relevant background for the remaining works in this thesis. Chapter

5 and Chapter 6 build the remaining sections of Part 2, and involve the fabrication and characterization of the microfluidic PEM electrolyzer.

In Chapter 5, the first microfluidic PEM water electrolyzer that is semi-transparent in the IR domain for characterization transmission IR spectroscopy was developed. Its membrane hydration was evaluated for two failure mechanisms driven by the supplied reactant flow rate through operando synchrotron FTIR spectroscopy. The lower flow rate drove mass transport-dominated overpotentials up to current densities of 75 mA cm^{-2}, when membrane drying was observed immediately before cell failure. The higher flow rate drove ohmic-dominated overpotentials and sustained improved current densities of up to 225 mA cm^{-2} that were comparable to similar microfluidic PEM electrolysis architectures presented in the literature, with the caveat that this chip was specifically designed to be semi-transparent in IR. The study acted as a first step for resolving water transport at a local region in the PEM of operating electrolyzers using transmission IR techniques.

In Chapter 6, the same microfluidic chip architecture fabricated in the previous chapter was evaluated with a wider range of characterization tools to improve our understanding of water transport in the PEM during electrochemical operation. The chip was characterized using EIS, DRT, and an in house IR spectroscopic imaging setup. The current response of the chip was measured through potentiostatic operation at 2.5 V for three different anolyte concentrations. Higher anolyte concentrations were accompanied by larger standard deviations in current density measurements. The characterization tools unveiled that while higher anolyte concentrations were accompanied by reduced ohmic losses, they were also accompanied by higher kinetic and mass transport losses. The PEM water content was averaged for acquired IR images to compare global PEM water content with the electrochemical performance under comparable time scales. The global PEM water content in images was investigated from low to high anolyte concentrations, for which the cathode channel wetness increased as well as mass transport losses. These results implied higher mass transport losses that could be attributed to inefficient product removal from the cathode. To investigate these effects further, the PEM hydration was investigated in three characteristic regions defined by the wetness of the adjacent channels: dry, wet, and hybrid (a mix of dry and wet). Water transport through the membrane was quantified through the term λ_{H_2O}, which was then used to determine water gradients between the electrodes $\Delta\overline{\lambda_{H_2O}}$. These results

were the first utilizing transmission based IR imaging to visualize the effects of the wetness of adjacent channels on the PEM hydration.

This thesis advances towards the understanding of water transport in PEMs through the fabrication of a microfluidic PEM electrolyzer for characterization through transmission IR techniques. The fabrication methods and experimental setup used here can be extended by implementing porous layers into the microfluidic electrolyzers, which could be refined to accurately measure water transport and maybe eventually the measurement of phenomena such as electro-osmotic drag or even the rarely reported thermo-osmosis. Additionally, the methods presented here could be extended for the characterization of other membrane types (e.g. bipolar- or anion exchange-membranes) that are commonly used in other electrochemical configurations. This microfluidic electrolyzer currently achieves current density operation one order of magnitude less than that of conventional electrolyzers. If comparable performance can be achieved in this chip through the integration of state-of-the-art components, then experimental results would more accurately reflect results from the larger scale industrial electrolyzers.

8 Future works

While the development of a microfluidic polymer electrolyte membrane (PEM) water electrolyzer that is semi-transparent in infrared (IR) light was completed in this thesis, there are some potential shortcomings in the presented works that must be investigated. For example, the impact of the utilized fabrication methods on electrolyzer longevity and performance must be evaluated. As a result, the following future works are recommended based on the findings presented in this thesis.

8.1 The effect of polymer electrolyte membrane pre-expansion via per-fluorinated resin on electrochemical performance

Membrane expansion and shrinking was a challenging hurdle that needed to be overcome for the fabrication of the microfluidic PEM electrolyzer used in Chapter 5 and Chapter 6. To reduce the mechanical effects of membrane expansion and shrinking during fabrication, the PEM was pre-swelled with Nafion resin before applying chemical bonding techniques. While this technique enabled IR imaging of PEM hydration, it is unconventional and may be detrimental to the electrolyzer's performance. Therefore, the effects of membrane pre-swelling through a per-fluorinated resin must be evaluated.

These effects can be investigated in a typical PEM water electrolysis cell with neutron imaging and can be combined with the other electrochemical characterization tools presented in this work (e.g. electrochemical impedance spectroscopy (EIS) and distribution of relaxation times (DRT)). Operating the electrolyzer during simultaneous neutron imaging is recommended for two electrolyzer builds. First is the control PEM electrolyzer case, using a PEM electrolyzer built with conventional components (e.g. titanium flow fields, porous transport layers (PTLs), and a catalyst coated membrane (CCM)). For the second case, the PEM electrolyzer should be built and tested through the same methods, but be built with the CCM pre-expanded through a per-fluorinated resin. The obtained electrochemical results (from potentiostatic or galvanostatic operation, EIS, and DRT) can then be compared with results obtained during neutron imaging to elucidate the physical and electrochemical effects of PEM pre-expansion. These results would inform of the validity of this technique for future transmission IR characterization using the presented cell architecture.

8.2 Integrating state-of-the-art water electrolysis components into microfluidic polymer electrolyte membrane electrolyzers for operando infrared spectroscopic imaging

One of the shortcomings of the fabrication methods for the microfluidic electrolyzer that resulted was the lack of state-of-the-art components. Specifically, the simultaneous integration of PTLs and CCMs in the fabrication of the microfluidic electrolyzer, which has yet to be achieved. Local liquid and gas measurements manifested in the dry and hybrid characteristic regions that were investigated in *Section 6.3.5*. However, the dry characteristic regions were undesirable as insufficient membrane hydration was observed around those regions. The integration of PTLs to improve water management in the chip would greatly improve uniform PEM hydration within the microfluidic PEM electrolyzer. Consequently the quality of results obtained in acquired IR images with the presented cell architecture could be improved. The fabrication of a microfluidic electrolyzer with an implemented PTL and a PEM has already been achieved for each material independently, and simply integrating a hydrophilic mesh layer would improve the water distribution throughout the channel.

In addition to the inclusion of PTLs and different PEM configurations in the fabrication process, the PEM and platinum electrodes can be replaced with a custom-ordered CCM with strategically placed catalysts. The catalysts would be deposited on one surface of the CCM and be separated such that they could be electrically separated. Fabricating a similar but improved microfluidic PEM electrolyzer with an integrated CCM would directly reduce ohmic losses as ions would not have to conduct through a liquid electrolyte. Effective water management in the microfluidic PEM electrolyzer through the integration of PTLs and CCMs would not just reduce the ohmic losses through a shorter path of ion transport, but would also reduce the interfacial resistance of the membrane.[65] The integration of PTLs and CCMs may also improve the quality of measured PEM water content (λ_{H_2O}) in comparison to those reported in Chapter 6.

8.3 Changes to membrane chemistry in an operating polymer electrolyte membrane water electrolyzer captured via multispectral infrared imaging

Only one type of membrane (Aquivion, Solvay) was investigated through the transmission-based IR techniques presented in Chapter 5 and Chapter 6. PEMs vary in many parameters, such as their thickness, their condition, their equivalent weights, the length of their backbone side chains, etc., and these parameters are all known to affect transport through the PEM.[65] For example, PEMs manufactured with chemical backbone structures containing shorter side chains such as Aquivion have shorter relaxation times than PEMs that are made with longer side chains such as Nafion. Moreover, these effects vary relative to the hydration of the PEM, as water transport in PEMs is influenced by the acidity and mobility of the sulfonic acid groups that the water molecules transport or conduct protons through.[83] Therefore, investigating various PEMs (e.g. varied equivalent weights, different molecular compositions, thicknesses, etc.) integrated into the microfluidic architecture presented in this thesis – especially those with fewer differences between parameters – are recommended. Additionally, the effects of membrane aging when utilized in this configuration are unknown and the chemistry of the PEM can be elucidated with transmission IR imaging. However, if the electrolyzer fabricated here is unsuitable for repeated use through accumulated mechanical stress (e.g. through membrane swelling and shrinking), pursuing another electrolyzer architecture is recommended.

The effects of these parameters on water transport through PEMs would be elucidated when combined with the IR characterization setup presented here. The IR characterization tools can even be improved to more sensitive instruments that are capable of multispectral IR imaging, which may enable the capture of changes in membrane chemistry during electrolyzer operation. Future improvement of fabrication and IR characterization of these materials may eventually enable the quantification of proton transport relative to the electrolyzer's electrochemical performance and its PEM hydration.

References

1 J. Hansen, P. Kharecha, M. Sato, V. Masson-Delmotte, F. Ackerman, D. J. Beerling, P. J. Hearty, O. Hoegh-Guldberg, S. L. Hsu, C. Parmesan, J. Rockstrom, E. J. Rohling, J. Sachs, P. Smith, K. Steffen, L. Van Susteren, K. Von Schuckmann and J. C. Zachos, *PLoS One*, , DOI:10.1371/journal.pone.0081648.

2 EIA projects world energy consumption will increase 56% by 2040, https://www.eia.gov/todayinenergy/detail.php?id=12251, (accessed 30 November 2023).

3 O. M. Toledo, D. Oliveira Filho and A. S. A. C. Diniz, *Renew. Sustain. Energy Rev.*, 2010, **14**, 506–511.

4 A. A. Kebede, T. Kalogiannis, J. Van Mierlo and M. Berecibar, *Renew. Sustain. Energy Rev.*, 2022, **159**, 112213.

5 P. M. Falcone, M. Hiete and A. Sapio, *Curr. Opin. Green Sustain. Chem.*, 2021, **31**, 100506.

6 J. O. Abe, A. P. I. Popoola, E. Ajenifuja and O. M. Popoola, *Int. J. Hydrogen Energy*, 2019, **44**, 15072–15086.

7 G. Gahleitner, *Int. J. Hydrogen Energy*, 2013, **38**, 2039–2061.

8 O. Schmidt, A. Gambhir, I. Staffell, A. Hawkes, J. Nelson and S. Few, *Int. J. Hydrogen Energy*, 2017, **42**, 30470–30492.

9 M. Carmo, D. L. Fritz, J. Mergel and D. Stolten, *Int. J. Hydrogen Energy*, 2013, **38**, 4901–4934.

10 P. Millet, F. Andolfatto and R. Durand, *Int. J. Hydrogen Energy*, 1996, **21**, 87–93.

11 P. Millet, *Hydrogen production by polymer electrolyte membrane water electrolysis*, Elsevier Ltd, 2015, vol. 1.

12 F. Marangio, M. Santarelli and M. Calì, *Int. J. Hydrogen Energy*, 2009, **34**, 1143–1158.

13 P. Choi, D. G. Bessarabov and R. Datta, *Solid State Ionics*, 2004, **175**, 535–539.

14 J. K. Lee and A. Bazylak, *Joule*, 2021, **5**, 19–21.

15 A. Angulo, P. van der Linde, H. Gardeniers, M. Modestino and D. Fernández Rivas, *Joule*, 2020, **4**, 555–579.

16 W. T. Grubb, *J. Phys. Chem.*, 1959, **63**, 55–58.

17 W. T. Grubb, *J. Electrochem. Soc.*, 1959, **106**, 275.

18 F. Arbabi, A. Kalantarian, R. Abouatallah, R. Wang, J. Wallace and A. Bazylak, *ECS Trans.*, 2013, **58**, 907–918.

19 O. Panchenko, E. Borgardt, W. Zwaygardt, F. J. Hackemüller, M. Bram, N. Kardjilov, T. Arlt, I. Manke, M. Müller, D. Stolten and W. Lehnert, *J. Power Sources*, 2018, **390**, 108–115.

20 C. Lee, J. K. Lee, B. Zhao, K. F. Fahy and A. Bazylak, *J. Electrochem. Soc.*, 2020, **167**, 024508.

21 F. Arbabi, A. Kalantarian, R. Abouatallah, R. Wang, J. S. Wallace and A. Bazylak, *J. Power Sources*, 2014, **258**, 142–149.

22 Y. A. Song, C. Batista, R. Sarpeshkar and J. Han, *J. Power Sources*, 2008, **183**, 674–677.

23 W. Y. Lin, Y. Wang, S. Wang and H. R. Tseng, *Nano Today*, 2009, **4**, 470–481.

24 A. W. Chow, *AIChE J.*, 2002, **48**, 1590–1595.

25 T. Bayraktar and S. B. Pidugu, *Int. J. Heat Mass Transf.*, 2006, **49**, 815–824.

26 H. A. Stone, A. D. Stroock and A. Ajdari, *Annu. Rev. Fluid Mech.*, 2004, **36**, 381–411.

27 H. Gao, C. Yan, W. Wu and J. Li, *Food Funct.*, 2020, **11**, 5726–5737.

28 A. G. Niculescu, C. Chircov, A. C. Bîrcă and A. M. Grumezescu, *Int. J. Mol. Sci.*, 2021, **22**, 1–26.

29 A. Centrone, *Annu. Rev. Anal. Chem.*, 2015, **8**, 101–126.
30 A. Perro, G. Lebourdon, S. Henry, S. Lecomte, L. Servant and S. Marre, *React. Chem. Eng.*, 2016, **1**, 577–594.
31 C. Pradere, M. Joanicot, J. C. Batsale, J. Toutain and C. Gourdon, *Quant. Infrared Thermogr. J.*, 2006, **3**, 117–135.
32 C. Berthomieu and R. Hienerwadel, *Photosynth. Res.*, 2009, **101**, 157–170.
33 G. Ghosh, *Handbook of Thermo-Optic Coefficients of Optical Materials with Applications*, 1998, vol. 5.
34 C. J. Glassbrenner and G. A. Slack, *Phys. Rev.*, 1964, **134**, 1058–1069.
35 C. Caliendo and F. Lo Castro, *Advanced bulk and thin film materials for harsh environment MEMS applications*, Elsevier Ltd, 2014.
36 D. G. Harville and D. L. Freeman, *SPE Annu. Tech. Conf. Exhib. 2-5 October, Houston, Texas*, 1988, 141–151.
37 L. Mertz, *Appl. Opt.*, 1983, **22**, 1535.
38 J. Morikawa, E. Hayakawa, T. Hashimoto, R. Buividas and S. Juodkazis, *Opt. Express*, 2011, **19**, 20542.
39 M. Ryu, J. A. Kimber, T. Sato, R. Nakatani, T. Hayakawa, M. Romano, C. Pradere, A. A. Hovhannisyan, S. G. Kazarian and J. Morikawa, *Chem. Eng. J.*, 2017, **324**, 259–265.
40 G. M. Carlomagno and G. Cardone, *Infrared thermography for convective heat transfer measurements*, 2010, vol. 49.
41 R. Usamentiaga, P. Venegas, J. Guerediaga, L. Vega, J. Molleda and F. G. Bulnes, *Sensors (Switzerland)*, 2014, **14**, 12305–12348.
42 T. Lafargue-Tallet, R. Vaucelle, C. Caliot, A. Aouali, E. Abisset-Chavanne, A. Sommier, R. Peiffer and C. Pradere, *Sci. Rep.*, 2022, **12**, 1–19.
43 Notus Computational Fluid Dynamics code, https://notus-cfd.org/.
44 D. W. James, *J. Mater. Sci.*, 1968, **3**, 540–543.
45 K. Hirota, 1941, **16**, 475–484.
46 J. A. Rard and D. G. Miller, *J. Solution Chem.*
47 K. I. Miyamoto, H. Ichimura, T. Wagner, M. J. Schöning and T. Yoshinobu, *Sensors Actuators, B Chem.*, 2013, **189**, 240–245.
48 L. J. P. Timmermans, P. D. Minev and F. N. Van De Vosse, *Int. J. Numer. Methods Fluids*, 1996, **22**, 673–688.
49 H. Charles, *Numerical Computation of Internal and External Flows, Volume 2: Computational Methods for Inviscid and Viscous Flows*, 1990, vol. 2.
50 R. D. Falgout, J. E. Jones and U. M. Yang, *Lect. Notes Comput. Sci. Eng.*, 2006, **51**, 267–294.
51 J. Paterson, D. Singhal, D. Tainoff, J. Richard and O. Bourgeois, *J. Appl. Phys.*, , DOI:10.1063/5.0004576.
52 M. W. J. Chase, *NIST-JANAF Themochemical Tables*, Fourth., 1998, vol. Monograph.
53 J. Wei, M. Liao, A. Ma, Y. Chen, Z. Duan, X. Hou, M. Li, N. Jiang and J. Yu, *Compos. Commun.*, 2020, **17**, 141–146.
54 M. L. Huber, R. A. Perkins, M. J. Assael, S. A. Monogenidou, R. Hellmann and J. V. Sengers, *J. Phys. Chem. Ref. Data*, , DOI:10.1063/5.0084222.
55 A. Aouali, S. Chevalier, A. Sommier, E. Abisset-Chavanne, J. C. Batsale and C. Pradere, *Sci. Rep.*, 2020, **10**, 1–10.
56 C. Bourges, S. Chevalier, J. Maire, A. Sommier, C. Pradere and S. Dilhaire, 2022, 1–16.
57 L. J. Nuttall and J. H. Russell, *Int. J. Hydrogen Energy*, 1980, **5**, 75–84.

58 K. Schmidt-Rohr and Q. Chen, *Nat. Mater.*, 2008, **7**, 75–83.
59 K. A. Mauritz and R. B. Moore, *Chem. Rev.*, 2004, **104**, 4535–4585.
60 Y. Lin, T. Arlt, N. Kardjilov, I. Manke and W. Lehnert, *Energies*, , DOI:10.3390/en11092214.
61 T. D. Gierke, G. E. Munn and F. C. Wilson, *J. Polym. Sci. Part A-2, Polym. Phys.*, 1981, **19**, 1687–1704.
62 J. Chi and H. Yu, *Cuihua Xuebao/Chinese J. Catal.*, 2018, **39**, 390–394.
63 M. M. Rashid, M. K. Al Mesfer, H. Naseem and M. Danish, *Int. J. Eng. Adv. Technol.*, 2015, 2249–8958.
64 S. Shiva Kumar and V. Himabindu, *Mater. Sci. Energy Technol.*, 2019, **2**, 442–454.
65 A. Kusoglu and A. Z. Weber, *Chem. Rev.*, 2017, **117**, 987–1104.
66 S. Slade, S. A. Campbell, T. R. Ralph and F. C. Walsh, *J. Electrochem. Soc.*, 2002, **149**, A1556.
67 P. Medina and M. Santarelli, *Int. J. Hydrogen Energy*, 2010, **35**, 5173–5186.
68 F. Barbir, *PEM Fuel Cells: Theory and Practice*, Academic Press, 2nd edn., 2012.
69 K. D. Kreuer, *Solid State Ionics*, 2013, **252**, 93–101.
70 A. Kusoglu, A. Hexemer, R. Jiang, C. S. Gittleman and A. Z. Weber, *J. Memb. Sci.*, 2012, **421**–**422**, 283–291.
71 M. K. Budinski and A. Cook, *Tsinghua Sci. Technol.*, 2010, **15**, 385–390.
72 Y. Zhang, J. Li, L. Ma, W. Cai and H. Cheng, *Energy Technol.*, 2015, **3**, 675–691.
73 M. Clapp, C. M. Zalitis and M. Ryan, *Catal. Today*, 2023, **420**, 114140.
74 N. J. Herkert, J. Merrill, C. Peters, D. Bollinger, S. Zhang, K. Hoffman, P. L. Ferguson, D. R. U. Knappe and H. M. Stapleton, *Environ. Sci. Technol. Lett.*, 2020, **7**, 178–184.
75 X. Dauchy, *Curr. Opin. Environ. Sci. Heal.*, 2019, **7**, 8–12.
76 E. S. Coffin, D. M. Reeves and D. P. Cassidy, *Curr. Opin. Environ. Sci. Heal.*, 2023, **31**, 100418.
77 Y. Li, G. He, S. Wang, S. Yu, F. Pan, H. Wu and Z. Jiang, *J. Mater. Chem. A*, 2013, **1**, 10058–10077.
78 J. Li, W. Cai, Y. Zhang and H. Cheng, *Energy Technol.*, 2014, **2**, 685–691.
79 S. Matsumura, A. R. Hlil, C. Lepiller, J. Gaudet, D. Guay, Z. Shi, S. Holdcroft and A. S. Hay, *Am. Chem. Soc. Polym. Prepr. Div. Polym. Chem.*, 2008, **49**, 511–512.
80 M. J. Park, K. H. Downing, A. Jackson, E. D. Gomez, A. M. Minor, D. Cookson, A. Z. Weber and N. P. Balsara, *Nano Lett.*, 2007, **7**, 3547–3552.
81 T. E. Springer, T. A. Zawodzinski and S. Gottesfeld, *J. Electrochem. Soc.*, 1991, **138**, 2334.
82 K. D. Kreuer, M. Schuster, B. Obliers, O. Diat, U. Traub, A. Fuchs, U. Klock, S. J. Paddison and J. Maier, *J. Power Sources*, 2008, **178**, 499–509.
83 D. K. Lee, T. Saito, A. J. Benesi, M. A. Hickner and H. R. Allcock, *J. Phys. Chem. B*, 2011, **115**, 776–783.
84 A. Kusoglu, T. J. Dursch and A. Z. Weber, *Adv. Funct. Mater.*, 2016, **26**, 4961–4975.
85 R. B. Moore and C. R. Martin, *Macromolecules*, 1989, **22**, 3594–3599.
86 L. Maldonado, J. C. Perrin, J. Dillet and O. Lottin, *J. Memb. Sci.*, 2012, **389**, 43–56.
87 J. Wang, M. Yang, P. Dou, X. Wang and H. Zhang, *Ind. Eng. Chem. Res.*, 2014, **53**, 14175–14182.
88 F. M. Collette, C. Lorentz, G. Gebel and F. Thominette, *J. Memb. Sci.*, 2009, **330**, 21–29.
89 F. D. Coms, T. J. Fuller and C. P. Schaffer, *J. Electrochem. Soc.*, 2018, **165**, F3104–F3110.
90 A. Kusoglu, B. L. Kienitz and A. Z. Weber, *J. Electrochem. Soc.*, 2011, **158**, B1504.
91 D. Wu, S. J. Paddison, J. A. Elliott and S. J. Hamrock, *Langmuir*, 2010, **26**, 14308–14315.

92 G. Dorenbos and Y. Suga, *J. Memb. Sci.*, 2009, **330**, 5–20.
93 B. S. Pivovar, *Polymer (Guildf).*, 2006, **47**, 4194–4202.
94 K. Chadha, S. Martemianov and A. Thomas, *Fuel Cells*, 2021, **21**, 139–148.
95 W. Z. Lang, H. Y. Niu, Y. X. Liu, C. X. Liu and Y. J. Guo, *J. Appl. Polym. Sci.*, 2013, **129**, 3473–3481.
96 Q. He, A. Kusoglu, I. T. Lucas, K. Clark, A. Z. Weber and R. Kostecki, *J. Phys. Chem. B*, 2011, **115**, 11650–11657.
97 C. Chen and T. F. Fuller, *J. Electrochem. Soc.*, 2009, **156**, B1218.
98 G. S. Hwang, D. Y. Parkinson, A. Kusoglu, A. A. MacDowell and A. Z. Weber, *ACS Macro Lett.*, 2013, **2**, 288–291.
99 C. E. Evans, R. D. Noble, S. Nazeri-Thompson, B. Nazeri and C. A. Koval, *J. Memb. Sci.*, 2006, **279**, 521–528.
100 L. M. Onishi, J. M. Prausnitz and J. Newman, 2007, 10166–10173.
101 T. A. Zawodzinski, C. Derouin, S. Radzinski, R. J. Sherman, V. T. Smith, T. E. Springer and S. Gottesfeld, *J. Electrochem. Soc.*, 1993, **140**, 1041–1047.
102 P. Choi and R. Datta, *ACS Div. Fuel Chem. Prepr.*, 2003, **48**, 300–301.
103 J. P. G. Villaluenga, B. Seoane, V. M. Barragán and C. Ruiz-Bauzá, *J. Memb. Sci.*, 2006, **274**, 116–122.
104 M. N. Tsampas, A. Pikos, S. Brosda, A. Katsaounis and C. G. Vayenas, *Electrochim. Acta*, 2006, **51**, 2743–2755.
105 J. Lin, P. H. Wu, P. N. Pintauro, R. Wycisk and Z. Shi, *AIChE Annu. Meet. Conf. Proc.*, 2008, **117**, 4284–4289.
106 S. J. Peighambardoust, S. Rowshanzamir and M. Amjadi, *Review of the proton exchange membranes for fuel cell applications*, Elsevier Ltd, 2010, vol. 35.
107 K. D. Kreuer, *Chem. Mater.*, 1996, **8**, 610–641.
108 K. A. Page, B. W. Rowe, K. A. Masser and A. Faraone, *J. Polym. Sci. Part B Polym. Phys.*, 2014, **52**, 624–632.
109 N. Agmon, *Chem. Phys. Lett.*, 1995, **244**, 456–462.
110 S. Kim and M. M. Mench, *J. Memb. Sci.*, 2009, **328**, 113–120.
111 M. Giacinti Baschetti, M. Minelli, J. Catalano and G. C. Sarti, *Int. J. Hydrogen Energy*, 2013, **38**, 11973–11982.
112 T. Sakai, H. Takenaka and E. Torikai, *J. Electrochem. Soc.*, 1986, **133**, 88–92.
113 H. S. Sodaye, P. K. Pujari, A. Goswami and S. B. Manohar, *J. Polym. Sci. Part B Polym. Phys.*, 1998, **36**, 983–989.
114 M. Schalenbach, T. Hoefner, P. Paciok, M. Carmo, W. Lueke and D. Stolten, *J. Phys. Chem.*
115 H. F. M. Mohamed, K. Ito, Y. Kobayashi, N. Takimoto, Y. Takeoka and A. Ohira, *Polymer (Guildf).*, 2008, **49**, 3091–3097.
116 H. F. M. Mohamed, Y. Kobayashi, C. S. Kuroda and A. Ohira, *J. Phys. Chem. B*, 2009, **113**, 2247–2252.
117 S. Siracusano, S. Trocino, N. Briguglio, V. Baglio and A. S. Aricò, *Materials (Basel).*, , DOI:10.3390/ma11081368.
118 P. Millet, N. Mbemba, S. A. Grigoriev, V. N. Fateev, A. Aukauloo and C. Etiévant, *Int. J. Hydrogen Energy*, 2011, **36**, 4134–4142.
119 K. Elsøe, L. Grahl-Madsen, G. G. Scherer, J. Hjelm and M. B. Mogensen, *J. Electrochem. Soc.*, 2017, **164**, F1419–F1426.
120 P. J. Kim, J. K. Lee, C. H. Lee, K. F. Fahy, P. Shrestha, K. Krause, H. W. Shafaque and A. Bazylak, *Electrochim. Acta*, , DOI:10.1016/j.electacta.2021.137879.

121 M. Suermann, T. J. Schmidt and F. N. Büchi, *ECS Meet. Abstr.*, 2015, **MA2015-02**, 1517–1517.
122 C. H. Lee, J. K. Lee, M. G. George, K. F. Fahy, J. M. LaManna, E. Baltic, D. S. Hussey, D. L. Jacobson and A. Bazylak, *Energy Convers. Manag.*, 2020, **213**, 112797.
123 A. Lasia, *Electrochemical Impedance Spectroscopy and its Applications*, 2014.
124 Y. Li, Y. Jiang, J. Dang, X. Deng, B. Liu, J. Ma, F. Yang, M. Ouyang and X. Shen, *Chem. Eng. J.*, 2023, **451**, 138327.
125 S. M. R. Niya and M. Hoorfar, *Electrochim. Acta*, 2014, **120**, 193–203.
126 S. Chevalier, N. Ge, J. Lee, M. G. George, H. Liu, P. Shrestha, D. Muirhead, N. Lavielle, B. D. Hatton and A. Bazylak, *J. Power Sources*, 2017, **352**, 281–290.
127 M. Ise, K. D. Kreuer and J. Maier, *Solid State Ionics*, 1999, **125**, 213–223.
128 X. Gong, A. Bandis, A. Tao, G. Meresi, Y. Wang, P. T. Inglefield, A. A. Jones and W. Y. Wen, *Polymer (Guildf).*, 2001, **42**, 6485–6492.
129 A. Guillermo, G. Gebel, H. Mendil-Jakani and E. Pinton, *J. Phys. Chem. B*, 2009, **113**, 6710–6717.
130 M. Maalouf, C. N. Sun, B. Pyle, M. Emery, G. M. Haugen, S. J. Hamrock and T. A. Zawodzinski, *Int. J. Hydrogen Energy*, 2014, **39**, 2795–2800.
131 T. Suzuki, Y. Tabuchi, S. Tsushima and S. Hirai, *Int. J. Hydrogen Energy*, 2011, **36**, 5479–5486.
132 P. M. Mangiagli, C. S. Ewing, K. Xu, Q. Wang and M. A. Hickner, *Fuel Cells*, 2009, **9**, 432–438.
133 D. J. Burnett, A. R. Garcia and F. Thielmann, *J. Power Sources*, 2006, **160**, 426–430.
134 R. O'Hayre, M. Lee and F. B. Prinz, *J. Appl. Phys.*, 2004, **95**, 8382–8392.
135 D. A. Bussian, J. R. O'Dea, H. Metiu and S. K. Buratto, *Nano Lett.*, 2007, **7**, 227–232.
136 S. Deabate, P. Huguet, A. Morin, G. Gebel, Y. Lanteri, Z. Peng and A. K. Sutor, *Fuel Cells*, 2014, **14**, 677–693.
137 A. Z. Peng, A. Morin, P. Huguet, Y. Lanteri and S. Deabate, *Phys. Chem. Chem. Phys.*, 2014, **16**, 20941–20956.
138 S. Deabate, R. Fatnassi, P. Sistat and P. Huguet, 2008, **176**, 39–45.
139 Y. Tabuchi, R. Ito, S. Tsushima and S. Hirai, *J. Power Sources*, 2011, **196**, 652–658.
140 T. A. Zawodzinski, M. Neeman, L. O. Sillerud and S. Gottesfeld, *J. Phys. Chem.*, 1991, **95**, 6040–6044.
141 M. Hara, J. Inukai, K. Miyatake, H. Uchida and M. Watanabe, *Electrochim. Acta*, 2011, **58**, 449–455.
142 M. F. L'Annunziata, *Radioactivity*, 2007, 1–45.
143 D. Reilly, N. Ensslin and H. J. Smith, *Passive Nondestructive Assay of Nuclear Materials*, 1991, vol. 5.
144 R. Banerjee, N. Ge, C. Han, J. Lee, M. G. George, H. Liu, D. Muirhead, P. Shrestha and A. Bazylak, *Int. J. Hydrogen Energy*, 2018, **43**, 9757–9769.
145 A. K. C. Wong, N. Ge, P. Shrestha, H. Liu, K. Fahy and A. Bazylak, *Appl. Energy*, 2019, **240**, 549–560.
146 N. Ge, R. Banerjee, D. Muirhead, J. Lee, H. Liu, P. Shrestha, A. K. C. Wong, J. Jankovic, M. Tam, D. Susac, J. Stumper and A. Bazylak, *J. Power Sources*, 2019, **422**, 163–174.
147 M. A. Hickner, N. P. Siegel, K. S. Chen, D. S. Hussey, D. L. Jacobson and M. Arif, *J. Electrochem. Soc.*, 2008, **155**, B427.
148 P. Quan, M. C. Lai, D. S. Hussey, D. L. Jacobson, A. Kumar and S. Hirano, *J. Fuel Cell Sci. Technol.*, 2010, **7**, 0510091–0510096.

149 A. Morin, F. Xu, G. Gebel and O. Diat, *Int. J. Hydrogen Energy*, 2011, **36**, 3096–3109.
150 E. Leonard, A. D. Shum, S. Normile, D. C. Sabarirajan, D. G. Yared, X. Xiao and I. V. Zenyuk, *Electrochim. Acta*, 2018, **276**, 424–433.
151 E. Leonard, A. D. Shum, N. Danilovic, C. Capuano, K. E. Ayers, L. M. Pant, A. Z. Weber, X. Xiao, D. Y. Parkinson and I. V. Zenyuk, *Sustain. Energy Fuels*, 2020, **4**, 921–931.
152 P. Shrestha, J. M. Lamanna, K. F. Fahy, P. Kim, C. Lee, J. K. Lee, E. Baltic, D. L. Jacobson, D. S. Hussey and A. Bazylak, , DOI:10.1126/sciadv.adg8634.
153 M. Maier, J. Dodwell, R. Ziesche, C. Tan, T. Heenan, J. Majasan, N. Kardjilov, H. Markötter, I. Manke, L. Castanheira, G. Hinds, P. R. Shearing and D. J. L. Brett, *J. Power Sources*, , DOI:10.1016/j.jpowsour.2020.227968.
154 C. Korzeneewski, E. Adams and D. Liu, *Appl. Spectrosc.*, 2008, **62**, 634–639.
155 J. Ostrowska and A. Narebska, *Colloid Polym. Sci.*, 1983, **261**, 93–98.
156 M. Falk, *Can. J. Chem.*, 1980, **58**, 1495–1501.
157 R. M. Blanchard and R. G. Nuzzo, *J. Polym. Sci. Part B Polym. Phys.*, 2000, **38**, 1512–1520.
158 T. Shimoaka, C. Wakai, T. Sakabe, S. Yamazaki and T. Hasegawa, *Phys. Chem. Chem. Phys.*, 2015, **17**, 8843–8849.
159 A. D. O. Bawagan, S. J. Hamrock, M. Schaberg, I. Yousef, E. Ritter and U. Schade, *Vib. Spectrosc.*, 2014, **75**, 213–217.
160 S. Matsumura, A. R. Hlil, C. Lepiller, J. Gaudet, D. Guay, Z. Shi, S. Holdcroft and A. S. Hay, *J. Polym. Sci. Part A Polym. Chem.*, 2008, **46**, 7207–7224.
161 D. T. Hallinan and Y. A. Elabd, *J. Phys. Chem. B*, 2009, **113**, 4257–4266.
162 D. T. Hallinan, M. G. De Angelis, M. Giacinti Baschetti, G. C. Sarti and Y. A. Elabd, *Macromolecules*, 2010, **43**, 4667–4678.
163 T. J. Zimudzi and M. A. Hickner, *ACS Macro Lett.*, 2016, **5**, 83–87.
164 H. R. Zelsmann, M. Pineri, M. Thomas and M. Escoubes, *J. Appl. Polym. Sci.*, 1990, **41**, 1673–1684.
165 S. R. Lowry and K. A. Mauritz, *J. Am. Chem. Soc.*, 1980, **102**, 4665–4667.
166 Solvay, Aquivion ® E87-05S perfluorosulfonic acid, https://www.fuelcellstore.com/spec-sheets/solvay-aquivion-e87-05s-membrane.pdf.
167 M. H. Pham and D. P. J. Barz, *J. Memb. Sci.*, 2017, **537**, 310–314.
168 Sarah Klug, 2021, 1–6.
169 F. Kodera, Y. Kuwahara, A. Nakazawa and M. Umeda, *J. Power Sources*, 2007, **172**, 698–703.
170 R. Attias, B. Dlugatch, M. S. Chae, Y. Goffer and D. Aurbach, *Electrochem. commun.*, 2021, **124**, 106952.
171 G. M. Hale and M. R. Querry, *Appl. Opt.*, 1973, **12**, 555.
172 M. N. Polyanskiy, Refractive index database, https://refractiveindex.info, (accessed 29 June 2023).
173 M. Watanabe, H. Uchida, Y. Seki, M. Emori and P. Stonehart, *J. Electrochem. Soc.*, 1996, **143**, 3847–3852.
174 M. A. Modestino, C. A. Diaz-Botia, S. Haussener, R. Gomez-Sjoberg, J. W. Ager and R. A. Segalman, *Phys. Chem. Chem. Phys.*, 2013, **15**, 7050–7054.
175 M. A. Modestino, M. Dumortier, S. M. Hosseini Hashemi, S. Haussener, C. Moser and D. Psaltis, *Lab Chip*, 2015, **15**, 2287–2296.
176 C. Immerz, B. Bensmann, P. Trinke, M. Suermann and R. Hanke-Rauschenbach, *J. Electrochem. Soc.*, 2018, **165**, F1292–F1299.

177 A. Z. Weber, R. L. Borup, R. M. Darling, P. K. Das, T. J. Dursch, W. Gu, D. Harvey, A. Kusoglu, S. Litster, M. M. Mench, R. Mukundan, J. P. Owejan, J. G. Pharoah, M. Secanell and I. V. Zenyuk, *J. Electrochem. Soc.*, 2014, **161**, F1254–F1299.
178 S. Ge, B. Yi and P. Ming, *J. Electrochem. Soc.*, 2006, **153**, A1443.
179 H. Ito, T. Maeda, A. Nakano and H. Takenaka, *Int. J. Hydrogen Energy*, 2011, **36**, 10527–10540.
180 T. A. Zawodzinski, T. E. Springer, J. Davey, R. Jestel, C. Lopez, J. Valerio and S. Gottesfeld, *J. Electrochem. Soc.*, 1993, **140**, 1981–1985.
181 The Engineering Toolbox, Viscosity - Absolute (Dynamic) vs. Kinematic., https://www.engineeringtoolbox.com/dynamic-absolute-kinematic-viscosity-d_412.html, (accessed 20 October 2023).
182 P. A. Kempler, Z. P. Ifkovits, W. Yu, A. I. Carim and N. S. Lewis, *Energy Environ. Sci.*, 2021, **14**, 414–423.
183 *Mater. Saf. Data Sheet*, 2018, **77**, 1–8.
184 *Mater. Saf. Data Sheet*, 2017, **77**, 1–8.
185 *Mater. Saf. Data Sheet*, 2018, **77**, 1–8.
186 T. A. Zawodzinski, J. Davey, J. Valerio and S. Gottesfeld, *Electrochim. Acta*, 1995, **40**, 297–302.
187 A. Z. Weber and J. Newman, *J. Electrochem. Soc.*, 2003, **150**, A1008.
188 T. Paul, P. W. Chi, P. M. Wu and M. K. Wu, *Sci. Rep.*, 2021, **11**, 1–9.
189 BioLogic, Distribution of Relaxation Times (DRT): how to identify equivalent circuits efficiently - BioLogic Learninc Center, https://www.biologic.net/topics/distribution-of-relaxation-times-drt-how-to-identify-equivalent-circuits-efficiently/, (accessed 20 October 2023).
190 A. Crête-Laurence, 2023, 1–49.
191 K. A. Woodbury, Ed., *Inverse Engineering Handbook*, CRC Press, 2002.
192 J. Staser, R. P. Ramasamy, P. Sivasubramanian and J. W. Weidner, *Electrochem. Solid-State Lett.*, 2007, **10**, 17–19.
193 C. W. Sun and S. S. Hsiau, *J. Electrochem. Sci. Technol.*, 2018, **9**, 99–108.
194 H. E. Darling, *J. Chem. Eng. Data*, 1964, **9**, 421–426.
195 C. H. Lee, J. Hinebaugh, R. Banerjee, S. Chevalier, R. Abouatallah, R. Wang and A. Bazylak, *Int. J. Hydrogen Energy*, 2017, **42**, 2724–2735.
196 D. Kirkham, 2016.

Appendix

Appendix A: Temperature control through the PID controller

The temperature of the microfluidic chips were controlled and monitored through a copper thermistor that was connected to a proportional integral-derivative (PID) controller. The thermistor is flat ring shaped with 35 mm inner diameter and 50.8 mm outer diameter and has a thickness of 0.38 mm (*Fig. A-**1***).

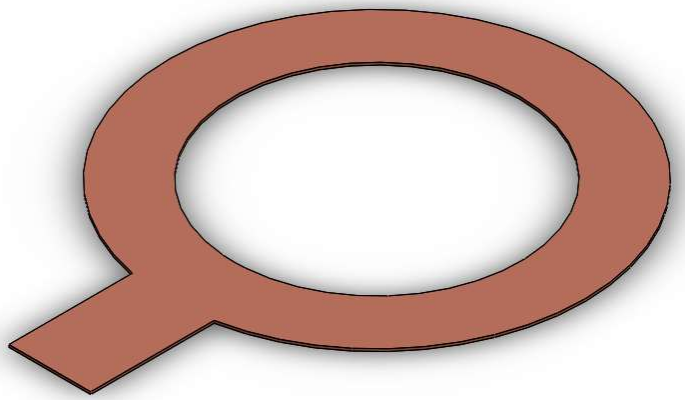

Fig. A-1: A model of the thermistor used to deliver temperature to microfluidic chips.

The thermistor has a coppered side on a nickel probe that is glued onto an insulated kapton surface. The copper surface was used to deliver temperature efficiently to a microfluidic chip (placed directly onto the copper surface). The resistance of the thermistor rated by the vendor Captec, was given as:

$$\boldsymbol{R_H = 11.0\ \Omega} \qquad \textit{Eq. A-1}$$

$$\boldsymbol{R_N = 31.52 \times (1 + 0.00610\,T)} \qquad \textit{Eq. A-2}$$

where R_H is the heater electrical resistance, R_N is the nickel probe electrical resistance [Ω], and T is the temperature [°C].

A PID was used to heat the copper thermistor, for which the basic working principles will be introduced here. PID control involves the PID controller itself, the system (object under control, the thermistor in this case), and an actuation device (power supply in this case) to drive the system. Initially, a set point, in terms of temperature (°C), is given to the PID controller, which will deliver a control signal in terms of voltage to the power supply. The voltage is determined through Ohm's Law where the resistance is the sum of those in *Eq. A-**1*** and *Eq. A-**2***. The power supply then delivers the voltage to the thermistor. The temperature of the thermistor is concurrently measured by its sensor probe, and its temperature is sent back to the PID controller as feedback. The PID controller will then adjust the control signal accordingly, and repeatedly loop between the PID controller, power supply, and thermistor. This closed feedback loop is shown below in *Fig. A-**2***.

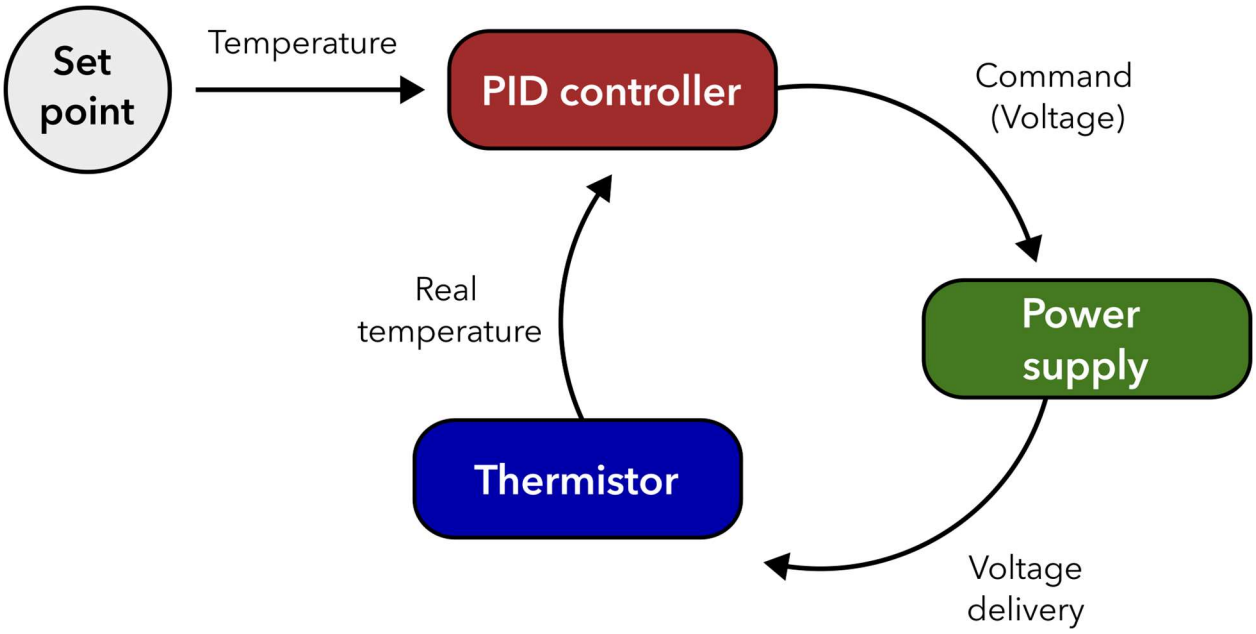

Fig. A-2: The closed feedback loop of the PID to regulate the temperature to the thermistor.

The command [V] or control signal that is delivered from the PID controller is determined as the sum of the three components of the PID, which it is named after.

$$\boldsymbol{Command = P + I + D} \qquad \textit{Eq. A-3}$$

First is the proportional term $\boldsymbol{P}$:

$$\boldsymbol{P = K_p e(t) = K_p(SP - PV)} \qquad \textit{Eq. A-4}$$

where $\boldsymbol{K_p}$ is the gain for the proportional term, $\boldsymbol{e(t)}$ is the error value which is the difference between the set point ($\boldsymbol{SP}$) [°C] and the measured process variable ($\boldsymbol{PV}$, temperature in this case) [°C]. Second is the integral term which is proportional to the time ($\boldsymbol{t}$) integral of the error value:

$$\boldsymbol{I = K_i \cdot \int_0^t (SP - PV) dt} \qquad \textit{Eq. A-5}$$

where $\boldsymbol{K_i}$ is the gain of the integral term. Finally the derivative term uses the difference between the current and previous error values divided by the time differential between measurements ($\boldsymbol{dt}$).

$$\boldsymbol{D = K_d \cdot \frac{d}{dt}(SP - PV)} \qquad \textit{Eq. A-6}$$

Appendix B: Beam size at the Far-IR beamline of the Canadian Light Source

The beam diameter is determined by assuming a Gaussian beam and performing a knife-edge measurement. By using the interface in the channel of the chip and the edge of the electrodes, a sharp edge representing a knife-edge can be obtained for the necessary measurements. The methodology for determining the beam size analysis is performed by Kirkham and is replicated here.[196] The final beam radius is determined to be 45.62 ± 0.48 µm for a wavelength of 10.7 µm.

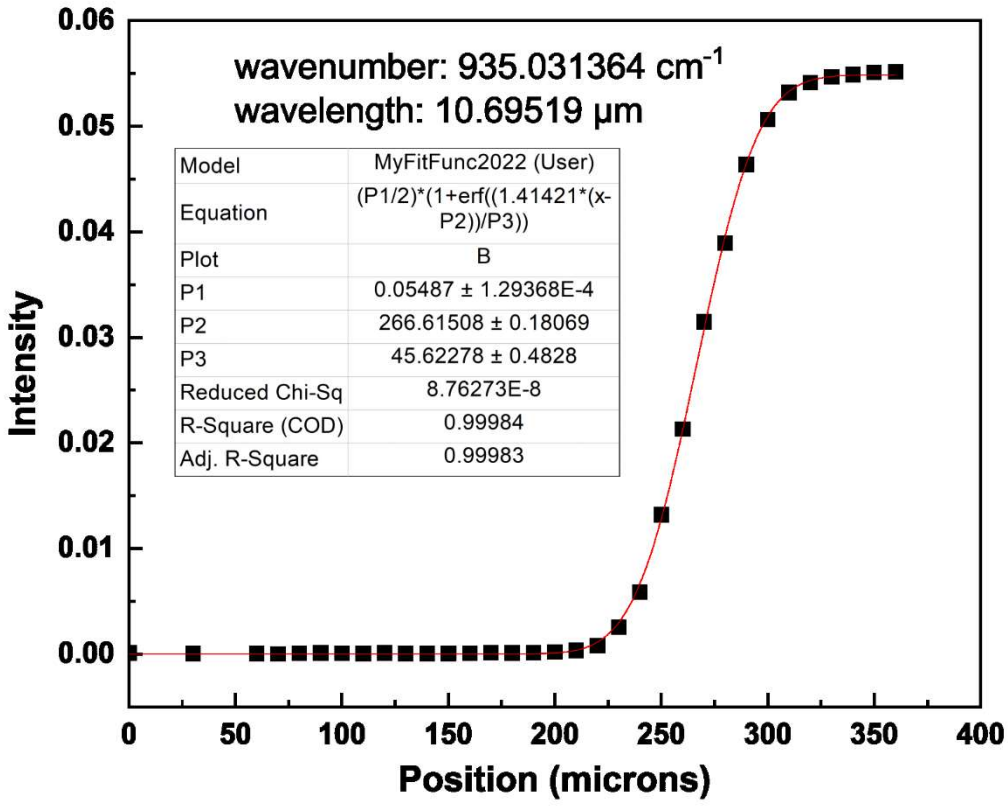

Fig. B-1: The resulting error function plot with fitting parameters P1, P2, and P3 for a wavelength of 10.7 µm. P3 corresponds to $1/e^2$ radius of the Gaussian beam, where the calculated beam radius is 45.62278 ± 0.4828 µm.

Appendix C: Raw infrared spectra

The raw IR transmission spectra acquired during FTIR spectroscopy were cropped around the peak of interest. The peak of interest is roughly centered around a wavelength of 10.7 μm and is the only observable peak in the measured spectrum where water attenuated the beam. The IR spectra are averaged for 300 acquisitions with a spectral resolution of 4 cm^{-1}. Each acquisition is measured during the final two minutes of steady current operation and results are presented for all experimental conditions.

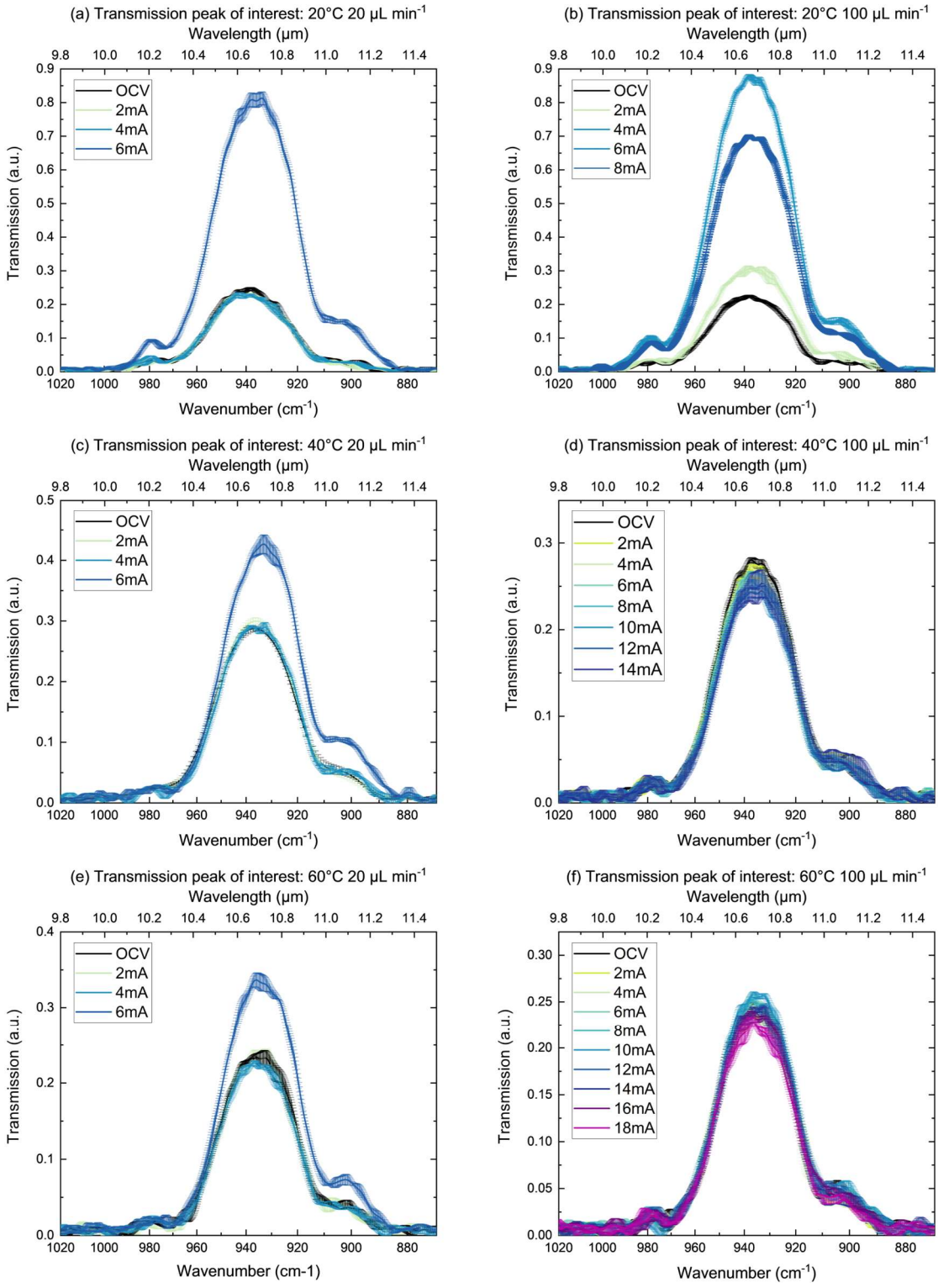

Fig. C-1: Averaged IR spectra from 300 acquisitions for each constant current operating condition for (a) 20 °C, 20 µL min^{-1}, (b) 20 °C, 100 µL min^{-1}, (c) 40 °C, 20 µL min^{-1}, (d) 40 °C, 100 µL min^{-1}, (e) 60 °C, 20 µL min^{-1}, and (f) 60 °C, 100 µL min^{-1}.

Appendix D: Ohmic resistance of the microfluidic PEM electrolyzer

Ohmic resistance measurements extracted from EIS were challenging to obtain for the proposed cell geometry due to the small active area of 0.08 cm^2. To improve the accuracy of ohmic resistance measurements, an impedance model from the work presented by Chevalier et al. was applied onto the experimentally obtained Nyquist plots, and the ohmic resistance was extracted as the HFR of the model.[126] A sample Nyquist plot with the fitted model is shown in *Fig. D-**1***.

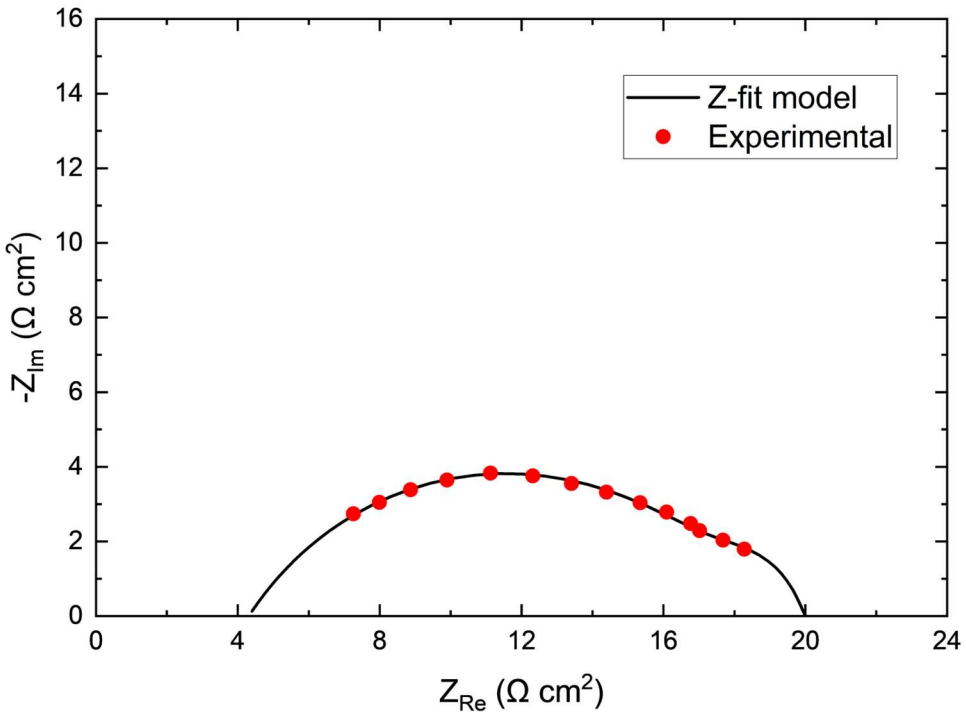

Fig. D-1: A sample Nyquist plot with the corresponding Z-fit model obtained at 20 °C with a flow rate of 20 µL min^{-1} and at a current density of 30 mA cm^{-2}. The extracted ohmic resistance is 4.31 Ω cm^2.

Individual ohmic resistance measurements and the corresponding ohmic voltage losses are graphically reported in *Fig. D-**2*** for each operating condition. Ohmic voltage losses are computed through *Eq. **1-8***.

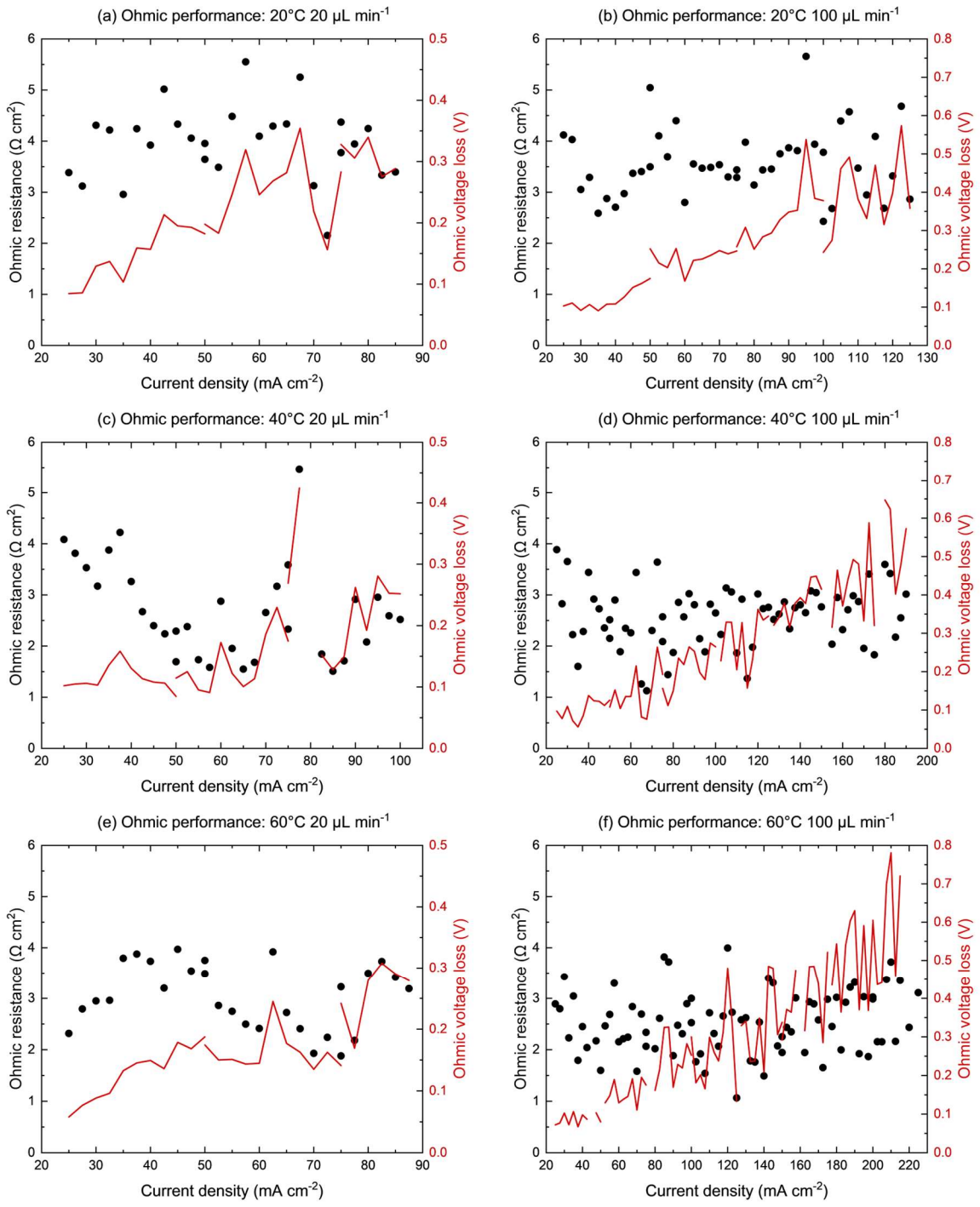

Fig. D-2: Measured ohmic resistance acquired from imposing a Z-fit onto experimentally acquired staircase galvanostatic EIS data and the corresponding ohmic voltage losses for (a) 20 °C, 20 µL min^{-1}, (b) 20 °C, 100 µL min^{-1}, (c) 40 °C, 20 µL min^{-1}, (d) 40 °C, 100 µL min^{-1}, (e) 60 °C, 20 µL min^{-1}, and (f) 60 °C, 100 µL min^{-1}.

Appendix E: Water attenuation coefficient for Section 6.2.5

Using the experimental setup detailed in *Section 6.2.2*, an experiment at a monochromatic wavenumber of 4 cm^{-1} was performed to determine the water attenuation coefficient by using a calibration chip with three different spacer thicknesses (50 µm, 100 µm, and 200 µm). A linear fit for absorbance measurements at different spacer thicknesses was used to determine a water attenuation coefficient of $5.9 \cdot 10^{-3}$ μm^{-1}, which was determined as the slope of the linear fit shown below in *Fig. E-1*.

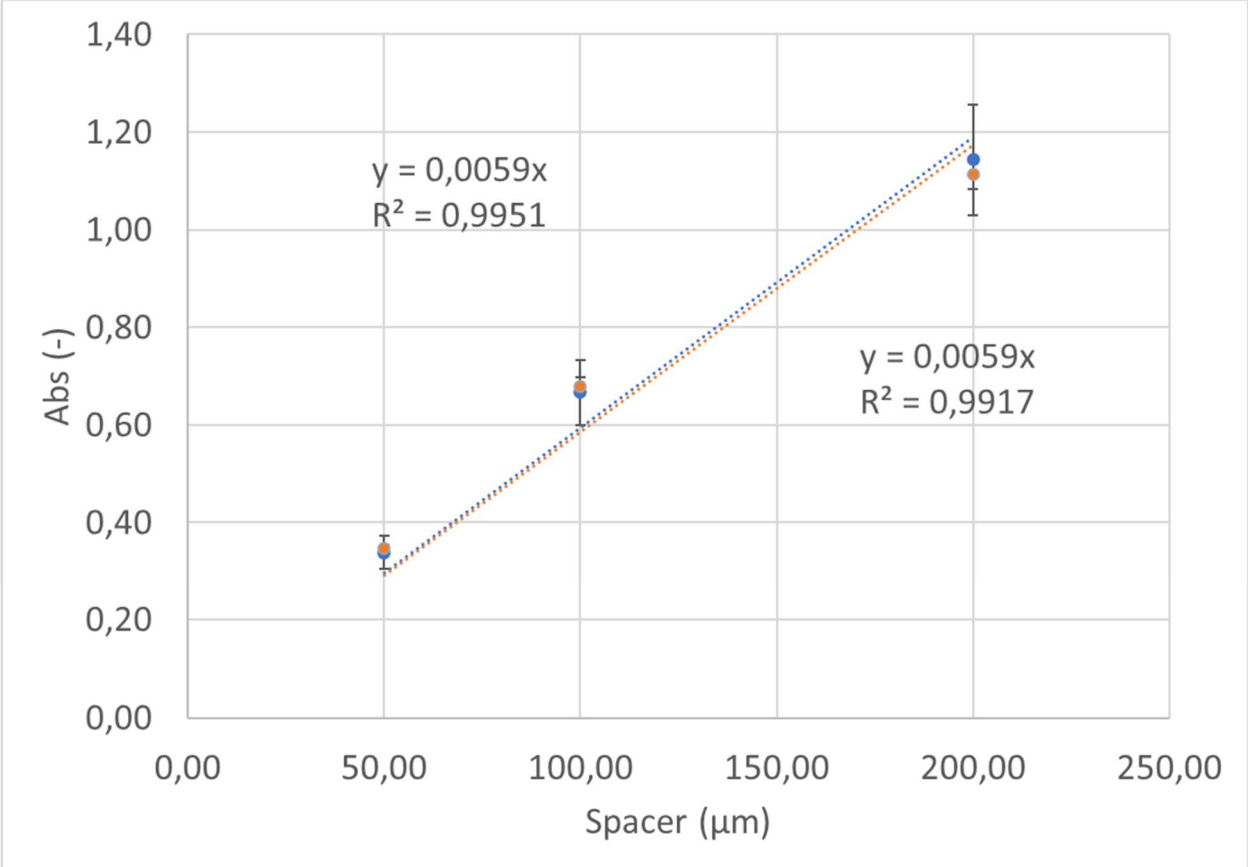

Fig. E-1: Determining the water attenuation coefficient through a calibration experiment. The water attenuation coefficient is equal to the slope of the linear fit.

Appendix F: Image binarization by digital level thresholding

Images were processed through a simple binarization based on a digital level (DL) threshold. Specifically, wet pixels all have a DL value less than dry pixels, separated by a $DL_{threshold}$, and dry pixels all have a DL value greater wet pixels, with $DL_{threshold}$ in between. $DL_{threshold}$ was determined to be a value between wet and dry pixels, such that it could be used reliably. This threshold value was determined to be $DL_{threshold} = 3000$, as this DL value is greater than that of wet pixels (for both catholyte and anolyte) and lower than that of all dry pixels, which can be confirmed in the histogram shown in *Fig. F-1*. The scale bar for the histogram ranges from 0 to 1 as data was rescaled to that range for the histogram. For the images shown (cycle 1 and image 7 for each anolyte concentration), these values linearly correspond to DL ranges of 41 to 9045, 46 to 8954, and 13 to 9643 for anolyte concentrations of 0.1 mol L^{-1}, 0.5 mol L^{-1}, and 1.0 mol L^{-1} H_2SO_4, respectively. With these DL ranges, a DL value of 3000 would correspond to 0.33, 0.34, and 0.31 when fitted between 0 to 1 for anolyte concentrations of 0.1 mol L^{-1}, 0.5 mol L^{-1}, and 1.0 mol L^{-1} H_2SO_4, respectively.

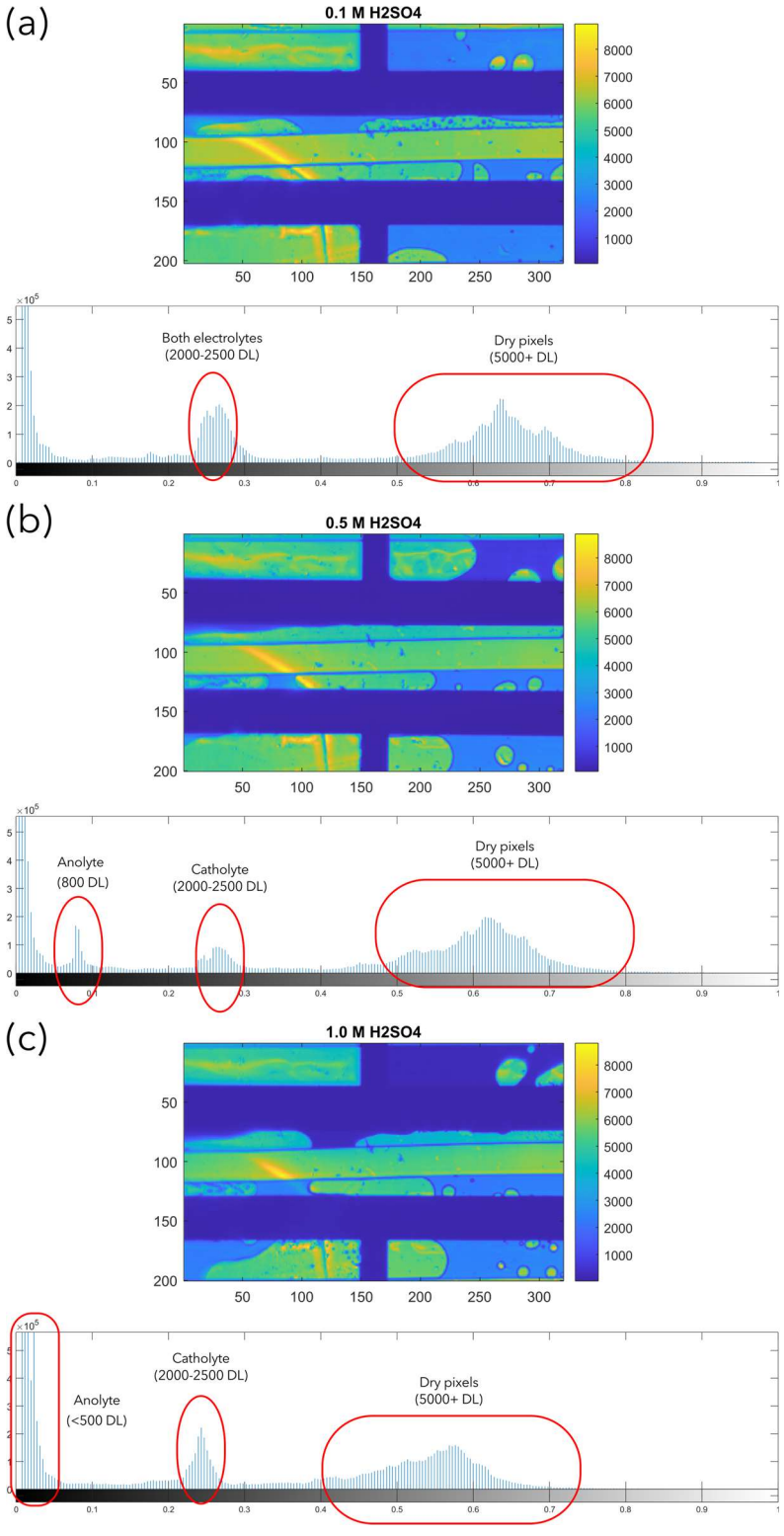

Fig. F-1: Histograms to show the DL threshold for image binarization for sample images containing anolyte concentrations of (a) 0.1 M H_2SO_4, (b) 0.5 M H_2SO_4, and (c) 1.0 M H_2SO_4.

Appendix G: Analysis of PEM hydration for three characteristic regions

In this section, the figure for which the adjacent channels of the wet, hybrid, and dry region are shown below in *Fig. G-1*. Additionally, the linear fitting parameters from *Eq. 6-15* are shown in *Tab. G-1*, *Tab. G-2*, and *Tab. G-3*.

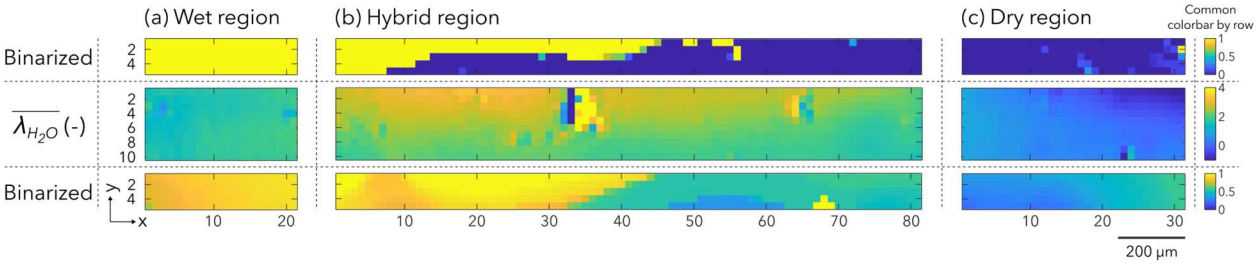

Fig. G-1: The adjacent channels in the sample image with 1.0 mol L^{-1} anolyte, cycle 1 image 7 for the (a) wet region, (b) hybrid region, and (c) dry region. Images in rows that are labeled "Binarized" are processed through a threshold algorithm to separate pixels into wet (=1) and dry (=0).

Tab. G-1: The linear fit coefficients from Eq. 6-15 *for each column from the wet region of interest (*Fig. 6-10*), resulting values from the fitted* $\overline{\boldsymbol{\lambda_{fit}}}$ *at y positions of 1 and 10, the associated* $\boldsymbol{\Delta\overline{\lambda_{fit}}}$*, and the same values from experimental measurements.*

Column of interest	$\boldsymbol{a_1}$	$\boldsymbol{a_0}$	Fitted at y = 1	Fitted at y = 10	$\boldsymbol{\Delta\overline{\lambda_{fit}}}$	Measurement at y = 1	Measurement at y = 10	$\boldsymbol{\Delta\overline{\lambda_{meas}}}$
	0.023	1.34	1.39	1.57	-0.18	1.56	1.68	-0.12
	0.012	1.47	1.50	1.59	-0.095	1.60	1.59	0.0093
	0.029	1.54	1.60	1.83	-0.23	1.71	1.84	-0.13
	0.027	1.62	1.67	1.89	-0.22	1.69	1.86	-0.17
	0.011	1.79	1.81	1.90	-0.089	1.84	1.85	-0.013

Tab. G-2: The linear fit coefficients from Eq. 6-15 *for each column from the hybrid region of interest (*Fig. 6-11*), resulting values from the fitted* $\overline{\boldsymbol{\lambda_{fit}}}$ *at y positions of 1 and 10, the associated* $\boldsymbol{\Delta\overline{\lambda_{fit}}}$*, and the same values from experimental measurements.*

Column of interest	$\boldsymbol{a_1}$	$\boldsymbol{a_0}$	Fitted at y = 1	Fitted at y = 10	$\boldsymbol{\Delta\overline{\lambda_{fit}}}$	Measurement at y = 1	Measurement at y = 10	$\boldsymbol{\Delta\overline{\lambda_{meas}}}$
	-0.13	3.28	3.15	2.01	1.14	3.07	2.06	1.01
	-0.10	2.99	2.89	2.01	0.88	2.88	2.18	0.70
	-0.10	2.95	2.85	1.95	0.90	2.72	1.92	0.80
	-0.09	2.71	2.62	1.79	0.83	2.61	1.87	0.74
	-0.078	2.36	2.28	1.58	0.70	2.36	1.68	0.68

Tab. G-3: The linear fit coefficients from Eq. 6-15 *for each column from the dry region of interest (*Fig. 6-12*), resulting values from the fitted* $\overline{\boldsymbol{\lambda_{fit}}}$ *at y positions of 1 and 10, the associated* $\boldsymbol{\Delta\overline{\lambda_{fit}}}$*, and the same values from experimental measurements.*

Column of interest	$\boldsymbol{a_1}$	$\boldsymbol{a_0}$	Fitted at y = 1	Fitted at y = 10	$\boldsymbol{\Delta\overline{\lambda_{fit}}}$	Measurement at y = 1	Measurement at y = 10	$\boldsymbol{\Delta\overline{\lambda_{meas}}}$
	0.012	0.73	0.75	0.85	-0.10	0.68	0.78	-0.10
	0.025	0.39	0.41	0.64	-0.23	0.33	0.56	-0.23
	0.057	-0.018	0.039	0.55	-0.51	-0.065	0.49	-0.57
	0.11	-0.54	-0.43	0.59	-1.02	-0.53	0.47	-1.00
	0.12	-0.81	-0.69	0.35	-1.04	-0.90	0.24	-1.14